

MOLECULARLY ENGINEERED SURFACES FOR  
EARLY CANCER DIAGNOSIS

by

MOHAMMAD RAZIUL HASAN

Presented to the Faculty of the Graduate School of

The University of Texas at Arlington

in Partial Fulfillment of the Requirements for the Degree of

DOCTOR OF PHILOSOPHY

THE UNIVERSITY OF TEXAS AT ARLINGTON

December 2017

Copyright © by Mohammad Raziul Hasan 2017

All Rights Reserved

## Acknowledgements

I am grateful to my parents for their continuous support, patience, and understanding in every part of my life. I would like to express my sincere gratitude to my advisor Dr. Samir M. Iqbal for his guidance, support, and encouragement in my research work. My heartiest gratitude goes to Dr. Vinay Abhyankar, Dr. Young-tae Kim, and Dr. Ashfaq Adnan for their technical guidance at different stages of my research projects. I also thank Dr. Kambiz Alavi, Dr. Ali Davoudi for their kind consent to review my dissertation and for being on my Ph.D. committee. I will take this opportunity to thank my co-workers Yuan Wan, Waseem Asghar, Arif Iftakher, Azhar Ilyas, Motasim Bellah, Waqas Ali, Muhymin Islam, Mohammad Abdallah, Usman Raza, Saisantosh Sasank Peri, Wenny Pham, Madiha Hanif, Adeel Sajid, Rajaraheel Khanzada, Ryan Khan, Loan Bui, Viraj Sabane, and many others for their advice, stimulating discussion, and hands-on help during my research. A special thanks goes to the staff of the Department of Electrical Engineering, Nanotechnology Research Center, Characterization Center for Materials and Biology (C<sup>2</sup>MB), Texas Advanced Computing Center (TACC), UTA Genomic Core Facility (GCF), and UTA Research Institute (UTARI). My deepest gratitude to my wife Nuzhat Mansur for her support. Thanks to ALLAH for my life and everything.

December, 2017

## Abstract

### MOLECULARLY ENGINEERED SURFACES FOR EARLY CANCER DIAGNOSIS

Mohammad Raziul Hasan, PhD

The University of Texas at Arlington, 2017

Supervising Professor: Samir M. Iqbal

Early detection of cancer can have immediate and significant impact on effective treatments for cancer patients and better disease prognosis. In the early stage of cancer, symptoms are initially expressed at molecular and cellular scales. Identification and capture of cancer cells can greatly advance cancer research. This research work is aimed to introduce novel biosensors and technologies for early cancer detection. We developed a one-step method to create nanotextured polymer substrates and showed the effect of surface nanotexture on cancer cell adhesion and cell surface interactions. The nanotextured surface was functionalized with an antibody to selectively capture cancer cells from a cell mixture. Nanotextured PDMS showed higher cell adhesion strength and enhanced cell capture. We also demonstrated a reversible sealed modular device approach to integrate nanotextured substrates into microfluidics for cell capture applications. The modular approach simplified cell capture workflow, provided easy assembly, and enabled a user-friendly method to access cells for post-capture analysis. We also observed that cancer cells showed distinct morphology on biofunctionalized surfaces. We developed a technique to quantify cell gestures using dynamic morphology from time-lapse optical micrographs of cells on functionalized surface. We used a supervised machine learning method to develop an automated system to identify cancer cells from their gestures. The system offered rapid, efficient, and novel identification of brain cancer cells and can be extended to classify many other types of tumor cells. Both of these detection mechanisms were based on the expression of protein biomarkers on

the cell surface. A nanopore sensor is a unique platform for detecting protein biomarkers from ionic current signatures. The underlying mechanism of protein translocation through the nanopore is very difficult to understand from outside. We constructed a molecular dynamics model to simulate protein translocation through a nanopore to reveal the interatomic interactions and investigate the deformation mechanisms of thrombin inside a nanopore due to externally applied electric fields. We investigated the structural integrity of protein and its deformation dynamics inside a nanopore. The development of this technique has advanced nanopore research by providing insights about molecular level information to complement macroscopic measurements in the laboratory.

## Table of Contents

Acknowledgements .....	iii
Abstract.....	iv
Table of Contents.....	vi
List of Illustrations .....	xi
List of Tables.....	xx
1. Introduction .....	1
1.1. Structure of Dissertation .....	1
1.1.1. <i>Introduction (Chapter 1)</i> .....	1
1.1.2. <i>Background and Review (Chapter 2)</i> .....	2
1.1.3. <i>One-Step Fabrication of Flexible Nanotextured PDMS as a Substrate for Selective Cell Capture (Chapter 3)</i> .....	2
1.1.4. <i>Classification of Cancer Cells using Computational Analysis of Dynamic Morphology (Chapter 4)</i> .....	2
1.1.5. <i>Molecular Dynamics Study of Protein Deformation in Solid-State Nanopores (Chapter 5)</i> .....	3
1.1.6. <i>Future Works (Chapter 6)</i> .....	3
2. Background and Review.....	4
2.1. Cancer Statistics.....	4
2.2. Origin of Cancer and Carcinogenesis .....	5
2.3. Cancer Metastasis and Early Detection .....	6
2.4. Cancer Biomarkers and EGFR .....	9
2.5. Biomarker Detection Molecules .....	10
2.5.1. <i>Antibody</i> .....	10
2.5.2. <i>Aptamer</i> .....	11
2.6. Cancer Detection Devices .....	13
2.6.1. <i>Mechanical Sorting</i> .....	13
2.6.2. <i>Affinity-based Detection Devices</i> .....	19

2.7.	Nanotextured Substrates for Cancer Detection.....	25
2.8.	Soft Lithography for Microfluidic Device Fabrication .....	28
2.9.	Imaging-based Cancer Diagnosis .....	29
2.10.	Machine Learning for Cancer Detection .....	32
2.11.	Nanopore and Molecular Dynamic Simulation for Label-free Detection of Protein.....	32
2.11.1.	<i>Fabrication of Nanopore .....</i>	33
2.11.2.	<i>Working Principle of Nanopore .....</i>	34
2.11.3.	<i>Molecular Dynamics Simulation of Nanopore.....</i>	35
2.11.4.	<i>Molecular Dynamics Simulation Software .....</i>	37
3.	One-Step Fabrication of Flexible Nanotextured PDMS as a Substrate for Selective Cell Capture.....	38
3.1.	Introduction.....	38
3.2.	Experimental .....	40
3.2.1.	<i>PDMS Channel Fabrication .....</i>	40
3.2.2.	<i>Replica Molding of Nanotextured and Plain PDMS surfaces .....</i>	41
3.2.3.	<i>Surface Texture Quantification and Imaging .....</i>	41
3.2.4.	<i>Surface Area Calculations .....</i>	42
3.2.5.	<i>Contact Angle Measurements.....</i>	42
3.2.6.	<i>Nanotextured PDMS Silanization.....</i>	42
3.2.7.	<i>Neutravidin Conjugation and Antibody Attachment ....</i>	43
3.2.8.	<i>Reversibly Sealed Easy Access Modular (SEAM) Platform Integration.....</i>	43
3.2.9.	<i>Cell Culture.....</i>	44
3.2.10.	<i>Cell Capture Experiments.....</i>	44
3.2.11.	<i>Threshold Fluid Shear Stress.....</i>	45
3.2.12.	<i>Four-parameter Curve Fitting.....</i>	46

3.2.13.	<i>Cell Adhesion Improvement and Cell Capture Enhancement Calculation</i>	47
3.2.14.	<i>Nucleic Acid Extraction</i>	47
3.2.15.	<i>Statistical Analysis</i>	48
3.3.	Results and Discussion	48
3.3.1.	<i>Nanotextured PDMS</i>	48
3.3.2.	<i>Effect of Nanotexture on Surface Area</i>	50
3.3.3.	<i>Nanotexture and Surface Composition</i>	51
3.3.4.	<i>Integration of Nanotextured PDMS into microfluidic architecture</i>	52
3.3.5.	<i>Nanotexture for Enhanced Cell Adhesion</i>	53
3.3.6.	<i>Nanotexture for Enhanced Cell Capture</i>	55
3.3.7.	<i>Selective Capture of Cancer Cells on Nanotextured Surfaces from a Multi-Cell Mixture</i>	57
3.3.8.	<i>Simplified Workflow for Nucleic Acid Isolation from Captured Cells</i>	59
3.4.	Discussion	62
3.5.	Conclusion	63
4.	Classification of Cancer Cells using Computational Analysis of Dynamic Morphology	64
4.1.	Introduction	64
4.2.	Materials, Methods, and Experimental Setup	66
4.2.1.	<i>System Overview</i>	66
4.2.2.	<i>Surface Functionalization</i>	67
4.2.3.	<i>Cancer and Healthy Cell Preparation</i>	69
4.2.4.	<i>Effect of Aptamer on Morphology of Cancer Cells</i>	70
4.2.5.	<i>Image Acquisition and Processing</i>	70
4.2.6.	<i>Feature Extraction and Annotation of Cell Gesture</i>	71
4.2.7.	<i>Feature Extraction</i>	73



4.2.8.	<i>Definition of Features</i> .....	74
4.2.9.	<i>Data Classification</i> .....	76
4.2.10.	<i>Machine Learning Algorithm</i> .....	77
4.3.	Results and Discussion .....	78
4.3.1.	<i>Classification of Cell Gesture Using Supervised Methods</i> .....	78
4.3.2.	<i>Feature Ranking</i> .....	79
4.3.3.	<i>Confusion Matrix Analysis</i> .....	80
4.3.4.	<i>Comparison between Classifiers</i> .....	81
4.3.5.	<i>Precision-Recall Curve Analysis</i> .....	82
4.4.	Conclusion.....	87
5.	Molecular Dynamics Study of Protein Deformation through Solid-State Nanopore .....	88
5.1.	Introduction.....	88
5.2.	Materials and Methods .....	91
5.2.1.	<i>Simulation Details</i> .....	91
5.2.2.	<i>Model Construction</i> .....	92
5.2.3.	<i>Nanopore Construction and Energy Minimization</i> .....	93
5.2.4.	<i>Force-field Calculations</i> .....	95
5.3.	Results and Discussion .....	96
5.4.	Conclusion.....	103
6.	Future research directions.....	104
6.1.	Introduction.....	104
6.2.	Effect of Nanotexture and Stiffness of Substrate in Cell Adhesion .....	104
6.3.	Diagnosis of Different Cell Types using Dynamic Morphology Analysis.....	104
6.4.	Cell Gesture at Different Stages of Cancer .....	105

6.5. MD Simulation for EGFR and EGFR-aptamer Complex Translocation through Nanopore .....	105
7. Conclusion .....	106
References.....	107
Biographical Information.....	123
Appendix .....	124
Permission from co-authors and publishers.....	124

## List of Illustrations

- Figure 2.1. Change in mortality rate in the USA per 100,000 population in the year 1950 and 2015 [3, 4]. ..... 4
- Figure 2.2. Two-hit tumor formation in both hereditary and non-hereditary retinoblastoma. (a) All retinoblasts are one-hit clones in hereditary retinoblastoma. (b) A 'one-hit' clone acts as a precursor to the tumor in non-hereditary retinoblastomas. Reprinted with permission [11]. ..... 6
- Figure 2.3. The process of cancer metastasis. (a) Metastatic cancer cells break free from the primary tumor and migrate to the vasculature. (b) Then the cancer cells keep flowing in the bloodstream until they find a metastasis-supporting site to colonize. (c) Platelets attack cancer cells in the bloodstream and protect them from the immune system. (d) Upon interaction with the secondary organ, cancer cells adapt to the local environment and proliferate in the secondary site. Reprinted with permission [15]. ..... 7
- Figure 2.4. Five-year survival rate of cancer patients diagnosed at different stages of cancer. The survival rate decreases significantly as the disease progress to advanced stages [16]. ..... 8
- Figure 2.5. Breast Cancer treatment cost after one and two years of diagnosis. The treatment cost is higher for advanced stages of cancer. The cost of treatment also gets higher when it is diagnosed late [17]. ..... 8
- Figure 2.6. Schematic representation of the production of monoclonal antibodies through hybridization method. (a) Immunization of mice with antigen stimulates immune cells which produce antibodies that recognize the antigen. (b) Immune cells are isolated. (c) Antibody-producing cells are fused with tumor cells to generate immortalized hybridoma cells. (d) Antibody-secreting hybridoma cells are screened and amplified by clonal expansion. (e) Extraction of monoclonal antibodies. Reprinted with permission [24]. ..... 11
- Figure 2.7. Schematic representation of DNA aptamer selection using SELEX. DNA sequences having specific recognition to target cells are evolved to enrich

the selection pools. The enriched pools are cloned and the positive clones are sequenced to identify individual aptamers. Reprinted with permission [30]. .... 12

Figure 2.8. Schematic representation of size-based cancer cell isolation methods. (a) Microporous membrane isolating larger tumor cells (purple) from red blood cells (red). (b) A microfluidic device to sort cancer cells using gradual filtration method. A schematic of the gradual filtration process is shown at the bottom left. Series of micropost structures fabricated in PDMS to block large cancer cells from passing through (right). ..... 14

Figure 2.9. (a) Working principle of a micropore sensor to isolate cancer cells from blood cells by ionic current signature. (i) Base ionic current measurement (red signal) for open pore. (ii) An ionic current drop is registered when the pore is blocked by the cell. (iii) A complete cell translocation is recorded as an electrical current fingerprint. (b) Schematic representation of hydrodynamic stretching of single cell to measure cell deformability. A narrow stream of sample cells is formed in a microfluidic channel using sheath flow. The sheath fluids hydrodynamically focus the cell in the middle of the channel. The cell gets deformed by the shear from two sides known as 'hydrodynamic pinching'. A high-speed camera takes snapshot of the deformed cell and then the deformability is calculated by image analysis. Cells having different size and deformability appears as different clusters in the scatter plot [37, 38]..... 16

Figure 2.10. Schematic representation of cell density-based isolation methods. (a) Centrifugation method to separate heavy cells from lighter ones. Heavy cells form a palette at the bottom of the tube because of the large centrifugal force generated in the centrifuge. (b) Spiral microfluidics for cell sorting. Reprinted with permission [44]. A mixture of cells is flown in a spiral microfluidic channel from the center to the outward direction. The inset shows the cross-section of the channel with flow patch. Cancer cells and blood cells are collected from outlet-1 and outlet-2, respectively. (c) Label-free enumeration of cancer cells in an inertia microfluidic device. Reprinted with permission [45]. Cell samples are pre-filtered in the channel (inset-1). The velocity profile of the flow pushes the cells toward the side of the channel (inset-2). The heavier tumor cells (purple) gets trapped in

the vortex region and smaller blood cells continue to flow through the channel (inset-3). ..... 18

Figure 2.11. Schematic illustration of FACS. Fluorescent antibodies are selectively attached to sample cell mixture. Individual cells are scanned by a laser. Multiple sensors capture scattered and fluorescent light. A computing system analyzes the color spectra and deflects the cells into separate collection tubes using a charged deflection plate. .... 20

Figure 2.12. Schematic illustration of magnetically activated cell sorting (MACS). Magnetic particles (yellow) selectively attach to cancer cells via antibody (green). An external magnetic field attracts the magnetic particle coated cells towards the cell container wall while the rest of the cells are flushing out. The inset shows a schematic of the magnetic particle attachment via antibodies. .... 21

Figure 2.13. A microfluidic chip combining hydrodynamic cell sorting, inertial focusing and magnetically operated sorting. Hydrodynamic sorting section isolates larger cells (WBCs and magnetic particle coated CTCs) from RBCs, platelets and other blood components. Then the external magnetic field deflects magnetic particle coated CTCs from WBCs. Reprinted with permission [52]. ... 22

Figure 2.14. Schematic representation of cancer cell capture on an antibody-functionalized surface. (a) Antibody immobilization on the surface. (b) Cells interacting with the functionalized surface. (c) Cancer cells captured on the surface immobilized antibodies. .... 22

Figure 2.15. Affinity-based microfluidic devices to isolate circulating tumor cells. (a) Schematic of a CTC-microchip device micropost arrays [53]. The device is sealed with the manifold with adhesive tapes. (b) Cancer cell captured on anti-EpCAM functionalized silicon micropost in the CTC-chip device; inset shows a magnified view of the captured cell (red). (c) Herringbone-chip containing fishbone patterned structure inside channel ceiling [54]. The channel is functionalized with antibodies. The herringbone grooves generate chaotic microvortices inside the channel to increase interaction with cells. (d) Flow visualization inside HB-chip. (e) Microfluidic Cluster-Chip for cancer cell detection [56]. SEM micrographs show multiple rows of shifted triangular pillars creating

consecutive cluster traps for CTCs; scale bar = 60  $\mu\text{m}$ . (f) High-magnification image of Cluster-Chip with a CTC cluster captured in the device; scale bar = 60  $\mu\text{m}$ . Reprinted with permission. .... 24

Figure 2.16. Effect of nanotexture in nature. (a) Water droplet floating on a hydrophobic surface of lotus leave due to its surface texture. (b) The nanotexture on transparent dragonfly wing controls transmission of light. (c) The nanotexture on moth eye is responsible for photon absorption. (d) A rose petal and the convex topography on the surface. The inset shows the SEM micrograph of surface texture [60-63]. Reprinted with permission. .... 26

Figure 2.17. Methods of fabricating nanotextured surfaces. (a) Schematic of bottom-up approach where materials are deposited on a substrate to make a nanotextured surface. Examples include: (b) Deposited ZnO nanoparticle to study osteoblast cancer cells [71], (c)  $\text{TiO}_2$  nanofiber deposited on a silicon substrate with electrospinning method to create CTC capture assay [65], and (d) Chemically deposited graphene-oxide for CTC isolation [66]. (e) Schematic representation of top-down approach that involves removal of the substrate with wet and dry etching methods. Examples include: (f) Reactive ion etched quartz silicon nanowire structure [67], (g) Silicon nanopillars array [69], and (h) Sandblasted glass with nanotexture on the surface [70]. Reprinted with permission. .... 27

Figure 2.18. Replica molding process. (a) A solid surface with the inverted pattern called 'master'. (b) PDMS mixture (PDMS and curing agent) is poured on master and then thermally cured. (c) The thermally-cured solid PDMS is peeled off from the master. (d) PDMS is oxygen-plasma bonded with a flat glass surface for microfluidic devices. .... 29

Figure 2.19. Illustration of different forces involved in cell migration. There are three major steps: protrusion, translocation and detachment. The protrusion of lamellipodia or filopodia starts by the force generated by actin polymerization. Translocation may occur by myosin interactions with actin filaments at the rear end. Finally, cell detaches from the rear which is accelerated by myosin-mediated

actin filament contraction pulling on adhesion complexes. Reprinted with permission. .... 31

Figure 2.20. Schematic flow of nanopore fabrication. (a) A cross-section of a silicon chip. (b) Silicon nitride deposition on both sides on the silicon chip. (c) Photoresist coating on one the backside silicon nitride. (d) An etch window is patterned in the photoresist layer using photolithography. (e) The patterned window is transferred to silicon nitride hard mask using dry etch. (f) Silicon is anisotropically etched with wet etchant (tetramethylammonium hydroxide, TMAH) through the etch window. The crystallographic orientation of silicon creates a slanted sidewall. (g) TEM drilling of the silicon nitride membrane. (h) and TEM micrograph of a 20 nm diameter nanopore. .... 34

Figure 2.21. Protein translocation through nanopore [94]. Bovine serum albumin, BSA was passed through the nanopore in an ionic buffer with pH 5 (labeled A) and pH 3 (labeled B) at 50 mV. (C) Time-resolved current signal of BSA (black and green) and avidin (red and blue) at pH 3 (black and red) and pH 6 (green and blue), respectively. Reprinted with permission..... 35

Figure 2.22. Flowchart of a molecular dynamic simulation calculation..... 36

Figure 3.1. Workflow of replica molding (a-c). (a) The backside of a silicon wafer is used as the master for the nanotextured PDMS. A PMMA cavity is used to control the thickness of the PDMS block. (b) PDMS is poured into the PMMA cavity and a transparent mylar sheet is used at the top to maintain a flat surface on the other side. (c) Cured nanotextured PDMS block is released from the master..... 41

Figure 3.2. Surface topography of plain and nanotextured PDMS captured at 30° angle in low vacuum. (a) SEM micrograph of plain PDMS. The inset shows the surface topography measured with AFM. (b) SEM micrographs of nanotextured PDMS. A high magnification image of the surface topography is shown in the inset. .... 49

Figure 3.3. Surface roughness profiles of plain and nanotextured PDMS measured by the profilometer. The scale in the vertical axis of the two profiles

represents the difference in surface roughness. The root mean square (RMS) roughness ( $R_q$ ) of nanotextured and plain PDMS was  $682 \pm 102$  nm and  $3.7 \pm 1.5$  nm, respectively ( $p$ -value  $< 0.05$ ,  $n = 8$ ). ..... 50

Figure 3.4. Change in water contact angle on plain and nanotextured PDMS surfaces due to silanization process. The contact angles ( $\theta_c > 90^\circ$ ) of untreated plain and nanotextured PDMS suggest a hydrophobic material. Both of the surfaces changed to hydrophilic ( $\theta_c < 90^\circ$ ) after thiol functionalization. Because of the increased surface area on the nanotextured surface, the thiol functionalization made nanotextured PDMS more hydrophilic ( $\theta_{nanotextured} = 49.7^\circ \pm 3.6$ ) compared to plain PDMS ( $\theta_{plain} = 61.3^\circ \pm 6.8$ ) as is shown by the contact angle measurements. .... 51

Figure 3.5 (a) Schematic showing the microfluidic integration of nanotextured PDMS using the SEAM platform that consists of PMMA housings with embedded magnets, nanotextured PDMS surface, and PDMS channel. Magnets are installed in top and bottom housings with opposite polarity facing each other for self-aligned assembly. (b) Image of an assembled device. Channel access ports are connected to syringe pump through microfluidic tubing and barb fittings. Red dye was loaded into the channel for visualization. (Scale bar = 10 mm). ..... 53

Figure 3.6. a) Cell attachment as a function of wall shear stress. The dashed line represents the 50% cell detachment threshold. The experimental data were fitted with a 4-parameter sigmoidal fit (coefficient of determination,  $R^2 > 0.99$  for both data series). The reduced chi-square values for the fitted curves were 2.3 and 2.0 for plain and nanotextured PDMS, respectively. b) The average shear stress required to detach 50% cells captured on functionalized plain PDMS ( $24 \pm 0.4$  dyne/cm<sup>2</sup>) and nanotextured ( $30 \pm 0.7$  dyne/cm<sup>2</sup>) PDMS; ( $*p$ -value  $< 0.05$ ,  $n = 4$ ). ..... 54

Figure 3.7. Fluorescence intensity of biotin-atto-488 conjugated on neutravidin and control functionalized PDMS surfaces. All the values are normalized with respect to average fluorescence intensity on plain PDMS. The average fluorescence intensity on neutravidin functionalized plain and nanotextured PDMS surfaces were  $4.67 \pm 0.32$  and  $5.7 \pm 0.24$ , respectively; Fluorescence



intensity on plain and nanotextured control PDMS surfaces were  $1 \pm 0.14$  and  $1 \pm 0.09$  (*\*p-value* < 0.05, #*p-value* = 0.96, *n* = 3). The presence of nanotexture increased the surface area and helped to accommodate a higher number of neutravidin molecules on the surface. .... 55

Figure 3.8. (a) Schematic showing cell capture process. Surfaces are incubated with A549 cells and washed using a syringe pump. (b) Representative fluorescent images of captured A549 cells on nanotextured (top) and plain PDMS (bottom); scale bar is 100  $\mu\text{m}$ . Fluorescent images of A549 superimposed on bright-field micrographs of the respective surfaces for visualization. (c) The density of captured A549 cells on anti-EGFR and isotype control functionalized plain and nanotextured PDMS. The A549 cell densities (average number of cells/ $\text{mm}^2$ ) on anti-EGFR antibody functionalized plain and nanotextured surfaces were  $85 \pm 14$  and  $148 \pm 37$  cells/ $\text{mm}^2$ , respectively; cell densities on isotype control plain and nanotextured PDMS surfaces were  $4 \pm 2$  and  $7 \pm 3$  cells/ $\text{mm}^2$ ; (*\*p-value* < 0.05, #*p-value* = 0.15)..... 56

Figure 3.9. (a) Schematic of specificity experiments. Nanotextured surfaces are incubated with a mixture of A549:HUVEC at 1:1 ratio and washed using a syringe pump. (b) Representative fluorescent images of the cell mixture before (left) and after wash (right); green cells are A549 cells and red are HUVECs; scale bar = 100  $\mu\text{m}$  for both images. (c) Graphical representation of average cell densities of A549 cells and HUVECs on anti-EGFR and the control surfaces after the washing step. Average A549 and HUVEC cell densities on anti-EGFR modified surfaces were  $52 \pm 4.1$  and  $4.0 \pm 0.7$  cells/ $\text{mm}^2$ , respectively. The average number of cells captured on isotype modified surfaces were  $1 \pm 0.2$  cells/ $\text{mm}^2$ . (*\*p-value* = 0.0001, *\*\*p-value* = 0.005, *\*\*\*p-value* = 0.0001; *n* = 3)..... 58

Figure 3.10. (a) Nucleic acid extraction from captured cells using in-channel lysis. The dotted line represents flow path for the lysis buffer and sample collection. (b) Cell lysis with direct transfer of captured cells from nanotextured PDMS surface into lysis buffer. (c) Comparison of nucleic acid extraction efficiency using the two methods. The data is normalized to the amount of nucleic acid directly extracted from a cell suspension. (*\*p-value* < 0.05; *n* = 5). .... 61

Figure 4.1. Schematic of dynamic morphological analysis of cell gesture. Optical micrographs of the cell population are processed with image analysis tool to detect the cell-contour. A collection of feature vectors is extracted to generate a morphological profile. The data for cell gesture is stored in a dataset. Machine learning algorithm is used to generate decision-making system to classify the cells based on the training data. Once the classification model is developed, unknown cells are classified based on the resemblance of their feature vectors to the known dataset. .... 67

Figure 4.2. Schematic representing anti-EGFR aptamer functionalization on glass substrate. .... 68

Figure 4.3. Effect of aptamer on the morphology of cancer cells. (a) EGFR expressed tumor cells interacts with anti-EGFR aptamer functionalized glass surface. (b) Tumor cells show distinct morphology over time when seeded on anti-EGFR aptamer functionalized surface. (c) Tumor cells do not show much activity in absence of aptamer on the surface. .... 70

Figure 4.4. Representative time-lapse images of a cancer cell and a healthy cell on anti-EGFR functionalized surface taken with an optical microscope. The changes in cell morphology over time are more pronounced for cancer cell.... 71

Figure 4.5. Features extracted from grayscale optical micrographs of a cell. (a) Grayscale image of the cell. The scale bar = 10  $\mu\text{m}$ . (b) The contour of the cell. (c) 4-point shape estimation. (d) Convexity from cell contour. (e) Bounding rectangle. (f) Minimum enclosing circle. (g) Best fitted ellipse. (h) Extreme points. .... 72

Figure 4.6. Feature ranking of the top 25 features in descending order of importance. The vertical lines represent the standard deviations of importance-metric. .... 80

Figure 4.7. Confusion matrix of the SVM classifier for active cancer, inactive cancer, and healthy cell categories. The intensity bar represents the scale. ... 81

Figure 4.8. (a) Precision-Recall plot for the predictive model trained with SVM classifier. The black solid line represents the average performance of the model.

(b) Performance comparison of three different classifiers. The average value of precision and recall are plotted here for each classifier model. The area under the curve (AUC) for each model is mentioned in the legend..... 83

Figure 5.1. (a) Schematic representation of nanopore experiment to capture the ionic current signature for protein translocation. The inset shows an actual TEM drilled pore. (b) Model of the simulated system: all-atom MD model comprised of a thrombin inside a Si<sub>3</sub>N<sub>4</sub> nanopore. The pore is solvated with KCl. The inner diameter of the pore is 6 nm, simulated periodic cell structure was 68 Å × 78 Å × 96 Å. .... 91

Figure 5.2. (A) Construction of Si<sub>3</sub>N<sub>4</sub> nanopore from a Si<sub>3</sub>N<sub>4</sub> unit cell using NAMD. (1) Si<sub>3</sub>N<sub>4</sub> unit cell; (2) Single-molecule thick Si<sub>3</sub>N<sub>4</sub> membrane; (3) the membrane is given a convenient geometry; (4) a nanopore in a Si<sub>3</sub>N<sub>4</sub> membrane. (B) Visualization of the thrombin molecule inside a Si<sub>3</sub>N<sub>4</sub> membrane (using VMD). Each color represents a different secondary structure. (C) The complete model of the system with molecular transport through nanopore under an applied bias. .... 94

Figure 5.3. Energy minimization of the system with conjugate gradient method for 20 nanoseconds. The inset shows the minimization of energy during the first 40 picoseconds..... 95

Figure 5.4. Root mean squared deviation (RMSD) of the protein backbone compared with the initial conformation. .... 98

Figure 5.5. (a) Radial distribution analysis of thrombin's structure after 20 ns simulation at increasing electric fields. The vertical axis represents the number of atom-pair at a distance mentioned in the horizontal axis. (b) Normalized radial distributions function. The density of atoms lying on the surface of a sphere at the listed distance from an atom. .... 100

Figure 5.6. Current-Voltage profile of the system. The average ionic current is linearly dependent on the applied potential when the protein is inside the nanopore. The inset shows the linear relationship between the two entities. The data points are interpolated with linear regression analysis..... 102

## List of Tables

Table 2.1. List of biomarkers overexpressed in different cancer. EGFR is a common biomarker for most of the cancers. ....	10
Table 2.2 Comparison of antibody and aptamer.....	13
Table 3.1. Simulated wall shear-stress as a function of flow rate .....	46
Table 3.2. Elemental analysis of plain and nanotextured PDMS (C <sub>2</sub> H <sub>6</sub> OSi) <sub>n</sub> ...	52
Table 4.1. List of feature vectors with quantitative measure. ....	75
Table 4.2. Average accuracy of classification using SVM, RFT, and NBC computed with five-fold validation technique. The standard deviation was calculated from the accuracy among the five combinations of training sets in cross-validation.....	79
Table 4.3. Precision, recall and F1-score measurements (The maximum value of each column in shown in bold).....	82

## Chapter 1

### 1. Introduction

Cancer is the second most fatal disease in the world [1]. It is the uncontrolled growth of abnormal cells in the body. Cancer cells can penetrate adjacent tissue and travel through the bloodstream to spread to other organs in the body. This spreading mechanism of cancer makes it extremely challenging to treat. Every year, billions of dollars are spent for cancer treatment and millions of people still die of cancer. Existing treatment methods of cancer include chemotherapy, radiation therapy, and surgical procedures. But the success of these approaches is limited because, in most of the cases, cancer is detected when it has progressed to an advanced stage. The treatment of cancer is much more effective if the disease is detected at an early stage. Unfortunately, an economic point-of-care cancer detection device is still missing. A fast and sensitive method to capture and identify cancer cells would be a great step toward early detection. An effective diagnostic method should be inexpensive, user-friendly, portable, and convenient to use. The focus of this dissertation work is developing devices and technologies for early detection of cancer. Three projects were undertaken to understand the working mechanism of cancer biomarkers and cells, developing new technologies to detect cancer at an early stage, and designing new devices to isolate cancer cells for effective diagnosis.

#### **1.1. Structure of Dissertation**

This dissertation is divided into 6 chapters. The breakdown of chapters is given below:

##### **1.1.1. Introduction (Chapter 1)**

This chapter provides the motivation and a short summary of the research work done in this dissertation.

### **1.1.2. Background and Review (Chapter 2)**

Chapter 2 reviews origin of cancer and possible detection methods. It gives an overview of the research work done in this field and the challenges that prevail.

### **1.1.3. One-Step Fabrication of Flexible Nanotextured PDMS as a Substrate for Selective Cell Capture (Chapter 3)**

Detection of metastatic tumor cells is important for early diagnosis and staging of cancer. However, such cells are very few in number at the onset of disease and thus very difficult to detect from blood or biopsy samples. Different functionalized surfaces have been explored and demonstrated to capture cancer cells. Introduction of nanoscale textures on the surfaces enhance the efficiency of cancer cell detection. Conventional methods to achieve nanotexture require access to specialized nanofabrication equipment within a dedicated cleanroom environment. This chapter presents a technique to create flexible polydimethylsiloxane (PDMS) surfaces using a molding approach that can be performed in a standard laboratory environment. A one-step reversible integration of nanotextured PDMS into a microfluidic platform is also demonstrated. The chapter includes characterization of nanotextured PDMS, investigation of nanotexture on cancer cell adhesion strength, and its application to selectively capture cancer cells.

### **1.1.4. Classification of Cancer Cells using Computational Analysis of Dynamic Morphology (Chapter 4)**

It is known that cancer cells, and especially metastatic tumor cells, show very distinctive morphological behavior compared to their healthy counterparts on aptamer functionalized surfaces. The ability to quickly analyze the data and quantify the cell morphology for an instant real-time feedback can certainly contribute to early cancer diagnosis. This chapter describes a supervised machine learning approach for identification and classification of cancer cell gestures for early diagnosis. The

morphologically distinct behaviors were quantified from time-lapse optical micrographs of cancer and healthy cells on aptamer-functionalized glass surfaces. Different classifier models were trained with the sample dataset to predict cancer cells from their gestures.

#### **1.1.5. *Molecular Dynamics Study of Protein Deformation in Solid-State Nanopores (Chapter 5)***

Electrophoretic translocation through solid-state nanopores is a promising technique for identification of specific proteins and protein complexes. In a typical protein detection experiment, an external electric field is applied across the nanopore and the ionic current is measured while the molecule passes through the pore. It is very important that the protein retains its structure and functionality under applied electric field and experimental conditions. This chapter presents a theoretical assessment of protein deformation in a nanopore experiment due to applied electric field. Nanoscale molecular dynamics (NAMD) simulations were done to investigate the deformation of a protein during translocation through a silicon nitride nanopore. The experimental conditions were simulated to perform quantitative analysis of the variation of a thrombin's 3D structure due to an externally applied electric field without any mechanical forces. The conformational changes, the stretching of protein structure, and the contribution of protein deformation in ionic current were studied.

#### **1.1.6. *Future Works (Chapter 6)***

In this chapter, scopes of future works that can complement/supplement the current research are discussed.

## Chapter 2

### 2. Background and Review

#### 2.1. Cancer Statistics

Cancer is one of the leading causes of death worldwide. According to International Agency for Research on Cancer (IARC), approximately eight million people die every year because of cancer [1]. By 2022, the projected number of people to be diagnosed with some sort of cancer is eighteen million [2]. In 2015, the number of new cancer cases was approximately 16 million in the USA only. Even in this twenty-first century with all the advanced medical solutions in America, about 600,000 cancer patients could not survive death. Figure 2.1 compares the mortality rate per hundred thousand people in the USA in the year 1950 and 2017 categorized by some common diseases such as cardiovascular disease, cerebrovascular disease, influenza, pneumonia, and cancer [3, 4].

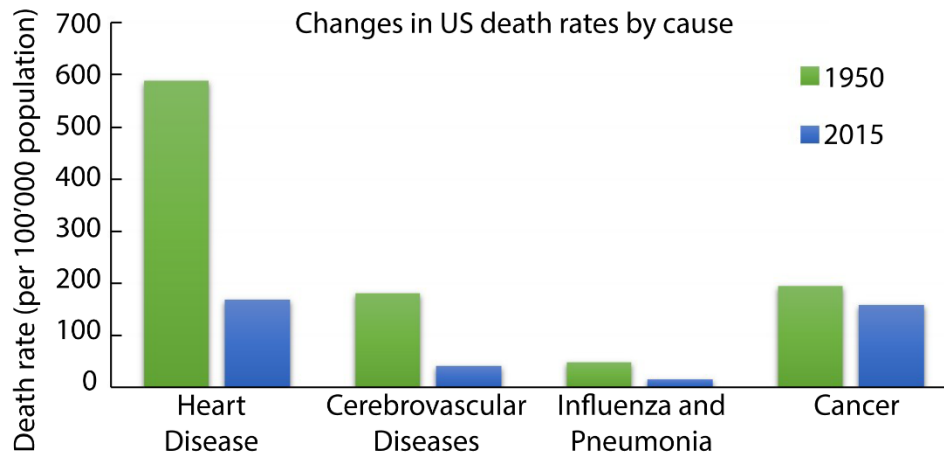


Figure 2.1. Change in mortality rate in the USA per 100,000 population in the year 1950 and 2015 [3, 4].

The harsh truth is that the mortality rate for cancer has not been improved in the past six decades compared to the significant reduction in mortality rates of other diseases. The advancement in science and technology have led to tremendous progress in the field



of medical research but unfortunately, that was not enough for cancer. But the situation is changing now. New research is emerging with innovative approaches to solve this grand challenge. Different fields of expertise are being combined together to come up with unique solutions to this problem.

## **2.2. Origin of Cancer and Carcinogenesis**

Carcinogenesis is the process through which normal cells evolve into cancerous cells. The change occurs both in genetic and phenotypic expressions of cell. The reason can be attributed to many known and unknown factors starting from personal habits, outside environment, accumulation of different defects, and mutation in DNA. In 1908, Ellerman and Bang reported an infectious virus for leukemia [5]. In later years, several other oncoviruses were discovered containing cancer-causing genomes [6-8]. These genomes can infect healthy cells by integrating the viral nucleic acids (DNA, RNA) into the host chromosome.

Normal cells go through cell division, proliferation, and cell death in a periodic manner. This periodic cell death is called apoptosis. The balance between cell growth and apoptosis is disturbed in the case of cancer. Activation of pro-oncogenes and deactivation of cancer suppressor genes cause a normal cell to transform into cancer with uncontrolled growth [9, 10]. Inheriting a germ-line copy of such damaged gene may also increase the possibility of cancer as explained by the two-hit hypothesis (Figure 2.2) [11]. Other physical factors, such as exposure to harmful radiation may also cause genetic changes and lead to cancer. Exposure to radioactive materials can also increase the chances of mutation in genes [12].

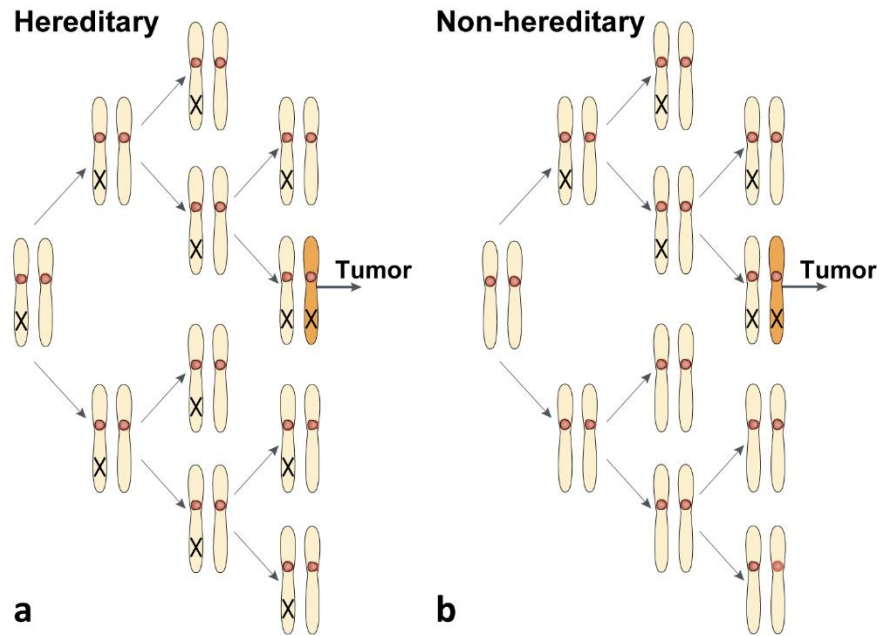


Figure 2.2. Two-hit tumor formation in both hereditary and non-hereditary retinoblastoma. (a) All retinoblasts are one-hit clones in hereditary retinoblastoma. (b) A 'one-hit' clone acts as a precursor to the tumor in non-hereditary retinoblastomas. Reprinted with permission [11].

### 2.3. Cancer Metastasis and Early Detection

Metastasis is the process how cancer spread in a body. Metastasis is the reason that makes cancer so dangerous. When a tumor forms in one particular organ of a body (also known as the primary site), cancer cells lose the ability to control cell differentiation and start to show malignant proliferation [13]. Integrins play an important role in cancer metastasis. Integrins are adhesion molecules present on cancer cell membrane that promote tumor cell attachment, migration, and invasion. Due to the mutation in integrin, cancer cells become invasive and enter host vasculature by local invasion. Thus, these cells are transferred to remote organ through the bloodstream and develop a secondary metastatic colony with the help of angiogenesis [14]. That is how cancer infiltrates other organs. Figure 2.3 illustrates the steps of tumor invasion and metastasis process [15]. There are two major steps involved in cancer metastasis. First, the cancer cells adhere to

extracellular matrix to survive and proliferate. Then, the cells penetrate the basement membrane and enter the bloodstream also known as intravasation. Usually, there are no symptoms seen on the outside to realize cancer metastasis. In most of the cases when a patient is diagnosed with cancer, unfortunately, it's too late to save the patient. So, the effective way to fight cancer is to detect cancer at an early stage.

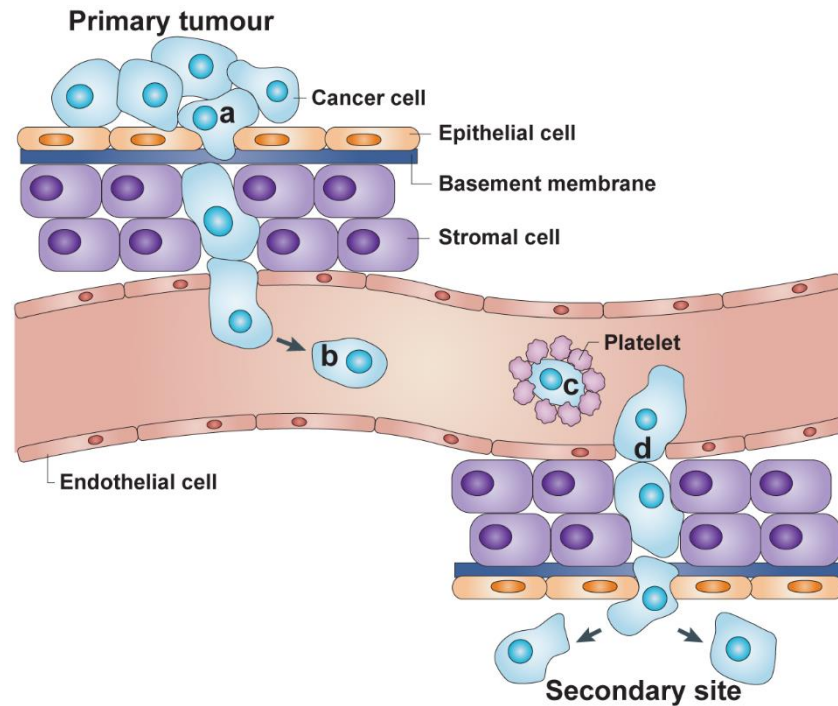


Figure 2.3. The process of cancer metastasis. (a) Metastatic cancer cells break free from the primary tumor and migrate to the vasculature. (b) Then the cancer cells keep flowing in the bloodstream until they find a metastasis-supporting site to colonize. (c) Platelets attack cancer cells in the bloodstream and protect them from the immune system. (d) Upon interaction with the secondary organ, cancer cells adapt to the local environment and proliferate in the secondary site. Reprinted with permission [15].

Early detection of cancer brings several advantages. Not only the survival rate is high if cancer is diagnosed early (Figure 2.4), but also the cost of treatment reduces significantly (Figure 2.5) [16, 17]. Being able to detect cancer at an early stage also allows the doctor to offer customized treatment to cancer patient which eventually favors quick

and complete recovery. Several methods have been reported to detect cancer cells from blood samples.

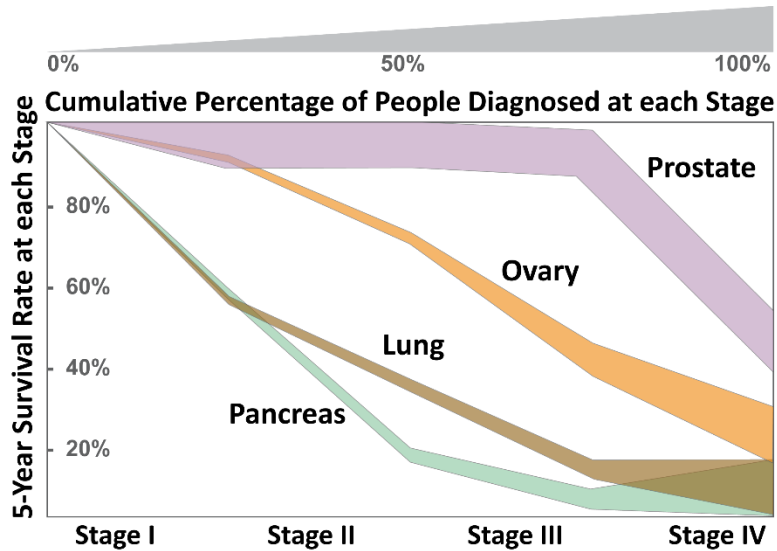


Figure 2.4. Five-year survival rate of cancer patients diagnosed at different stages of cancer. The survival rate decreases significantly as the disease progresses to advanced stages [16].

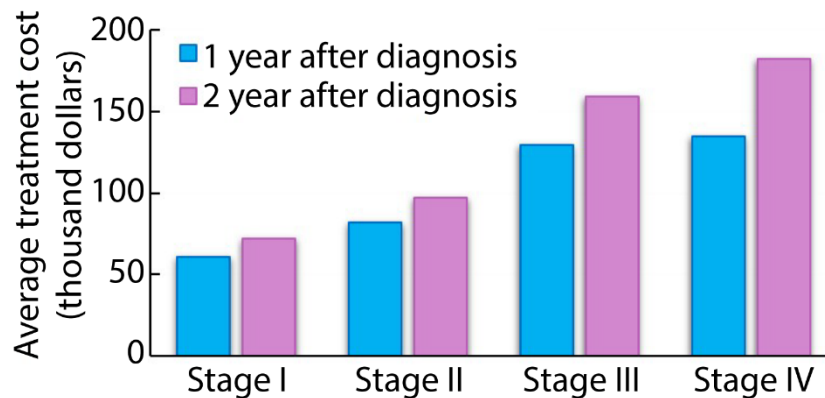


Figure 2.5. Breast Cancer treatment cost after one and two years of diagnosis. The treatment cost is higher for advanced stages of cancer. The cost of treatment also gets higher when it is diagnosed late [17].

Another important factor is to selectively capture cancer cells from blood samples in order to perform post-capture diagnosis. An effective post-capture analysis may lead to

faster diagnosis and accurate treatment. Needless to say that the detection method needs to be fast and sensitive for early stage of cancer.

#### **2.4. Cancer Biomarkers and EGFR**

There are certain proteins on cell membrane known as receptors. Epidermal Growth Factor Receptor (EGFR) is one of them. EGFR is responsible for cell signaling and cell proliferation. It is also responsible for stimulation of transport, activation of glycolysis, DNA, RNA, and protein synthesis [18]. It is reported that there are about 40,000 to 100,000 EGFR on a healthy cell membrane [19]. But the number of EGFR per cell tend to go high when a cell becomes tumorous. Many cancer cells including breast cancer, lung cancer, brain cancer, renal, and bladder cancer are reported to overexpress EGFR on the cell surface [20-22]. Naturally, this overexpression of EGFR can be used as an indicating factor in cancer which is why this is often used for selective detection of cancer. A surface protein that is used for cancer detection is called a biomarker. The number of EGFR biomarkers in cancer cells can be 10 to 100 times higher compared to a healthy counterpart depending on the type of cancer [23]. Hence, it is a popular choice for detection and therapy of several types of cancer. However, there are other biomarkers that can be used for cell detection. Table 2.1 includes a list of biomarkers present in different types of cancer cells.

Table 2.1. List of biomarkers overexpressed in different cancer. EGFR is a common biomarker for most of the cancers.

<b>Disease</b>	<b>Biomarker</b>
Breast Cancer	CEA, HER-2, EGFR
Cervical Cancer	Human Pappiloma Virus, EGFR
Lung Cancer	EGFR, KRAS, BRAF
Bladder Cancer	EGFR, HSP27, Annexin
Ovarian Cancer	EGFR, Haptoglobin $\alpha$ , CA-125
Esophageal Cancer	EGFR, Periplakin

## 2.5. Biomarker Detection Molecules

Two types of molecules are widely used to detect biomarkers based on their affinity interactions: (i) Antibody and (ii) Aptamer.

### 2.5.1. Antibody

Antibodies are proteins produced by the immune system. They bind to foreign objects and help to eliminate them from the system. Antibodies are widely used for imaging, detection, and therapeutic application of biomolecules. The most common type is the monoclonal antibody (mAb) which is produced by in vitro hybridization of immune cells and myeloma cells. Figure 2.6 shows a schematic of how monoclonal antibodies are produced in mouse [24]. A similar method is used to produce a large number of pure and specific antibodies for cancer diagnosis. Antibodies have been widely used in ELISA, flow cytometry, immunohistopathology, western blotting, and immunofluorescence imaging [25, 26]. Antibodies are also used for affinity-based cancer cell capture, isolation, and selective drug delivery applications [27].

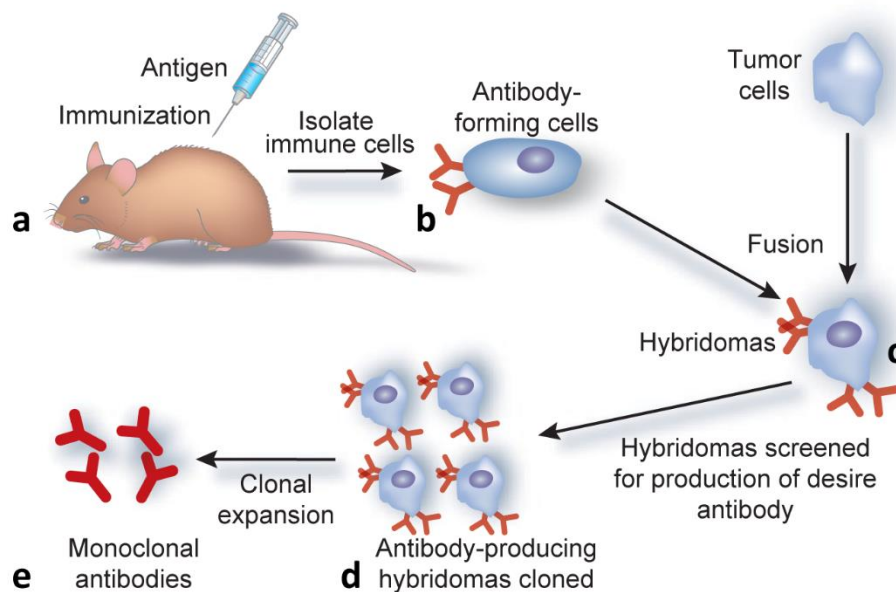


Figure 2.6. Schematic representation of the production of monoclonal antibodies through hybridization method. (a) Immunization of mice with antigen stimulates immune cells which produce antibodies that recognize the antigen. (b) Immune cells are isolated. (c) Antibody-producing cells are fused with tumor cells to generate immortalized hybridoma cells. (d) Antibody-secreting hybridoma cells are screened and amplified by clonal expansion. (e) Extraction of monoclonal antibodies. Reprinted with permission [24].

### 2.5.2. Aptamer

Aptamers are chemically synthesized DNA/RNA molecules that conformally bind to specific target molecules. They can be single or double stranded chain of oligonucleic acids or peptide molecules. Aptamers are also commonly used for detection of proteins, biomolecules and cancer biomarkers [28, 29]. Aptamers are produced by a method called the systematic evolution of ligands by exponential enrichment (SELEX) [30]. Figure 2.7 shows a schematic of the SELEX process. Briefly, a target cell is introduced into a nucleic acid pool containing various types of DNA/RNA. Then the positively selected molecules are separated and amplified by polymerase chain reaction (PCR) method. In the next

cycle, the selection is performed from the positively selected nucleic acids. This cycle is repeated several times until a few highly selective molecules are found.

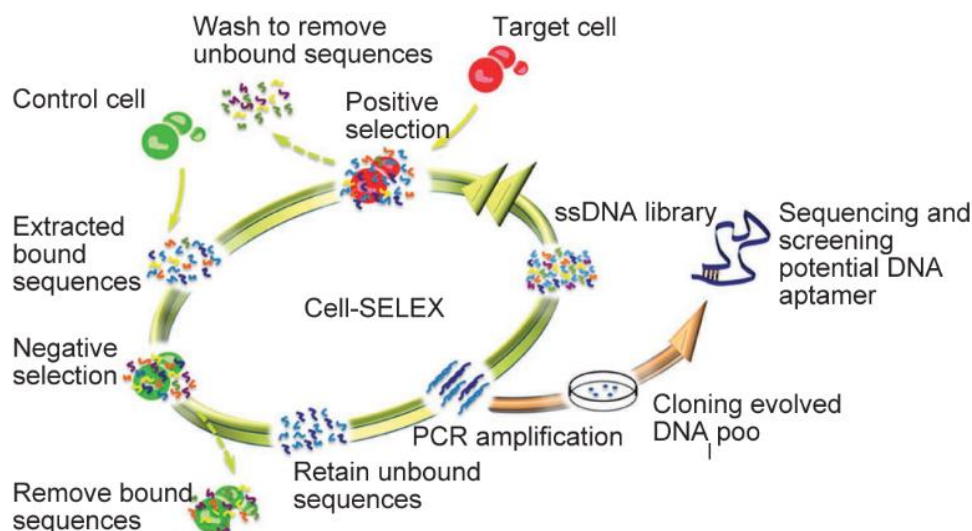


Figure 2.7. Schematic representation of DNA aptamer selection using SELEX. DNA sequences having specific recognition to target cells are evolved to enrich the selection pools. The enriched pools are cloned and the positive clones are sequenced to identify individual aptamers. Reprinted with permission [30].

The advantages of aptamer over antibody really depend on the type of applications. Aptamers are smaller in size and have a smaller footprint which makes it easier to pack them at a high concentration on a surface. In addition, aptamers are chemical stable. On the other hand, antibodies are widely used because it is easy to conjugate antibody with other molecules. Also, antibodies are not subjected to nuclease degradation. Table 2.2 compares a few benefits of these biomarker detection molecules.



Table 2.2 Comparison of antibody and aptamer.

<b>Aptamer</b>	<b>Antibody</b>
Smaller in size	Comparatively larger
Highly selective	Comparatively low selective
In vitro production	In vivo production
More difficult to conjugate	Easy to conjugate
Chemically stable	Require strict environment for reaction and stability

## 2.6. Cancer Detection Devices

Several cancer cell detection devices have been developed to capture and isolate cells from blood and tissue samples. The devices can be categorized into three sections in terms of the detection scheme: (i) physical or mechanical property-based detection, (ii) biochemical interaction-based detection, and (iii) image-based detection. The physical property-based detection methods are comparatively faster. On the other side, the biological property-based detection methods offer more selectivity. Image-based detection methods have the advantage of automation capability.

### 2.6.1. Mechanical Sorting

Usually, cancer cells have different physical properties such as size, elasticity, and deformability. Different types of cancer cell lines derived from brain, lung, breast, prostate, and liver have been studied and isolated based on these physical characteristics. ScreenCell developed a technique named “Isolation by Size of Epithelial Tumor cells (ISET)” using a microporous membrane [31]. The detection scheme is based on the fact that certain tumor cells are larger in size than the blood cells. In this method, a porous sieve is used to filter out the small cells from large ones. Larger cancer cells remain on

one side of the membrane and the smaller blood cells such as erythrocytes (RBC) and leukocytes (WBC) falls through the membrane pores. Figure 2.8 shows an illustration of the size-based isolation scheme. The advantage of such method lies in their simplicity. Several other works have been developed to filter cancer cells based on similar working principle [32-34]. In most of the cases, nanofabrication tools are used to fabricate microporous filters and a microfluidic channel is often used to guide the flow of samples.

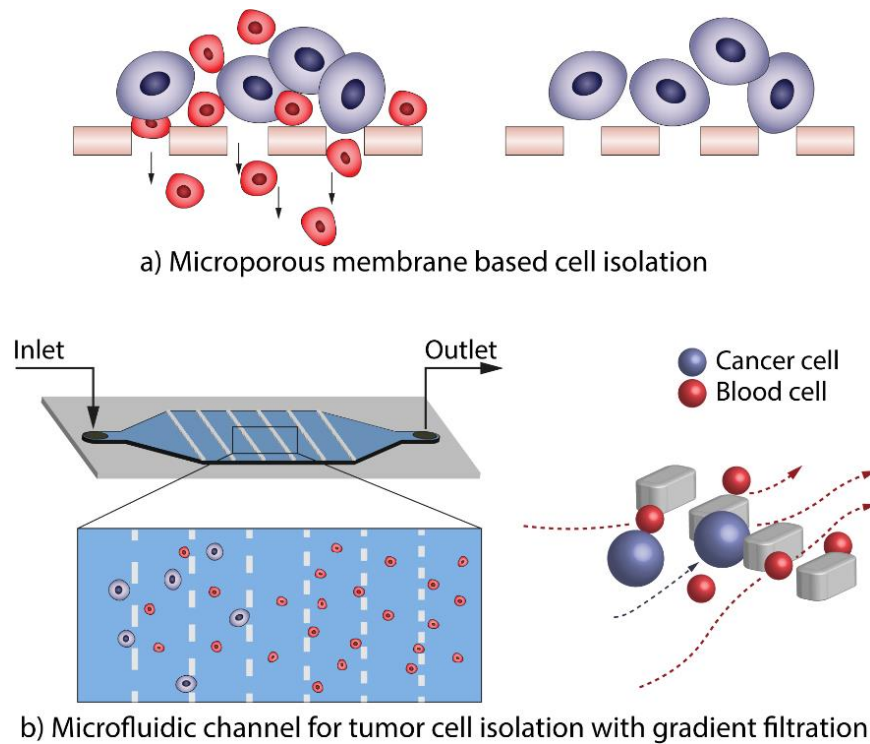


Figure 2.8. Schematic representation of size-based cancer cell isolation methods. (a) Microporous membrane isolating larger tumor cells (purple) from red blood cells (red). (b) A microfluidic device to sort cancer cells using gradual filtration method. A schematic of the gradual filtration process is shown at the bottom left. Series of micropost structures fabricated in PDMS to block large cancer cells from passing through (right).

Another approach to isolate cancer cells from blood cells is to probe their elastic property. It is reported that when a cell becomes cancerous, the stiffness and the elasticity of the cell membrane changes [35, 36]. Several micropore-based methods have been

developed to probe the deformability of cells to isolate them. The method also has the advantage of single-cell analysis. The working principle is very straightforward. The cells are allowed to deform by applying an external force through mechanical constriction or hydrodynamic pinching (Figure 2.9). Then the deformation is measured and analyzed to distinguish different cells. In a micropore device, a membrane is fabricated and a small pore is drilled in that membrane. The diameter of the pore is usually slightly smaller than the diameter of the target cells. The device is immersed in an ionic solution and cells are allowed to pass from one side of the membrane to the other with the help of a pump. An external electric field is applied to measure the ionic current through the pore. When a cell passes through the pore, it creates a drop in the ionic current. Thus, each cell translocation event is registered as an ionic current signature as shown in Figure 2.9.

A similar concept is applied in case of hydrodynamic pinching devices. Here, a hydrodynamic stress is applied on the cells from two sides using sheath flows and a high-speed camera takes snapshots of the deformed cells as they pass through a narrow channel. The deformation of each cell is calculated by image processing and the number of target cells is quantified. These single-cell analysis devices are good for sensitive and high throughput detection of cancer cells.

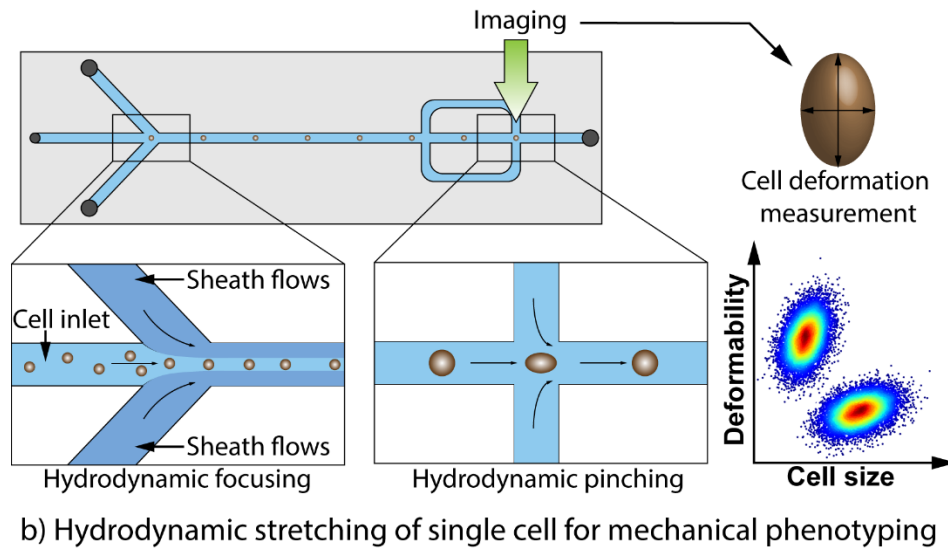
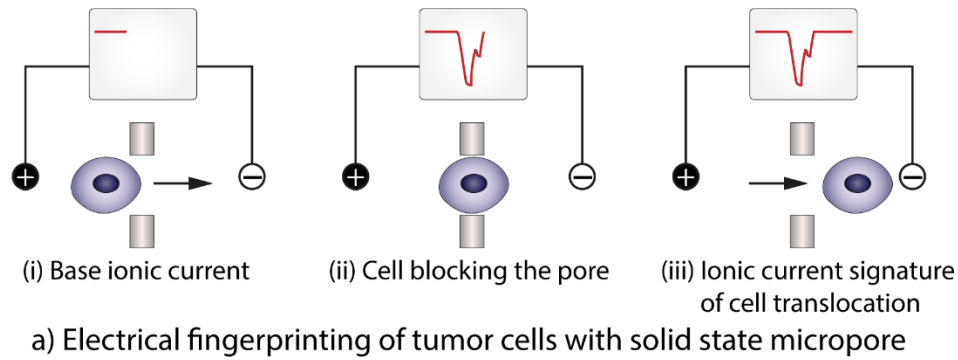


Figure 2.9. (a) Working principle of a micropore sensor to isolate cancer cells from blood cells by ionic current signature. (i) Base ionic current measurement (red signal) for open pore. (ii) An ionic current drop is registered when the pore is blocked by the cell. (iii) A complete cell translocation is recorded as an electrical current fingerprint. (b) Schematic representation of hydrodynamic stretching of single cell to measure cell deformability. A narrow stream of sample cells is formed in a microfluidic channel using sheath flow. The sheath fluids hydrodynamically focus the cell in the middle of the channel. The cell gets deformed by the shear from two sides known as ‘hydrodynamic pinching’. A high-speed camera takes snapshot of the deformed cell and then the deformability is calculated by image analysis. Cells having different size and deformability appears as different clusters in the scatter plot [37, 38].

Cancer cells can also be separated from blood samples based on cell mass or inertia. The most common approach is the centrifugation technique. In this method, a

mixture of cells with different mass is placed in a tube. The tube is spun at high speed in a centrifuge. After centrifugation, heavier cells settle at the bottom and comparatively lighter cells keep floating (Figure 2.10 a). A similar principle is utilized in spiral microfluidics and vortex-based label-free cell isolation devices. These methods are called inertia-based separation. In a spiral microfluidic channel, cells are flown from the center of the device to the outward direction (Figure 2.10 b). Due to the curved geometry of the microfluidic channel, the cells experience a combination of inertial lift and drag forces. This causes a lateral separation of the cells having different mass while they flow through the channel. Heavy cells tend to flow near the channel wall with the smaller radius of curvature (inner wall) and the lighter cells flow near the outer wall of the channel [39]. In some cases, the walls of the spiral channel can be slanted to achieve better separation capability. Warkiani et al. demonstrated a slanted spiral microfluidic device for label-free isolation of breast cancer cells from blood samples [40, 41]. Dino Di Carlo and his team developed Vortex microfluidic technology based on inertial focusing for label-free isolation of prostate circulating tumor cells [42, 43]. A schematic representation is shown in Figure 2.10c. In this device, a straight channel with series of rectangular extended regions are used to create local vortex flows to temporarily trap heavy cells. Figure 2.10 summarizes different inertia-based cell separation devices.

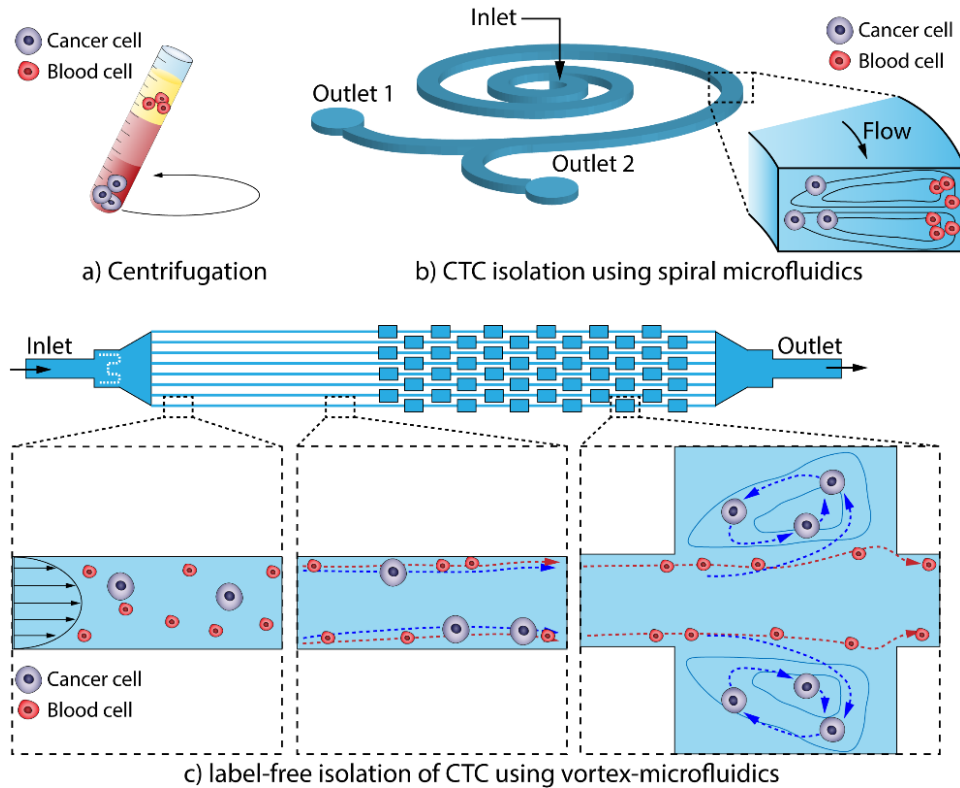


Figure 2.10. Schematic representation of cell density-based isolation methods. (a) Centrifugation method to separate heavy cells from lighter ones. Heavy cells form a palette at the bottom of the tube because of the large centrifugal force generated in the centrifuge. (b) Spiral microfluidics for cell sorting. Reprinted with permission [44]. A mixture of cells is flown in a spiral microfluidic channel from the center to the outward direction. The inset shows the cross-section of the channel with flow patch. Cancer cells and blood cells are collected from outlet-1 and outlet-2, respectively. (c) Label-free enumeration of cancer cells in an inertia microfluidic device. Reprinted with permission [45]. Cell samples are pre-filtered in the channel (inset-1). The velocity profile of the flow pushes the cells toward the side of the channel (inset-2). The heavier tumor cells (purple) gets trapped in the vortex region and smaller blood cells continue to flow through the channel (inset-3).

The main advantage of these physical property-based cell isolation devices is being a label-free technique. The samples do not have to be tagged with any other molecules. It does not require any pre-processing of samples. The viability of cells is also good since they do not have to be tagged with any other molecules. However, in many

cases, the physical difference between cancer and healthy cells are not always obvious and mechanical methods may not be the best approach to identify cancer cells [46]. These methods can provide information about the presence of tumor cells but cannot always identify the type of cancer cells. In order to understand the specifics of cancer cells, we need to exploit their immunochemical properties.

### **2.6.2. Affinity-based Detection Devices**

Cancer cells can be detected from the protein expression on the cell membrane too. The presence of certain types of biomolecules and their number on the cell surface can indicate whether the cell is cancerous or not. These biomolecules are called biomarkers. Compared to the physical attribute-based detection, biomarker-based detection provides much more information about the type of cancer cell, the stage of cancer progression and the immune response of the cells to certain drugs. As discussed before, the most important element to identify cancer biomarkers is antibody and aptamers. Different types of particles (fluorescent or magnetic) are selectively attached to cancer cells and then the cells are characterized using fluorescence imaging or magnetic sorting.

The most common method to isolate cancer cells using fluorescence particle is called Fluorescence Activated Cell Sorting (FACS) [47]. In this method, cells are pre-tagged with fluorescent dye. In most cases, a primary antibody is attached to the cell surface receptors and then a secondary antibody conjugated with a fluorescent particle is attached to the primary antibody. A laser excites the fluorescent molecules on the cell surface while they are traveling in a continuous flow and a detector picks up the optical signal. The intensity of fluorescence and scattered light are then analyzed to sort the cells. Figure 2.11 shows a schematic of FACS.

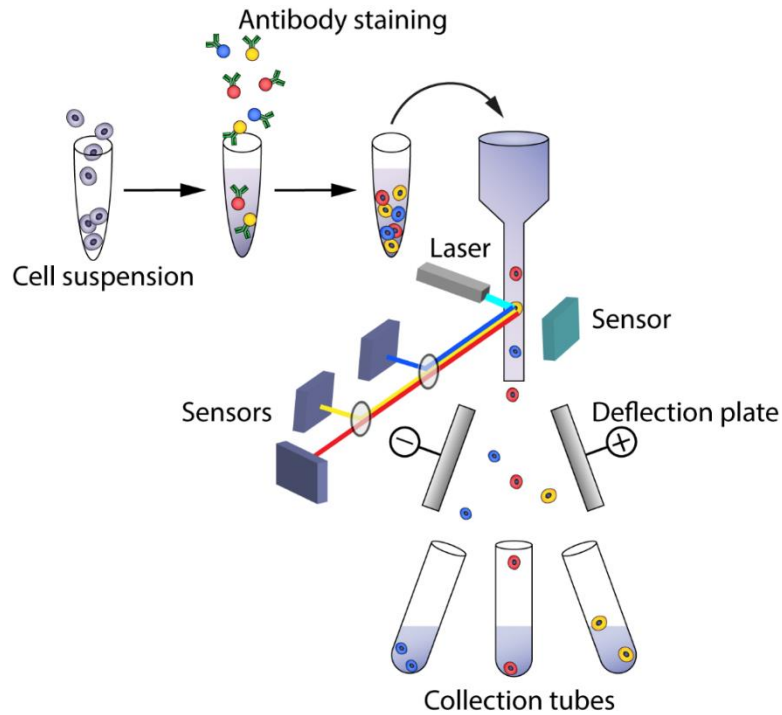


Figure 2.11. Schematic illustration of FACS. Fluorescent antibodies are selectively attached to sample cell mixture. Individual cells are scanned by a laser. Multiple sensors capture scattered and fluorescent light. A computing system analyzes the color spectra and deflects the cells into separate collection tubes using a charged deflection plate.

A similar approach is adapted for magnetic particle-based sorting. Magnetic nanoparticles are selectively attached to the cell surface via antibody and then an external magnetic field is applied to sort the cells based on their particle expression. A schematic is shown in Figure 2.12.



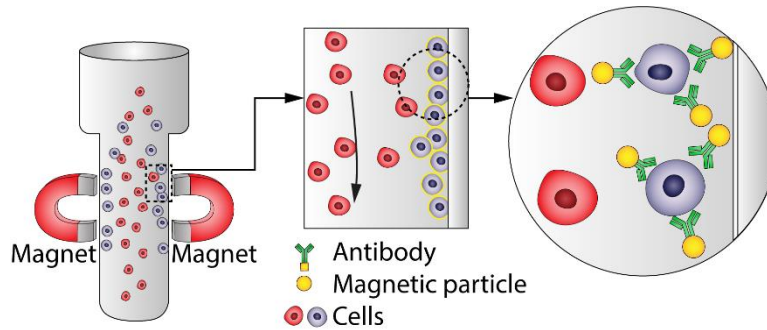


Figure 2.12. Schematic illustration of magnetically activated cell sorting (MACS). Magnetic particles (yellow) selectively attach to cancer cells via antibody (green). An external magnetic field attracts the magnetic particle coated cells towards the cell container wall while the rest of the cells are flushing out. The inset shows a schematic of the magnetic particle attachment via antibodies.

Due to the advancement in lab-on-a-chip technologies, these cell detection methods are being implemented in microfluidic platforms. Kruger et al. developed a microfluidic device to sort fluorescently activated cells [48]. Pamme et al. isolated human cervical cancer (HeLa) cells with magnetic particles [49]. Hoshino et al. reported the isolation of human colon and breast cancer cells with antibody-conjugated magnetic nanoparticle in a microchip device [50]. Recently, Myklatun et al. successfully demonstrate a microfluidic device isolating intrinsically magnetic cells [51]. The versatility of microfluidic technology also makes it possible to combine multiple detection approaches into a single device. Toner et al. developed a CTC-iChip device by combining two cell separation methods into one device (Figure 2.13). A size-based preliminary sorting was followed by magnetophoresis for separation of CTCs from WBCs, RBCs, and platelets [52].

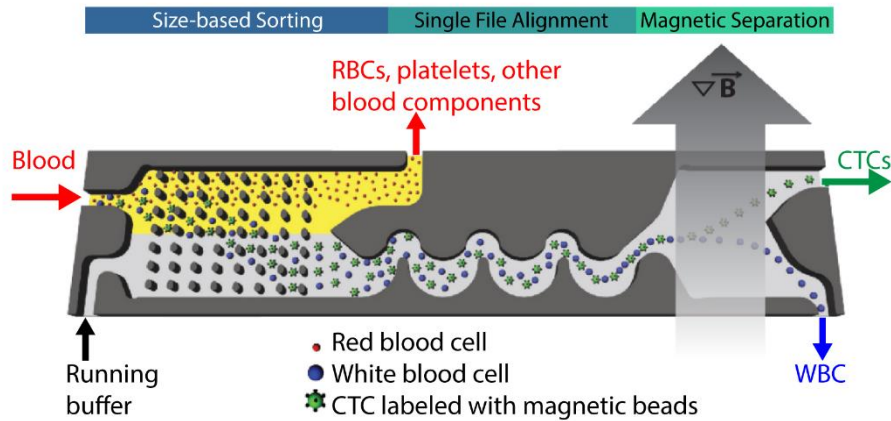


Figure 2.13. A microfluidic chip combining hydrodynamic cell sorting, inertial focusing and magnetically operated sorting. Hydrodynamic sorting section isolates larger cells (WBCs and magnetic particle coated CTCs) from RBCs, platelets and other blood components. Then the external magnetic field deflects magnetic particle coated CTCs from WBCs. Reprinted with permission [52].

Cancer cell surface biomarkers are also used to capture cells on a surface. Different capture molecules (aptamers or antibodies) are immobilized on the device surface and then cells are introduced into the device, typically in a microfluidic chamber. Target cells with overexpression of biomarkers are attached to the surface immobilized capture molecules and the rest of the samples are washed away. A schematic illustration is shown in Figure 2.14.

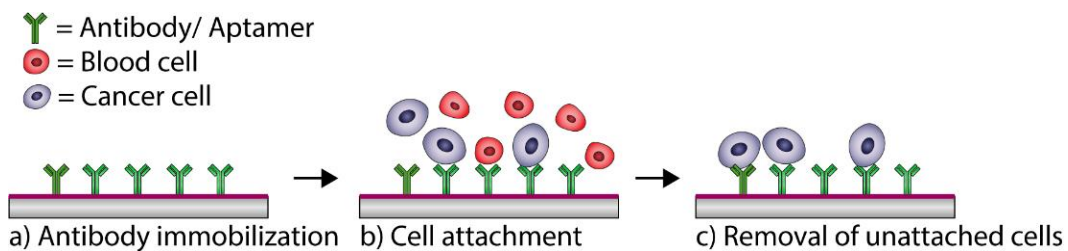


Figure 2.14. Schematic representation of cancer cell capture on an antibody-functionalized surface. (a) Antibody immobilization on the surface. (b) Cells interacting with the functionalized surface. (c) Cancer cells captured on the surface immobilized antibodies.

The advantage of affinity-based detection methods is that it not only allows selective cell enrichment but also captures all the target samples in one place. This is suitable for imaging and post-capture analysis. The microfluidic platform also provides portability. One limitation of the surface capture devices is that these devices work well with cells having an overexpression of biomarkers on the surface. Otherwise, the sensitivity of the device is limited to the number of biomarkers available on the cell membrane that the surface immobilized antibodies can attach to. To address that, several surface engineering techniques have been implemented to enhance the cell to surface interaction. Toner et al. developed a micropost device to isolate cancer cells from blood samples [53]. Other microfluidic devices incorporating microstructures like fishbone patterns, cylindrical posts, and triangular pillars have also been reported to isolate circulating tumor cells from blood samples [54-56] (Figure 2.15). These structures modulate the fluid flow inside the device and increase cell surface interactions in order to capture the cells on the functionalized surfaces.

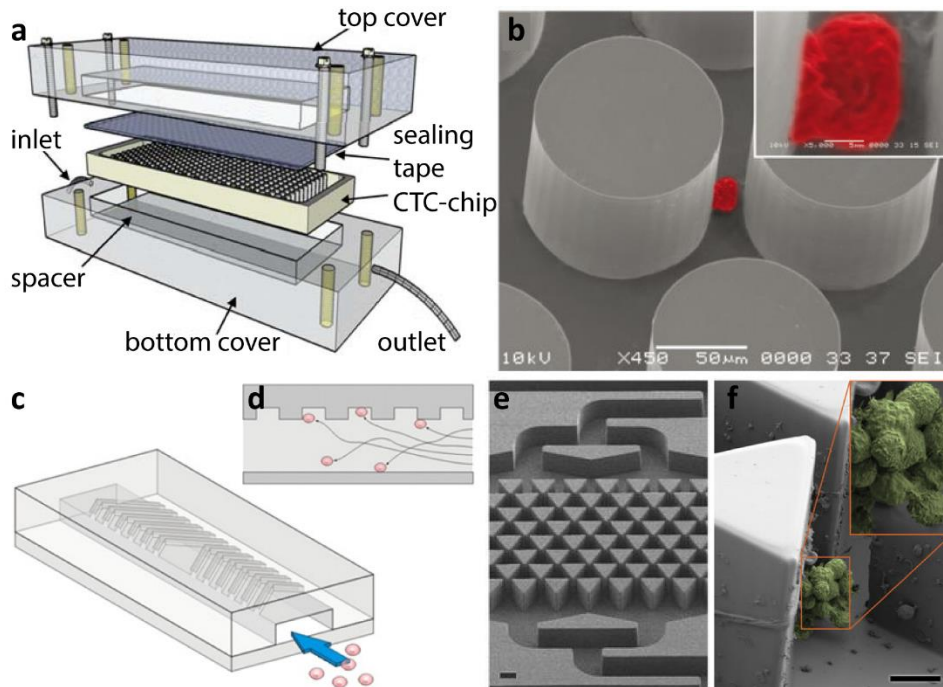


Figure 2.15. Affinity-based microfluidic devices to isolate circulating tumor cells. (a) Schematic of a CTC-microchip device micropost arrays [53]. The device is sealed with the manifold with adhesive tapes. (b) Cancer cell captured on anti-EpCAM functionalized silicon micropost in the CTC-chip device; inset shows a magnified view of the captured cell (red). (c) Herringbone-chip containing fishbone patterned structure inside channel ceiling [54]. The channel is functionalized with antibodies. The herringbone grooves generate chaotic microvortices inside the channel to increase interaction with cells. (d) Flow visualization inside HB-chip. (e) Microfluidic Cluster-Chip for cancer cell detection [56]. SEM micrographs show multiple rows of shifted triangular pillars creating consecutive cluster traps for CTCs; scale bar = 60  $\mu\text{m}$ . (f) High-magnification image of Cluster-Chip with a CTC cluster captured in the device; scale bar = 60  $\mu\text{m}$ . Reprinted with permission.

Although these devices show improved performance in terms of cell isolation capability, these are difficult to fabricate. To enhance the cell surface interactions, nanotexturing have emerged in the field of microfluidic cell capture devices. Several researchers have introduced nanotexture in the devices to enhance the cell capture performance. The presence of patterned topography or nanotexture on the surface increases surface area and interactions with the target samples.

## **2.7. Nanotextured Substrates for Cancer Detection**

We see nanotexture everywhere in nature. Nanotexture controls the wettability, adhesion, structural color, and chemical functions of a surface. Nanotexture is seen in human body too and it plays a role in cancer metastasis. The nanotexture in the basement membrane helps to anchor cancer cells through cell adhesion molecules and facilitate cell growth [57]. This has drawn much attention for cancer cell adhesion and cell enrichment applications. Nanotextured substrates have been fabricated and chemically modified to capture and isolate tumor cells [58, 59].

Different types of nature-inspired nanotextured patterns have been explored to control surface properties. It has been well researched that nanotexture controls the surface hydrophobicity, the optical properties, surface charge, and energy. For example, the hydrophobic surface of lotus leaves was understood to be the effect of surface texture. Similar structures have been explored to control the wettability of surfaces [60]. Understanding the nanotexture present on the wings of dragonflies and butterflies enabled researchers to fabricate anti-reflective surfaces to increase the efficiency of photovoltaic devices [61, 62]. Recently, the convex and concave patterns on rose petals have been mimicked on a PDMS surface to increase the efficiency of tumor cell capture [63].

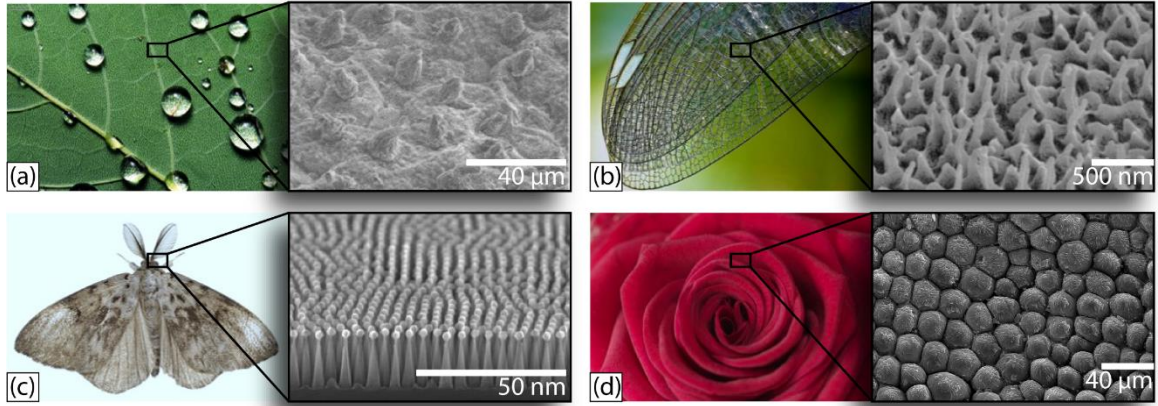


Figure 2.16. Effect of nanotexture in nature. (a) Water droplet floating on a hydrophobic surface of lotus leaf due to its surface texture. (b) The nanotexture on transparent dragonfly wing controls transmission of light. (c) The nanotexture on moth eye is responsible for photon absorption. (d) A rose petal and the convex topography on the surface. The inset shows the SEM micrograph of surface texture [60-63]. Reprinted with permission.

The role of nanotexture in cell capture applications has been demonstrated by several research groups. Han et al. showed enhancement in human leukemia cell capture on a nanoparticle deposited surface [64]. Zhang et al. used electrospinning technique to create a  $\text{TiO}_2$  nanofiber-based cell capture assay [65]. Yoon and his team deposited graphene nanosheets on a silicon substrate for sensitive capture of breast cancer cells [66]. There are other methods to create nanotexture. Basically, the methods of fabricating a nanotextured surface can be categorized into two sections (i) bottom-up and (ii) top-down. The above-mentioned methods are all part of bottom-up approaches which includes deposition of particles or materials on the surface. On the other hand, the top-down approaches involve the removal of materials from the surface to create a pattern. This method often includes some type of dry or wet etch, surface grinding, and chemical polishing process. Fabrication of nanowire substrate with deep reactive ion etching (DRIE) [67], etching of silicon substrate to create nanodot and nanopillar structures [68, 69], and

reactive ion etch (RIE) of glass substrate are a few examples of top-down fabrication method [57, 70]. Figure 2.17 includes different types of nanotextured surface used for cell capture application.

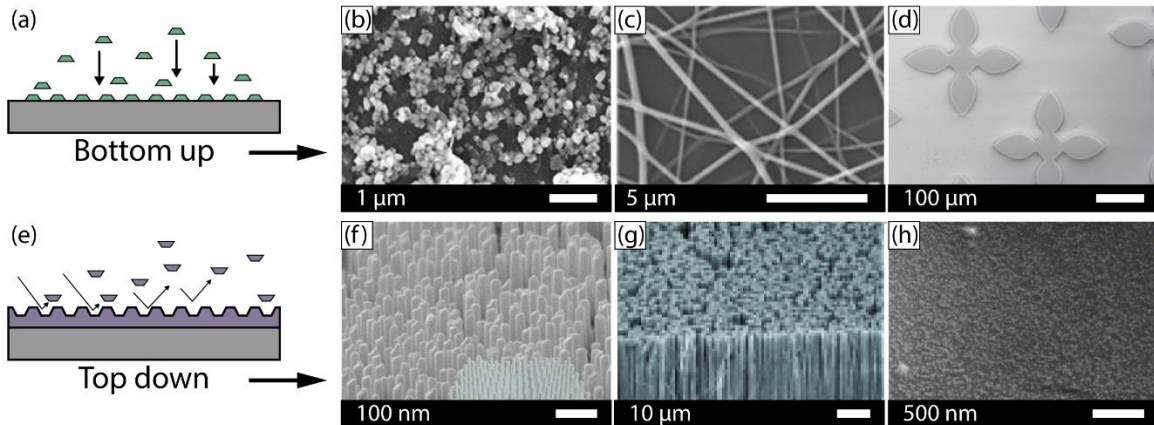


Figure 2.17. Methods of fabricating nanotextured surfaces. (a) Schematic of bottom-up approach where materials are deposited on a substrate to make a nanotextured surface. Examples include: (b) Deposited ZnO nanoparticle to study osteoblast cancer cells [71], (c) TiO<sub>2</sub> nanofiber deposited on a silicon substrate with electrospinning method to create CTC capture assay [65], and (d) Chemically deposited graphene-oxide for CTC isolation [66]. (e) Schematic representation of top-down approach that involves removal of the substrate with wet and dry etching methods. Examples include: (f) Reactive ion etched quartz silicon nanowire structure [67], (g) Silicon nanopillars array [69], and (h) Sandblasted glass with nanotexture on the surface [70]. Reprinted with permission.

Each of these fabrication methods has their own advantage and disadvantages. In most of these methods, it requires specialized tools and laboratory environment to fabricate the nanotexture. The type of materials that can be processed in nanofabrication tools is also limited due to compatibility issues. Some tools are also very expensive to maintain and operate. Integration of these nanotextured materials into microfluidics brings another challenge. The integration process often involves an irreversible permanent bonding to maintain a good seal which poses a problem to access cells and perform post-capture analysis. Researchers have been continuously trying to come up with a fast and

easy process to create nanotextured substrates and integrate that into microfluidic chips for cell studies. The selection of material is also important for microfluidic integration. In the past decades, PDMS has been a widely accepted material for nanotexture and microfluidic device fabrication. PDMS is a silicone-based flexible polymer which can be used to replicate patterns and structures from a solid mold. The process is called 'soft lithography'.

## **2.8. Soft Lithography for Microfluidic Device Fabrication**

Soft lithography is a technique for fabricating or replicating structures using elastomeric stamps and molds [72]. The most common material used for replicating structures in a moldable polymer is polydimethylsiloxane (PDMS). The process of fabricating features from a conformable mask is called 'replica molding'. Figure 2.18 illustrates the replica molding process. A solid surface called master contains the inverted shape of the desired pattern (Figure 2.18(a)). Then PDMS is mixed with a curing agent in a specific ratio to make a polymer paste. The ratio of PDMS to curing agent controls the stiffness of the final polymer. A higher portion of curing agent will make the PDMS stiffer after curing. The mixture is degassed to get rid of any air bubbles. Then the poured PDMS mixture is heated at 150°C for 10 minutes (Figure 2.18 b). This hardens the polymer and it can be peeled off from the surface (Figure 2.18 c).



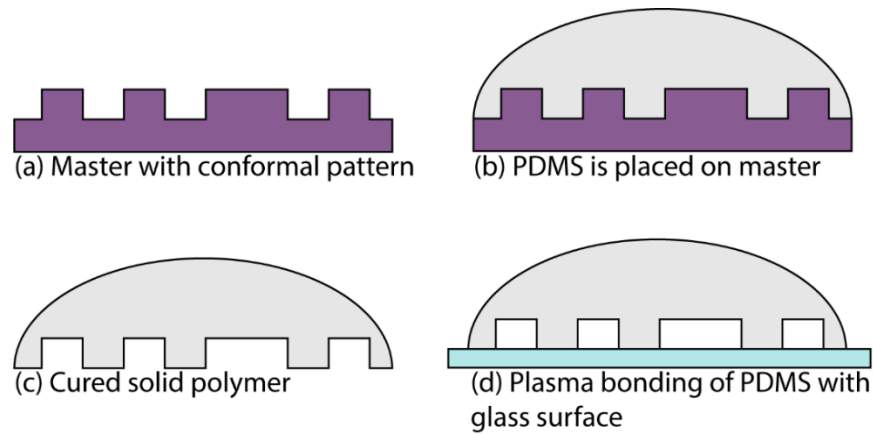


Figure 2.18. Replica molding process. (a) A solid surface with the inverted pattern called ‘master’. (b) PDMS mixture (PDMS and curing agent) is poured on master and then thermally cured. (c) The thermally-cured solid PDMS is peeled off from the master. (d) PDMS is oxygen-plasma bonded with a flat glass surface for microfluidic devices.

Replica molding is commonly used in making microfluidic channels, creating micron and sub-micron structures from textured surfaces, and for contact printing applications. There are certain advantages of using PDMS for replica molding. PDMS is cheap, chemically inert, and biocompatible which makes it convenient to use in bioengineering applications. PDMS also has good chemical and thermal stability. It is permeable to gas and optically transparent down to 280 nm wavelength of light. In many microfluidic applications, PDMS is irreversibly sealed to a glass surface with oxygen plasma treatment. Recently, PDMS surfaces are chemically modified to explore cell capture applications.

## 2.9. Imaging-based Cancer Diagnosis

The state of the art techniques for imaging-based cancer diagnosis includes computerized tomography (CT) scan, magnetic resonance imaging (MRI), mammogram, ultrasound, and X-ray imaging [73]. Even though these tools can non-invasively detect tumors in many patients, the detection ability is depended on the size and density of the tumor tissue. Moreover, these methods are not very effective for early diagnosis of cancer

since the number of diseased cells is extremely low at that stage and the sensitivity of these tools is not in cellular scale. Recently, researchers are investigating new imaging tools like positron emission tomography (PET) imaging to acquire molecular scale information from tumor samples [74]. Selective attachment of nanoparticles and magnetic particles through monoclonal antibodies are being explored to enhance the detection capability of these existing methods [75-77]. However, in many cases, patients are exposed to radiation and imaging agents which lead to other complications if the patient has any illness or a medical condition like pregnancy, allergy or is prone to side effects.

Another approach to detecting cancer is to directly image cells collected from biopsy samples. Only an optical image may not capture enough information to distinguish cancer cells. That's why cells are often tagged with fluorescent markers. Different fluorescent markers are available to stain cell nucleus, actin fibers, and chromosomes, and other components in the cytoplasm. These fluorescent images can be compared with known target samples and used for cancer detection. One such common approach is called fluorescent in situ hybridization (FISH). Recently FISH imaging was used to develop an automated cancer detection platform [78, 79]. The advantage imaging-based approach is that it can be automated with a pre-programmed microscope and computer system. Several research groups have developed automated cancer classification tools from fluorescently labeled tissue samples [80, 81]. Many image analysis software such as CellProfiler, CellXpress, and CellCognition are also available to analyze different cell phenotypes [82-84].

Apart from using static cell images for cell identification, analyzing cellular behavior and responses in different microenvironment can also provide significant information about cellular malfunctions. Cell migration and dynamic morphology are two important phenomena that provide insights about cancer formation. Cell migration is an important

biological process for development of nervous system, inflammatory response, and wound healing [85, 86]. It plays a vital role in cancer metastasis and proliferation. The cell migration mechanism is shown in Figure 2.19 [87]. Generally, cell migration occurs in three steps (i) protrusion (ii) translocation and (iii) detachment. The lamellipodia and filopodia in the cell membrane create a protrusion by actin polymerization with a combination of Brownian ratchet and cortical expansion mechanism. Once the protrusion adheres to the substrate, the cell body translocates forward through myosin interactions with actin filaments. The balance between two major acting forces directs the movement, (i) forward driving adhesion traction force and (ii) rearward pulling actin filament contraction force. Eventually, the cell translocates forward because the traction force is greater than the contraction force. Finally, the rear cell body detaches from the substrate by myosin-mediated actin filament contraction.

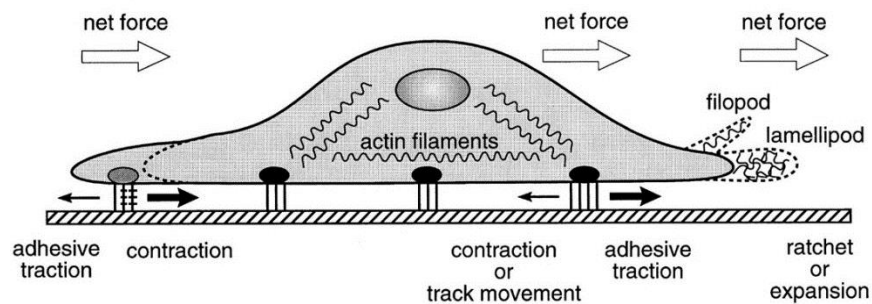


Figure 2.19. Illustration of different forces involved in cell migration. There are three major steps: protrusion, translocation and detachment. The protrusion of lamellipodia or filopodia starts by the force generated by actin polymerization. Translocation may occur by myosin interactions with actin filaments at the rear end. Finally, cell detaches from the rear which is accelerated by myosin-mediated actin filament contraction pulling on adhesion complexes. Reprinted with permission.

The dynamic behavior and motility of cell are stimulated by the genetic mutation. This is very important for cancer cells. Due to its increased growth rate and proliferation, cancer cells show enhanced activity and movement. This favors cell migration too. The

activity of cells on a surface can be modulated by bio-modification of the surface. We investigated this phenomenon in our research and used machine learning-based classification to distinguish cancer cells from healthy ones.

### **2.10. Machine Learning for Cancer Detection**

Machine Learning (ML) is the branch of artificial intelligence of getting computers to learn from past examples and to act without being explicitly programmed. In the past decade, machine learning has been used in self-driving cars, practical speech recognition systems, customized web search, and to understand the human genome. It allows computers to detect hard-to-discern patterns from large and complex datasets using various statistical, probabilistic, and optimization algorithms. Cancer has been characterized a heterogeneous disease consisting of numerous subtypes. The characteristics of each type of cancer at different stages of the disease are slightly different from one another. Therefore, machine learning methods have become a popular tool for researchers to model the progression and treatment of cancerous conditions [88, 89]. Large-scale patient-data are being analyzed to accurately predict future outcomes of a cancer type and offer customized medicine by analyzing DNA sequence, protein and gene expressions.

### **2.11. Nanopore and Molecular Dynamic Simulation for Label-free Detection of Protein**

Nanopore technology has been advanced substantially due to its advantages for single molecule detection and characterization capabilities. Nanopore sensors have been used for rapid sequencing of DNA, detection of proteins and metal ions, and protein transportation studies [90-93].

### **2.11.1. Fabrication of Nanopore**

Earlier, biological pores such as alpha-hemolysin were used for nanopore experiments. Later, solid-state pores became more popular due to their mechanical and chemical stability. Advancement of nanofabrication tools made it easier to fabricate solid-state nanopores and also to modify the pore diameter, thickness, and the material of the membrane. Figure 2.20 shows a simple schematic of solid-state nanopore fabrication in a silicon nitride membrane. Other materials such as  $\text{Al}_2\text{O}_3$ ,  $\text{SiO}_2$ , and graphene have also been used for nanopore fabrication for different purposes. Basically, a thin film is grown or deposited on the silicon wafer. Then the substrate (silicon) is etched from the back side to create a free-standing membrane. Finally, a small pore is drilled with high energy ion or electron beam. Focused ion beam (FIB) and Transmission electron microscope (TEM) are most commonly used for nanopore drilling. However, the pore can be fabricated using high-resolution photolithography for higher throughput. The inner wall of the nanopore can also be coated with biomolecules to study protein interactions.

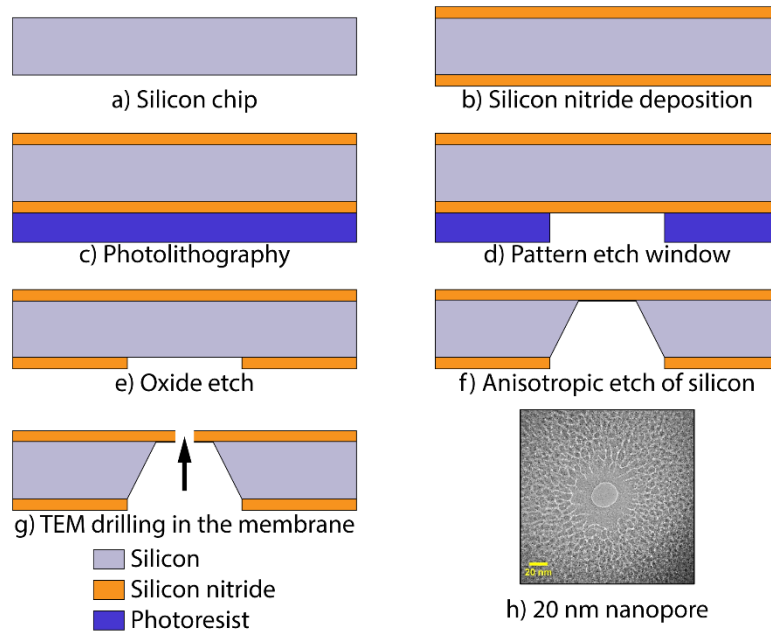


Figure 2.20. Schematic flow of nanopore fabrication. (a) A cross-section of a silicon chip. (b) Silicon nitride deposition on both sides on the silicon chip. (c) Photoresist coating on one the backside silicon nitride. (d) An etch window is patterned in the photoresist layer using photolithography. (e) The patterned window is transferred to silicon nitride hard mask using dry etch. (f) Silicon is anisotropically etched with wet etchant (tetramethylammonium hydroxide, TMAH) through the etch window. The crystallographic orientation of silicon creates a slanted sidewall. (g) TEM drilling of the silicon nitride membrane. (h) and TEM micrograph of a 20 nm diameter nanopore.

### 2.11.2. Working Principle of Nanopore

The working principle of protein detection using nanopore is very straightforward. A biological or solid-state nanopore is immersed in an ionic solution. An external electric field is applied and protein molecules are passed through the nanopore. The translocation of protein molecules and any interactions with the pore wall is then captured in the ionic current profile measured by the external patch clamp system. The velocity of the protein depends on the charge of the protein, the electric field applied in the system, and protein-pore interactions. The charge of the protein depends on the isoelectric point of the protein and the pH of the ionic solution. Thus, the size of the pore, the strength of the electric field,

the concentration and pH of the ionic solution, and the surface coating on the inner pore wall can play important roles in protein transport studies. Figure 2.21 shows a demonstration of label-free protein detection using solid-state nanopore at different pH.

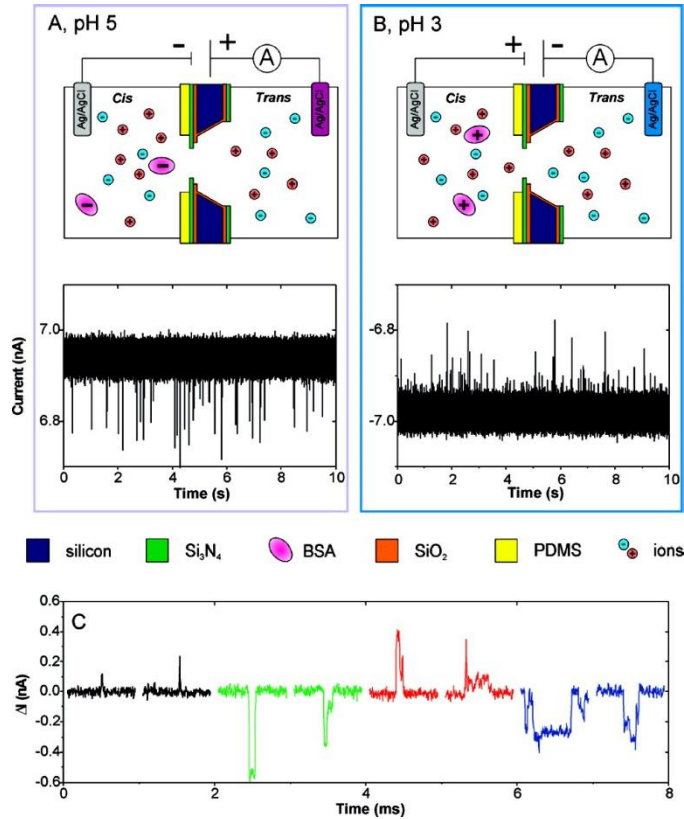


Figure 2.21. Protein translocation through nanopore [94]. Bovine serum albumin, BSA was passed through the nanopore in an ionic buffer with pH 5 (labeled A) and pH 3 (labeled B) at 50 mV. (C) Time-resolved current signal of BSA (black and green) and avidin (red and blue) at pH 3 (black and red) and pH 6 (green and blue), respectively. Reprinted with permission.

### 2.11.3. Molecular Dynamics Simulation of Nanopore

Proteins play crucial roles in carrier transport, molecular motors, cellular structural support etc. Several nanopore-based protein studies have been conducted through different experiments. However, some information such as the interatomic interactions of protein and the nanopore cannot be measured with experimental setups. The

translocation dynamics, and also the structural stability of the confined protein inside nanopore cannot be calculated from laboratory experiments. Molecular Dynamic (MD) simulation can predict these events that take place inside the nanopore. Computer simulations can be used for better understanding of molecular assemblies and interactions. MD simulation is suitable for analyzing the dynamic properties of the transport mechanism, time-dependent responses, and flow-based experiments.

The foundation of MD simulation is built on Newton's third law. An MD simulation actually predicts the position of every atom in a molecule by analyzing all the forces acting between any atom-pairs. First, a model of the system is built with atomic-scale precision. The position of the atoms and the energy is estimated using Newtonian and quantum mechanical calculations. Then the next state of the molecule is calculated based on the state of all the atoms in the system at the previous step. An MD simulation has the advantage to calculate atomic interaction in small timescale. Figure 2.22 shows a basic flowchart of the calculation steps for an MD simulation.

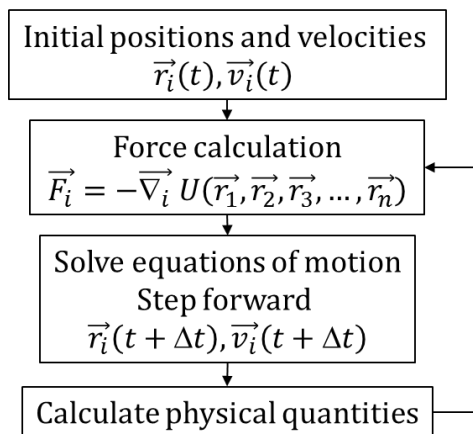


Figure 2.22. Flowchart of a molecular dynamic simulation calculation.



#### **2.11.4. Molecular Dynamics Simulation Software**

Two software is popularly used for MD simulations (i) Nanoscale Molecular Dynamics (NAMD) and (ii) Visual Molecular Dynamics (VMD). NAMD is used for parallel programming to simulate large bio-molecular systems. The program uses CHARM++ models specially developed for nucleic acids, peptides, and protein simulations to calculate interatomic forces. VMD is used for visualization of simulated biomolecules and structural analysis.

## Chapter 3

### 3. One-Step Fabrication of Flexible Nanotextured PDMS as a Substrate for Selective Cell Capture

#### 3.1. Introduction

Advances in nanofabrication techniques including chemical and reactive ion etching, nano-embossing, chemical vapor deposition, and electrospinning have enabled the creation of surfaces with nanoscale topography (e.g. nanotexture) [57, 58, 61, 65, 95, 96]. These engineered surfaces have provided unique opportunities to imitate the physiological nanotexture found *in vivo* and explore biomimetic cell-surface interactions. Over the last decade, the characteristic advantages of nanotextured substrates including increased surface areas [97-99], enhanced surface activity [100], and tunable surface energies [101] have been leveraged to modulate phenotypic behaviors including cell attachment [102-104], viability [105, 106], migration [107], and differentiation [108].

Nanotextured surfaces are also gaining popularity in cancer cell capture applications [59, 109-111]. Taking advantage of increased surface areas, Yoon and colleagues introduced antibody-functionalized graphene nano-sheets and demonstrated efficient cancer cell capture from lung and breast cancer patient samples [66]. Zhang and colleagues demonstrated the application of nanotextured TiO<sub>2</sub> for cancer cell capture from colorectal and gastric patient samples [65]. Similarly, Wang and colleagues reported the use of 3D nanostructured silicon nanopillars for isolation of breast and prostate cancer cells [69, 112]. Cancer cell capture on aptamer-functionalized nanotextured surfaces has been demonstrated before [99, 113-115]. It has been shown that captured cells can be sub-classified as metastatic or non-metastatic by quantifying dynamic membrane ruffling behavior via real-time imaging [114, 116]. These observations underscore the important role that nanotopographic cues have in guiding cell behavior. Even though the advantages

of nanotextured surfaces are becoming increasingly evident for cellular explorations, there are practical considerations that must be addressed before these materials can be widely fabricated and used by researchers outside the materials science and engineering communities.

Conventional techniques to create nanotextured substrates require cleanroom facilities and specialized fabrication equipment [67, 96, 117]; these requirements impose a significant entry barrier for researchers that wish to incorporate nanotextured materials into their experiments but do not have access to the needed facilities. For cell capture experiments, important considerations include (i) precise sample introduction and routing, (ii) controlled washing, and (iii) experimental reproducibility. Microfluidic technologies have been shown to effectively meet these requirements [53, 54, 56]; however, the leak-proof integration of nanotextured substrates with microfluidic channels, coupled with the optimization requirements of microfluidic experimental workflows can be challenging to implement.

To simplify nanotextured substrate fabrication and provide a user-friendly solution for microfluidic integration, this work presents a one-step molding approach to achieve nanotexture on a flexible polymer surface without requiring specialized nanofabrication equipment. The nanotextured polymer was then integrated into a magnetically sealed microfluidic architecture with a tool-free approach that can be easily implemented in a standard laboratory setting. As a proof of concept, nanotextured polymer surfaces were functionalized with antibodies targeting epidermal growth factor receptor (EGFR) and demonstrated improved A549 lung cancer cell adhesion and enhanced capture on a nanotextured surface compared to a functionalized plain polydimethylsiloxane (PDMS) surface. This work also reports on cell capture selectivity from a multi-cellular mixture and demonstrate an efficient nucleic acid isolation process to support downstream genomic

analysis. The overarching goal of this work is to provide an experimental platform that can be easily used in studies exploring cell-surface interactions and selective cell capture.

## **3.2. Experimental**

### **3.2.1. PDMS Channel Fabrication**

Standard soft lithography and replica molding techniques were used to fabricate PDMS channels (Figure 3.1). Channels ( $L=10$  mm,  $W=1$  mm) were designed in AutoCAD (v2007) and printed at high resolution into mylar transparency films (CAD/Art Service Inc.). Silicon wafers (100 mm diameter, p-type, single side polished) were spin-coated with SU-8 100 photoresist (MicroChem) at 3000 rpm to create a 100  $\mu\text{m}$  thick SU-8 layer which defined the height of the microfluidic channel. Wafers were then soft baked at 65 °C for 10 minutes and 95 °C for 30 minutes, cooled, covered with the printed transparency mask, and exposed to UV light centered at 365 nm. After post-exposure bake at 65 °C for 1 minute and 95 °C for 10 minutes, wafers were immersed in developer solution for 10 minutes (MicroChem) to remove non-crosslinked photoresist. Wafers were hard baked at 150 °C and allowed to cool. A ring (1.5 mm thickness, 90 mm OD, 80 mm ID) was laser cut (Epilog CO<sub>2</sub> laser) from a PMMA sheet (McMaster) and affixed to the surface of the wafer via pressure sensitive adhesive (3M). The attached PMMA ring was used to control the thickness of the PDMS block containing the microfluidic channel features. PDMS prepolymer (Sylgard 184, Dow Corning) was mixed thoroughly (10:1 base to catalyst ratio by mass) and placed under vacuum to remove entrapped bubbles. The PMMA ring cavity was filled with the bubble-free PDMS solution, gently covered with a transparency film, then covered with an additional piece of PMMA to ensure a flat surface, and finally cured at 75 °C for 6 hours. Fully cured PDMS was removed from the mold and cut to size ( $L=25$  mm,  $W=10$  mm) with a razor blade to fit into the cavity. Fluidic access ports were cored into the PDMS using a 2 mm diameter biopsy punch.

### 3.2.2. Replica Molding of Nanotextured and Plain PDMS surfaces

Flexible PDMS surfaces (nanotextured and plain) were fabricated by replica molding. Bubble-free PDMS was prepared as described above and poured onto the backside (nanotextured) or polished (plain) side of a silicon wafer. PDMS thickness was defined by the same PMMA cavity technique used in microfluidic channel molding process. Once the PDMS was cured, it was carefully removed from the wafer surface and stored in a dust free environment until use.

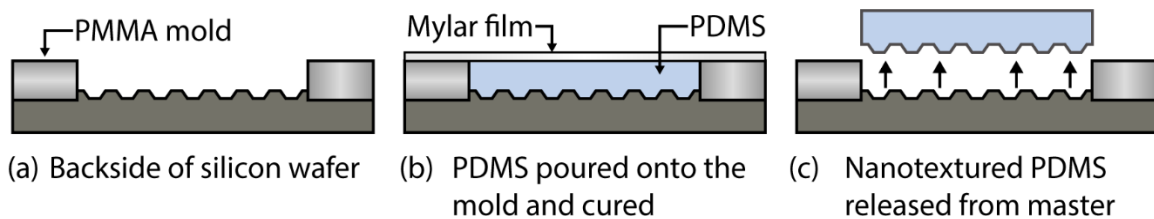


Figure 3.1. Workflow of replica molding (a-c). (a) The backside of a silicon wafer is used as the master for the nanotextured PDMS. A PMMA cavity is used to control the thickness of the PDMS block. (b) PDMS is poured into the PMMA cavity and a transparent mylar sheet is used at the top to maintain a flat surface on the other side. (c) Cured nanotextured PDMS block is released from the master.

### 3.2.3. Surface Texture Quantification and Imaging

A profilometer (XP200, Ambios Technology) was used to measure the surface roughness of the nanotextured and plain PDMS surfaces at room temperature. Scan resolution was 1 nm and 200  $\mu\text{m}$  lines were scanned on the surface with a stylus force of 10 mg at 10  $\mu\text{m}/\text{sec}$  scan speed. The RMS roughness ( $R_q$ ) was calculated from the profile to quantify surface. SEM micrographs of nanotextured and plain PDMS were acquired in low vacuum environmental mode on a FEI NOVA nanoSEM. Atomic force microscope (AFM) images were acquired in the non-contact mode using NCHR 10M tips to measure surface topography (Park XE-70).

### **3.2.4. Surface Area Calculations**

The surface area was calculated by the following method. Four neighboring points ( $z_1, z_2, z_3, z_4$ ) with pixel dimension  $h_x$  and  $h_y$  along corresponding axes were chosen. An additional point was assumed at the center of the rectangle with the mean value of corner pixels. Thus, four triangles were formed and the surface area was approximated by summing their areas. The area of one of the top triangles and eventually the surface area was calculated with the following formula:

$$A_{12} = \frac{h_x h_y}{4} \sqrt{1 + \left(\frac{z_1 - z_2}{h_x}\right)^2 + \left(\frac{z_1 + z_2 - 2z}{h_y}\right)^2}$$

$$A = A_{12} + A_{23} + A_{34} + A_{41}$$

### **3.2.5. Contact Angle Measurements**

The contact angles on plain and nanotextured PDMS surfaces were measured using a goniometer (Ramé-Hart) with a 2  $\mu$ L droplet of deionized (DI) water. Images were captured using DROPimage software with at least five images per surface and at least four independent replicate samples for each condition.

### **3.2.6. Nanotextured PDMS Silanization**

PDMS surfaces were cleaned with isopropyl alcohol (IPA), triple washed with DI water, and dried with filtered  $N_2$ . The surfaces were treated with oxygen plasma (Nordson MARCH, AP600 plasma system) for 20 seconds to enhance hydrophilicity then immediately immersed into a 4% (v/v) 3-mercaptopropyl trimethoxysilane (MPTS, Sigma-Aldrich) in 95% ethanol solution for 30 minutes at room temperature on a rocker platform. The surfaces were sequentially rinsed with ethanol and DI water then dried with filtered  $N_2$ . The silanization process resulted in surfaces decorated with thiol functional groups.

### **3.2.7. Neutravidin Conjugation and Antibody Attachment**

After thiol functionalization, surfaces were treated with 50 µg/mL maleimide-activated neutravidin (Thermo) in phosphate buffer saline (PBS) for 1 hour at 37 °C. The maleimide-activated neutravidin covalently attached to the thiol-functionalized surface through the maleimide-thiol coupling at neutral pH. Unreacted neutravidin was removed with three PBS washes and the substrates were stored in PBS at 4 °C for up to one week before use. Biotinylated anti-EGFR antibody (Thermo) was added to the neutravidin-conjugated PDMS surfaces at a concentration of 20 µg/mL in PBS and incubated at 37 °C for one hour. Control surfaces were incubated with 20 µg/mL biotinylated antibody which was isotype-matched to the primary antibody. Antibody attachment was performed immediately before experimentation followed by PBST (PBS with 0.05% Tween-20) wash and blocking with 1% (w/ v) bovine serum albumin in PBST for 1 h.

### **3.2.8. Reversibly Sealed Easy Access Modular (SEAM) Platform Integration**

PMMA housings (L=45 mm, W=30 mm), McMaster Carr) were designed in AutoCAD and cut with a CO<sub>2</sub> laser. Individually cut layers (1.5 – 2 mm) were laminated together using pressure sensitive adhesive films to create rigid plastic housings containing L=25 mm, W=10 mm, H=1.5 mm cavities PDMS pieces containing the microfluidic channels (top) and the flexible nanotextured or plain PDMS surfaces (bottom). Laser-cut holes at the four corners accommodated cylindrical rare earth magnets (K&J Magnetics, 2.54 mm diameter, thickness=1.58 mm) which were then glued in place. Rare earth magnets were embedded in the PMMA and oriented such that the top and bottom housings had opposite magnetic poles facing one another to achieve a simple and self-aligned latching mechanism. The housings compressed the top PDMS channel against the PDMS capture surface and achieved a leak-proof seal (Figure 3.5(b)). Magnetic latching allowed the SEAM platform to be easily sealed and resealed as needed. The

tubing was connected to the channel using a barbed fitting (McMaster), and a syringe pump was used to control fluid flow (Harvard Apparatus). The magnetic latching mechanism was sufficient to create a seal that could withstand the maximum possible flow rate for our syringe pump (5 mL/min) corresponding a pressure drop of ~ 1.5 psi (100 mbar).

### **3.2.9. Cell Culture**

Human small cell lung cancer cells (A549) were obtained from ATCC and cultured in complete RPMI-1640 according to manufacturer's directions. Human umbilical vein endothelial cells (HUVEC) were obtained from Lonza and maintained in EndoGRO culture media according to manufacturer's directions. Cells were seeded at 5,000 cells cm<sup>-2</sup> in T-75 culture flask and were passaged at ~70% confluence. Media was replaced every 24-48 hours. Prior to experiments, cells were enzymatically disassociated from the culture flask, counted with an automated cell counter (Countess-II, Thermo), and diluted to the desired concentration in serum-free media. All cells were used between passages 5 to 10.

### **3.2.10. Cell Capture Experiments**

PDMS surfaces were integrated into the SEAM platform and functionalized with anti-EGFR antibody to target EGFR on the surface of A549 cells. Control experiments included a biotinylated, non-targeting antibody which was isotype-matched to the anti-EGFR antibody. A549 cells were labeled with fluorescent dye (CellTracker green, CMFDA) at 5 μM concentration for 3 hours prior to experiments to aid in visualization. Cells were counted, resuspended in serum-free media, and then incubated in the functionalized channels at 200 cells/mm<sup>2</sup> seeding density for 20 minutes at 37 °C. Channels were washed using a syringe pump for 2 minutes to remove unattached cells from the surface. The channels were then imaged with a fluorescence microscope



(Olympus IX81, with ORCA-Flash 4.0 camera) using Olympus CellSens software and counted using *ImageJ*.

For specificity experiments, A549 cells and HUVECs were labeled with green (CellTracker green, CMFDA) and orange dye (CellTracker orange, CMTMR), respectively, at 5  $\mu$ M concentration for 3 hours. The A549 and HUVECs were combined at a ~1:1 ratio in serum-free media. The cell mixture was introduced into the channels at the desired density, incubated for 20 minutes, and imaged pre and post wash.

### **3.2.11. Threshold Fluid Shear Stress**

A549 cells were captured on a functionalized PDMS surfaces as described above and exposed to defined fluid shear stress to assess adhesion strength. Shear stress within the capture channel (L = 10 mm, W= 1 mm, H = 0.1 mm) was simulated in COMSOL (v5.2a) as a function of flow rate via parametric sweep (50, 100, 150, and 200  $\mu$ L/min). The surface roughness to channel hydraulic diameter ratio,  $\epsilon/D_h$ , was small (0.003) with Reynolds number < 10 and therefore effects of nanotexture on shear stress were not considered in our model. Cells were exposed to shear stress ranging from 0 to 50 dyne/cm<sup>2</sup> for 1 minute and the number of cells retained in the channel after shear exposure was quantified. The data were fit to a 4 parameter sigmoidal curve, and the threshold shear stress required to dislodge 50% of captured cells,  $\tau_{50\%}$ , was determined for each substrate ( $n > 3$  independent experiments for each). Data are reported as average and standard deviation of the extracted  $\tau_{50\%}$  value from three independent experiments.

A COMSOL simulation was performed to simulate wall shear stress within the microfluidic channel (L = 10 mm, W = 1 mm, H= 0.1 mm) under different flow rates. Results are shown in Table 3.1.

Table 3.1. Simulated wall shear-stress as a function of flow rate

Flow rate ( $\mu\text{l}/\text{min}$ )	Shear stress ( $\text{dyne}/\text{cm}^2$ )
10	0.77
50	3.87
100	7.74
200	15.47

### 3.2.12. Four-parameter Curve Fitting

The following equation was used in 4-parameter sigmoidal fit.

$$y = A + \frac{B - A}{1 + \left(\frac{10^C}{x}\right)^D}$$

Where,  $x$  and  $y$  are the independent and dependent variable; the 4 fitting-parameters are,  $A$  = Final asymptote,  $B$  = Initial asymptote,  $C$  = Point of inflation, and  $D$  = Slope.

The reduced chi-squared value was used to compare the goodness of fit.

$$\text{reduced chi - square } \chi_v^2 = \frac{\chi^2}{\nu},$$

$$\text{chi - square, } \chi^2 = \sum \frac{(O_i - C_i)^2}{\sigma_i^2},$$

$$\text{degrees of freedom, } \nu = n - m$$

Where,  $\nu$  = degree of freedom,  $n$  = number of observations,  $m$  = number of fitted parameters,  $\sigma$  = variance,  $O$  = Observations,  $C$  = Calculated data.

### 3.2.13. Cell Adhesion Improvement and Cell Capture Enhancement Calculation

The threshold shear stress required to dislodge 50% of captured cells, was denoted as  $\tau_{50\%}$ . Then  $\tau_{50\%}$  was calculated for both nanotextured ( $\tau_{50\%, \text{nanotextured}}$ ) and plane PDMS ( $\tau_{50\%, \text{plane}}$ ) surface. Then the improvement in cell adhesion was calculated with the following equation

$$\text{Percent increase in attachment} = \frac{\tau_{50\%, \text{nanotextured}} - \tau_{50\%, \text{plane}}}{\tau_{50\%, \text{plane}}} \times 100\%$$

Cell capture improvement on functionalized nanotextured PDMS versus plain PDMS was calculate using the following equation.

$$\text{Percent increase in cells captured} = \frac{N_{\text{nanotextured}} - N_{\text{plain}}}{N_{\text{plain}}} \times 100\%$$

Where,  $N_{\text{nanotextured}}$  is the number of cells captured on nanotextured surface per  $\text{mm}^2$  and  $N_{\text{plain}}$  is the number of cells captured on plain surface per  $\text{mm}^2$ .

### 3.2.14. Nucleic Acid Extraction

After cell capture, nucleic acid isolation was performed using a Quick-RNA MicroPrep kit (Zymo-Research) and quantified using a NanoDrop-1000 Spectrophotometer (Thermo). Two methods were compared. In the first method, the PDMS substrate with attached cells was removed from the SEAM platform and transferred directly into a microtube containing 400  $\mu\text{L}$  of lysis buffer and then processed according to the manufacturer's directions. In the second method, in-channel lysis was done by flowing 400  $\mu\text{L}$  of lysis buffer through the channel, collected in a tube, and then processed according to the manufacturer's protocol. At least three independent experiments were done for each method.

### **3.2.15. Statistical Analysis**

Statistical significance was assessed with two-tailed unpaired *t*-test or ANOVA with Bonferroni post-hoc analysis as indicated in the text. Data are reported as the average  $\pm$  standard deviation with *p-value* < 0.05 considered statistically significant. The number of independent replicates is indicated in the text.

## **3.3. Results and Discussion**

### **3.3.1. Nanotextured PDMS**

Silicon wafers are commonly used in soft lithography to create microfluidic channel features and PDMS is a chemically inert, optically transparent, and ubiquitous material in microfluidic applications [54]. To create nanotextured surfaces without requiring specialized equipment, a replica molding technique was used with the unpolished backside of a silicon wafer as a template and PDMS as the fabrication material. The molding process transferred the intrinsic nanotexture from the unpolished wafer ( $R_q = 702 \pm 73$  nm) to the PDMS polymer. As shown in Figure 3.2, the topographical features of nanotextured surfaces were imaged with scanning electron microscopy (SEM) and compared with plain PDMS surface molded from the polished side of a silicon wafer. Atomic force microscopy (AFM) was used to measure the surface roughness of the plain PDMS (inset to Figure 3.2(a)). The roughness of the nanotextured surface was beyond the measurement limit of the AFM and profilometer was used to assess the roughness of the surface (Figure 3.3).  $R_q$  for nanotextured and plain PDMS was found to be  $682 \pm 102$  nm and  $3.7 \pm 1.5$  nm, respectively (*p-value* < 0.05, *n* = 8).

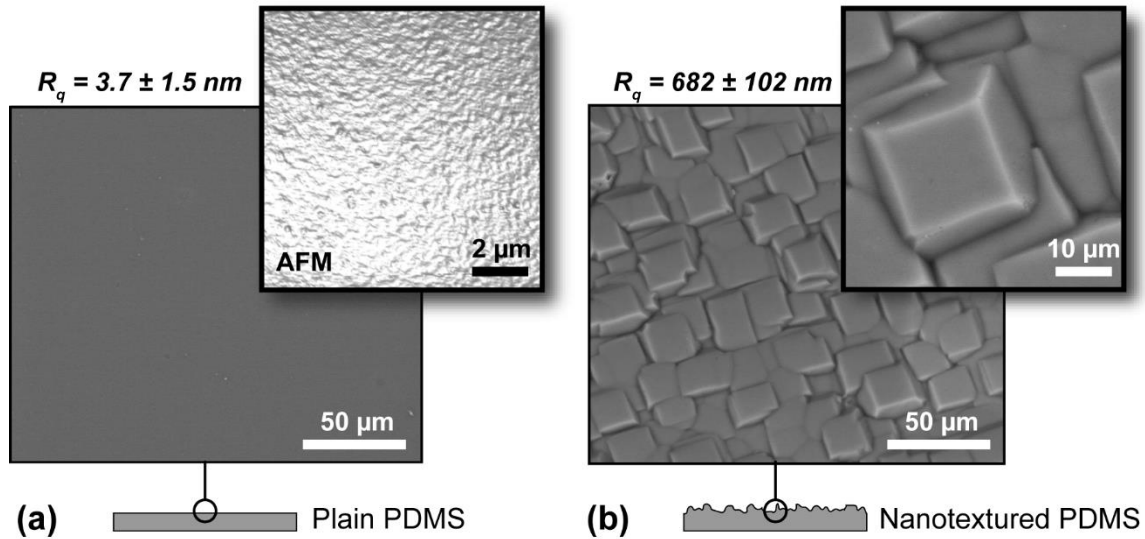


Figure 3.2. Surface topography of plain and nanotextured PDMS captured at 30° angle in low vacuum. (a) SEM micrograph of plain PDMS. The inset shows the surface topography measured with AFM. (b) SEM micrographs of nanotextured PDMS. A high magnification image of the surface topography is shown in the inset.

Obtaining  $R_q$  values equivalent to our method using conventional additive or subtractive nanofabrication techniques involves processing steps that must be optimized for every material (e.g. silicon, glass, polymer), and care must be taken to quantify differences in resulting surface compositions. Reactive ion etching (RIE), nanoparticle coating, electrospinning and other deposition methods have been used to create nanotexture from 20-200 nm and multiple rounds are required to achieve the equivalent roughness of our molding process. The replica molding from the backside of a silicon wafer is a simple, one-step process that can be done in any laboratory. If other  $R_q$  values are desired, the backside of the silicon wafer can be modified to expand the range of nanotexture transferred to the polymer during replica molding. For example, anisotropic etching of the silicon wafer can create surfaces with higher  $R_q$  while dry-etch methods can be used to decrease  $R_q$ . Although additional processing is required, the resulting backside

silicon surfaces can be used indefinitely as templates outside of a nanofabrication laboratory.

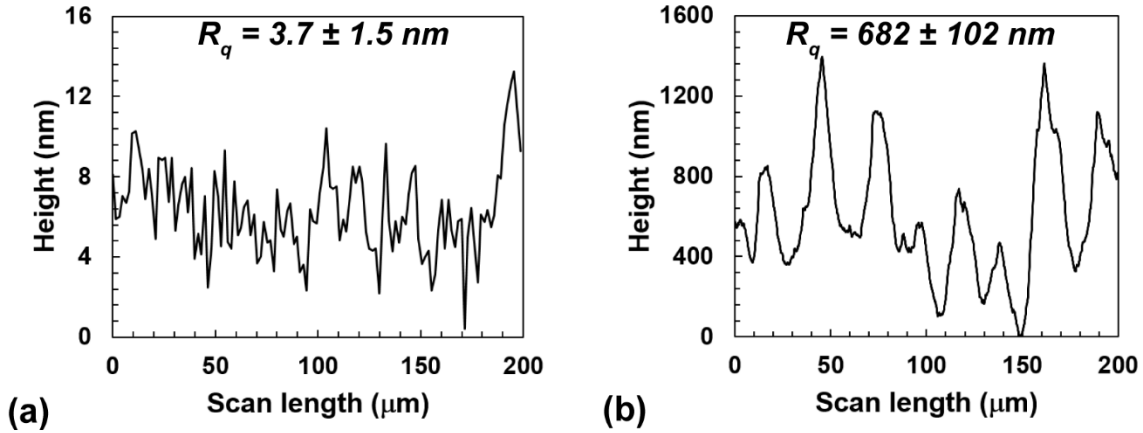


Figure 3.3. Surface roughness profiles of plain and nanotextured PDMS measured by the profilometer. The scale in the vertical axis of the two profiles represents the difference in surface roughness. The root mean square (RMS) roughness ( $R_q$ ) of nanotextured and plain PDMS was  $682 \pm 102 \text{ nm}$  and  $3.7 \pm 1.5 \text{ nm}$ , respectively ( $p\text{-value} < 0.05$ ,  $n = 8$ ).

### 3.3.2. Effect of Nanotexture on Surface Area

To calculate the increase in the surface area resulting from a two-order of magnitude enhancement in  $R_q$ , a triangulation-based image analysis technique was used as described by Necas and coworkers [118]. In this approach, an image of each surface was calibrated with measured surface roughness and the individual pixel intensity of the two-dimensional image was used to calculate the topographic parameters. Four adjacent pixels were chosen on the surface with a common corner at the center. The intensity of the center corner was approximated to be the mean intensity of the four points and rectangular pyramid shape was formed; the corresponding surface area was calculated from the four lateral triangles. The total surface area for the plain and nanotextured PDMS was found to be  $0.034 \text{ mm}^2$  and  $0.063 \text{ mm}^2$  for the same footprint of  $200 \text{ μm} \times 172 \text{ μm}$ , corresponding to an 85% increase in surface area.

PDMS is an intrinsically hydrophobic material ( $\theta_c = 110^\circ$ ) while the thiol group is slightly polar. Contact angle measurements showed that nanotextured PDMS ( $\theta_{nanotextured} = 49.7^\circ \pm 3.6$ ) became more hydrophilic after thiol functionalization compared to plain PDMS ( $\theta_{plain} = 61.3^\circ \pm 6.8$ ) (see Figure 3.4); the ~20% decrease in contact angle of thiol-functionalized surfaces can be attributed to the increased surface area and corresponding increase of surface-bound thiol groups [119]. Thiol groups were used to attach neutravidin molecules to the surface to create a versatile method to functionalize a surface using biotin-conjugated reagents (e.g. antibodies, proteins, or aptamers).

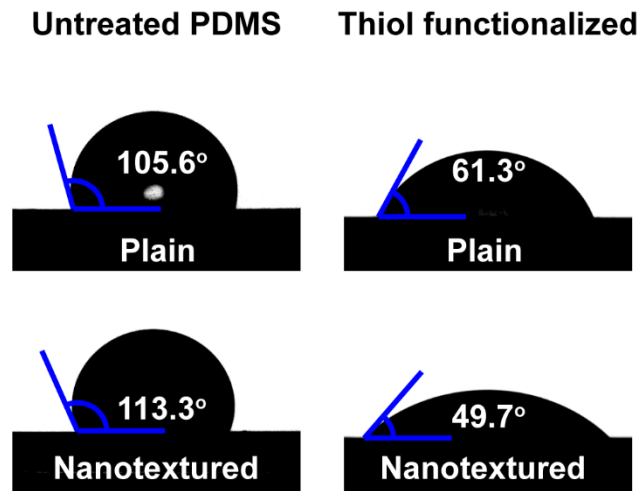


Figure 3.4. Change in water contact angle on plain and nanotextured PDMS surfaces due to silanization process. The contact angles ( $\theta_c > 90^\circ$ ) of untreated plain and nanotextured PDMS suggest a hydrophobic material. Both of the surfaces changed to hydrophilic ( $\theta_c < 90^\circ$ ) after thiol functionalization. Because of the increased surface area on the nanotextured surface, the thiol functionalization made nanotextured PDMS more hydrophilic ( $\theta_{nanotextured} = 49.7^\circ \pm 3.6$ ) compared to plain PDMS ( $\theta_{plain} = 61.3^\circ \pm 6.8$ ) as is shown by the contact angle measurements.

### 3.3.3. Nanotexture and Surface Composition

Energy-dispersive spectroscopy (EDS) analysis was used to verify that molding from the backside of a silicon wafer did not alter the composition of the resulting

nanotextured PDMS (Table 3.2). The molecular weight of Hydrogen (H) is too small to be detected with EDS and the trace aluminum (Al) was attributed to the sample holder. Our data showed no significant change in composition between the plain and nanotextured PDMS. In contrast to other texturing methods (e.g. CVD, chemical etch, electrospinning), our simple replica molding technique allowed us to transfer texture to the bulk material without altering the surface composition.

Table 3.2. Elemental analysis of plain and nanotextured PDMS (C<sub>2</sub>H<sub>6</sub>OSi)<sub>n</sub>

<b>Element</b>	<b>Plain PDMS (%wt.)</b>	<b>Nanotextured PDMS (%wt.)</b>
<b>C</b>	46.1 ± 0.31	45.07 ± 0.31
<b>Si</b>	24.96 ± 0.17	26.31 ± 0.16
<b>O</b>	28.35 ± 0.25	28.05 ± 0.24
<b>Al</b>	0.57 ± 0.09	0.57 ± 0.04
<b>Total</b>	100.00	100.00

### **3.3.4. Integration of Nanotextured PDMS into microfluidic architecture**

Microfluidic devices used for cell culture studies are typically permanently bonded together (*i.e.* channel feature layer attached to culture surface) using chemical modification or mechanically assembled with screws or retaining clips. To simplify integration efforts, a modular platform containing a magnetic latching mechanism was utilized to enable self-aligned, tool-free, sealing and resealing of microfluidic devices (Figure 3.5). Replica molded PDMS substrates (textured or non-textured) were sealed against a PDMS slab that contained microfluidic channel features using a two-piece PMMA housing assembly with magnets of opposite polarity embedded in each layer [120]. The magnets enabled a simple, self-aligned compression seal and could be easily disassembled and reassembled as needed. Magnetic latching also allowed easy access



to cells within the device and facilitated a simplified process for isolating cells and nucleic acids for downstream analysis.

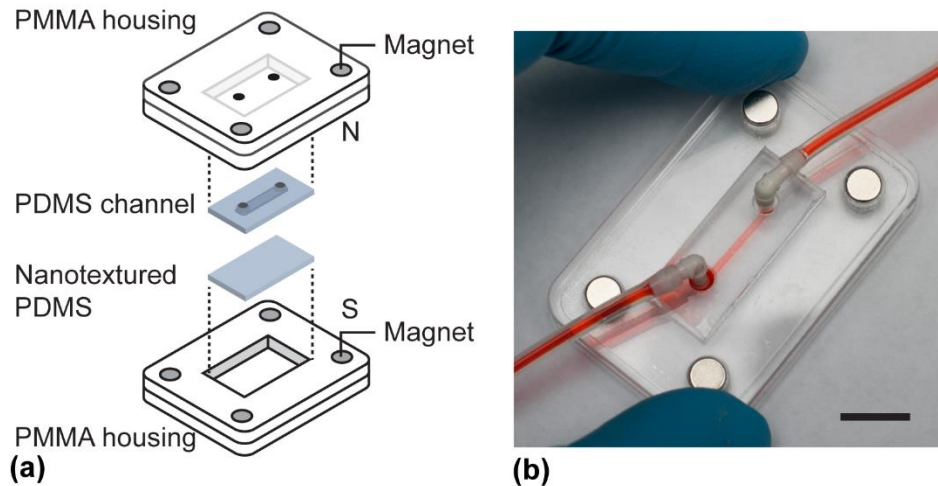


Figure 3.5 (a) Schematic showing the microfluidic integration of nanotextured PDMS using the SEAM platform that consists of PMMA housings with embedded magnets, nanotextured PDMS surface, and PDMS channel. Magnets are installed in top and bottom housings with opposite polarity facing each other for self-aligned assembly. (b) Image of an assembled device. Channel access ports are connected to syringe pump through microfluidic tubing and barb fittings. Red dye was loaded into the channel for visualization. (Scale bar = 10 mm).

### 3.3.5. Nanotexture for Enhanced Cell Adhesion

It was expected that the increased surface area on nanotextured PDMS would lead to enhanced cell-surface interactions resulting in stronger cell attachment compared to plain (non-textured) PDMS. To test this, PDMS surfaces were functionalized with an anti-EGFR antibody within the reversibly sealed SEAM platform. SEAM allowed easy integration of nanotextured PDMS and enabled controlled application of fluid shear stress. EGFR is upregulated in several cancer types and is a common target for cancer cell capture. A human non-small lung cancer cell line, A549, was used to investigate possible enhancements in cell attachment strength. These cells were chosen because they have

relatively low expression levels of EGFR compared to other cancer cell populations such as A431 and human glioblastoma [121-123]. Cells with overexpressed EGRF are likely to have more pronounced interactions with antibody-functionalized surfaces while cells with moderate expression could highlight the influence of functionalized nanotextured surfaces on cell attachment.

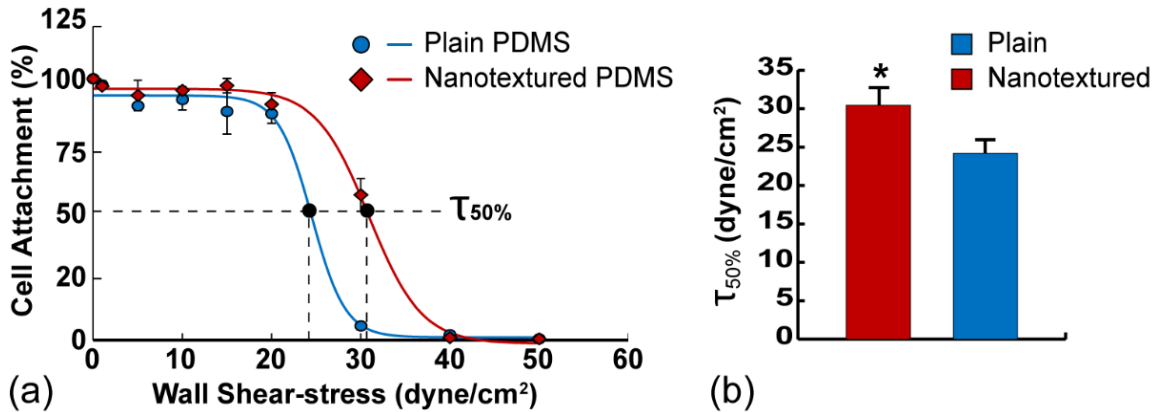


Figure 3.6. a) Cell attachment as a function of wall shear stress. The dashed line represents the 50% cell detachment threshold. The experimental data were fitted with a 4-parameter sigmoidal fit (coefficient of determination,  $R^2 > 0.99$  for both data series). The reduced chi-square values for the fitted curves were 2.3 and 2.0 for plain and nanotextured PDMS, respectively. b) The average shear stress required to detach 50% cells captured on functionalized plain PDMS ( $24 \pm 0.4$  dyne/cm<sup>2</sup>) and nanotextured ( $30 \pm 0.7$  dyne/cm<sup>2</sup>) PDMS; (\**p-value* < 0.05, *n* = 4).

A549 cells (average density of 200 cells/mm<sup>2</sup>) were allowed to attach onto anti-EGFR antibody functionalized PDMS surfaces and exposed to different shear stresses ranging from 0 – 50 dyne/cm<sup>2</sup> using SEAM. The number of cells remaining in the channel after exposure to shear stress was fit to a 4-parameter sigmoidal curve (Figure 2.6a). The average shear stress required to detach 50% of cells from the two surfaces,  $\tau_{50\%}$ , was compared (Figure 3.6b). Results showed that 26 ± 5% higher  $\tau_{50\%}$  was required to detach A549 cells from functionalized nanotextured PDMS versus plain PDMS. These results can

be attributed to the larger capture area and higher density of antibodies on the surface. Assuming a hexagonal close-packed neutravidin layer [124] the neutravidin surface density on plain and nanotextured PDMS was estimated to be  $1.36 \times 10^9$  and  $2.5 \times 10^9$  per  $\text{mm}^2$ , respectively. A biotin-fluorophore conjugate was used to verify the increased presence of neutravidin on the nanotextured surfaces (Figure 3.7).

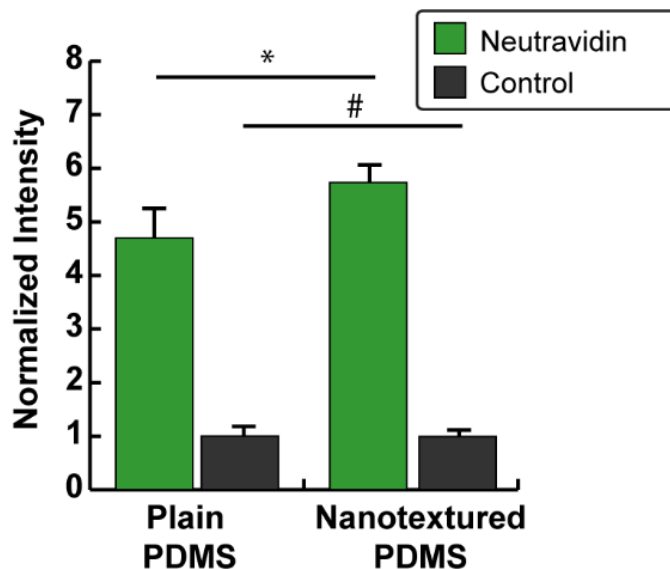


Figure 3.7. Fluorescence intensity of biotin-atto-488 conjugated on neutravidin and control functionalized PDMS surfaces. All the values are normalized with respect to average fluorescence intensity on plain PDMS. The average fluorescence intensity on neutravidin functionalized plain and nanotextured PDMS surfaces were  $4.67 \pm 0.32$  and  $5.7 \pm 0.24$ , respectively; Fluorescence intensity on plain and nanotextured control PDMS surfaces were  $1 \pm 0.14$  and  $1 \pm 0.09$  (\**p-value* < 0.05, #*p-value* = 0.96, *n* = 3). The presence of nanotexture increased the surface area and helped to accommodate a higher number of neutravidin molecules on the surface.

### 3.3.6. Nanotexture for Enhanced Cell Capture

Based on the cell adhesion results demonstrating increased cell-surface interactions, it was expected that the nanotextured PDMS surfaces would exhibit enhanced selective cancer cell capture compared with plain PDMS. To test this

hypothesis, A549 cells were 1) incubated on PDMS surfaces for 20 minutes followed by 2) a wash at a flow rate ( $Q$ ) of 100  $\mu\text{L}/\text{min}$  and 3) captured cells were imaged with a fluorescence microscope. An illustration of the cell capture experiment is shown in Figure 3.8(a). Figure 3.8(b) shows representative images of cells captured on functionalized nanotextured and plain surfaces. Images of fluorescently labeled cells were superimposed on optical images of the underlying surface to highlight texture. Figure 3.8(c) summarizes the cell capture results.

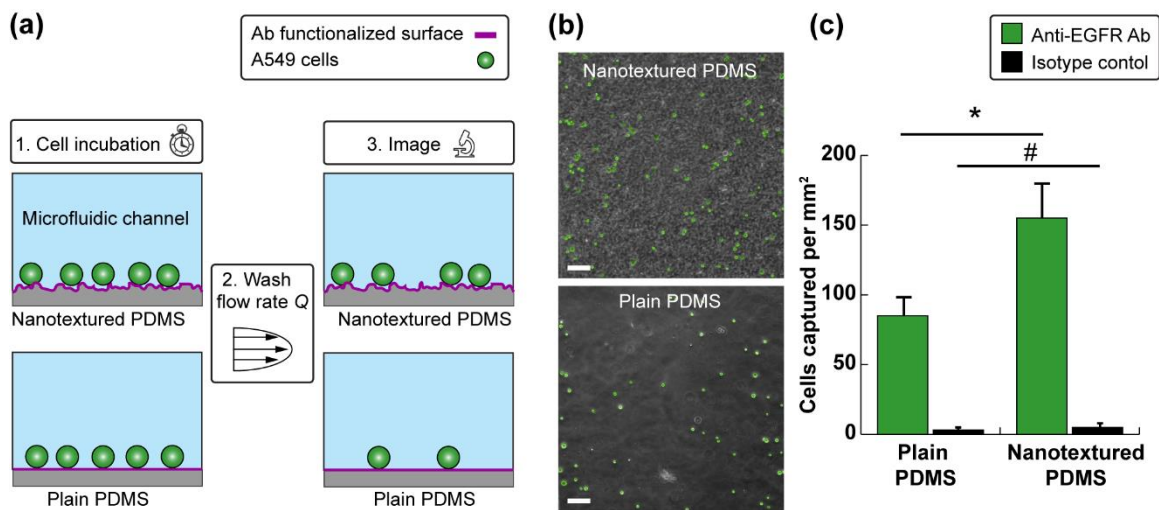


Figure 3.8. (a) Schematic showing cell capture process. Surfaces are incubated with A549 cells and washed using a syringe pump. (b) Representative fluorescent images of captured A549 cells on nanotextured (top) and plain PDMS (bottom); scale bar is 100  $\mu\text{m}$ . Fluorescent images of A549 superimposed on bright-field micrographs of the respective surfaces for visualization. (c) The density of captured A549 cells on anti-EGFR and isotype control functionalized plain and nanotextured PDMS. The A549 cell densities (average number of cells/ $\text{mm}^2$ ) on anti-EGFR antibody functionalized plain and nanotextured surfaces were  $85 \pm 14$  and  $148 \pm 37$  cells/ $\text{mm}^2$ , respectively; cell densities on isotype control plain and nanotextured PDMS surfaces were  $4 \pm 2$  and  $7 \pm 3$  cells/ $\text{mm}^2$ ; ( $*p\text{-value} < 0.05$ ,  $\#p\text{-value} = 0.15$ ).

From these experiments, a  $71 \pm 19\%$  increase in cell capture was observed on the nanotextured PDMS compared to the plain PDMS with statistically significant differences

( $p$ -value < 0.05,  $n = 4$ ). To confirm that these observations were due to increased contact between cells and antibody functionalized surfaces and not from physical trapping of cells on nanotextured surfaces ( $R_q \sim 680$  nm), PDMS substrates were functionalized with (non-targeting) antibodies isotype-matched to anti-EGFR antibodies. If physical trapping played a significant role in the cell capture, the number of cells non-specifically attached to the nanotextured surface compared to a plain PDMS surface would be higher. Capture experiments with non-targeting isotype-matched antibodies showed no statistical differences ( $p$ -value = 0.15) between plain and nanotextured surfaces. Thus, it is concluded that the increased capture could be attributed to the specific interactions between the antibody functionalized nanotextured PDMS and the EGFR on the cell surface.

A neutravidin-biotin functionalization scheme was used here because it is a versatile and commonly used approach to immobilize antibodies to a surface that can be easily replicated. The small amount of non-specific cell attachment could be related to electrostatic interactions between the neutravidin surface and the cellular membranes and these effects could be further reduced by (i) incorporating hydrophilic polyethylene glycol (PEG) chains as linkers between the antibody and the biotin molecule and/or by (ii) introducing PEG-biotin molecules in the channel after antibodies are attached to block unoccupied biotin binding sites.

### **3.3.7. Selective Capture of Cancer Cells on Nanotextured Surfaces from a Multi-Cell Mixture**

In clinical samples, cancer cells are captured from blood samples that include red blood cells (RBC), white blood cells (WBC), epithelial, and endothelial cells. The ability to selectively capture cancer cells from a background cell population was explored by creating a ~1:1 (47%-53%) mixture of A549 and human umbilical vein endothelial cells

(HUVEC), respectively. The cell mixture was introduced onto the functionalized nanotextured surface within SEAM platform (initial seeding density = 150 cells/mm<sup>2</sup>). HUVECs were chosen because they have very low expression of EGFR on the cell membrane[125]. PDMS surfaces were functionalized with an isotype-matched biotinylated antibody as a control, and A549 cells (green) and HUVECs (orange) were fluorescently labeled to simplify cell identification and enumeration. A schematic illustration of the experiment is shown in Figure 3.9(a) and a representative multi-color fluorescence image of the cell mixture on the surface before and after washing is shown in Figure 3.9(b).

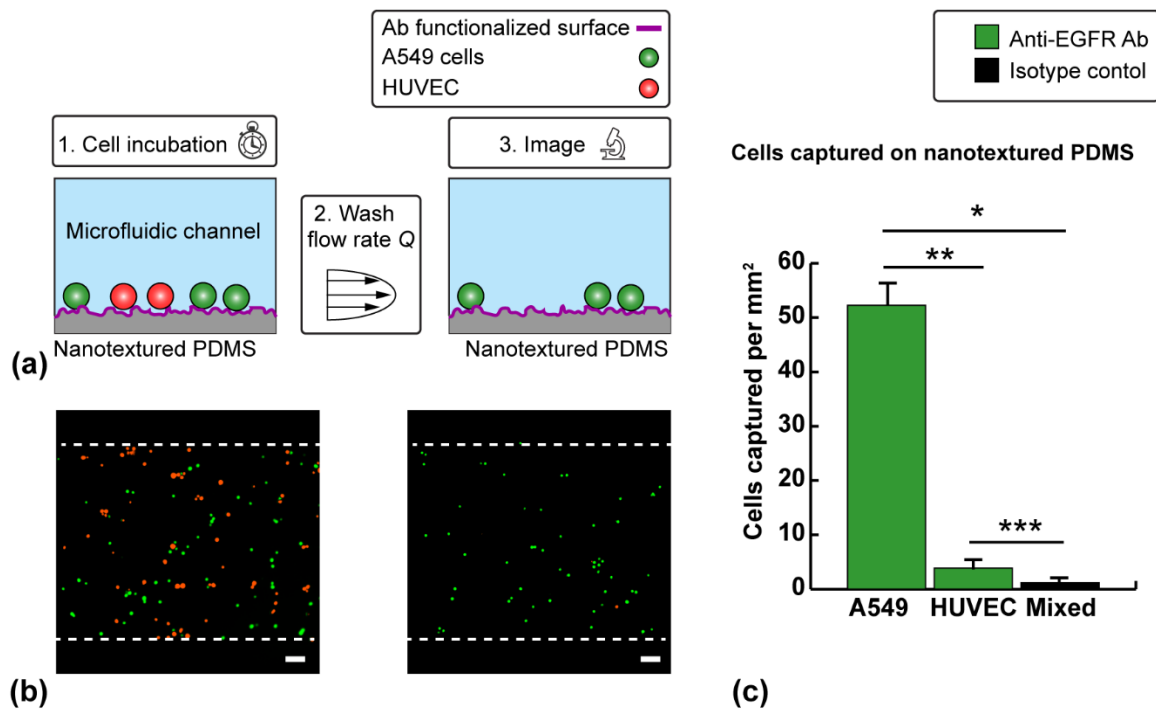


Figure 3.9. (a) Schematic of specificity experiments. Nanotextured surfaces are incubated with a mixture of A549:HUVEC at 1:1 ratio and washed using a syringe pump. (b) Representative fluorescent images of the cell mixture before (left) and after wash (right); green cells are A549 cells and red are HUVECs; scale bar = 100 μm for both images. (c) Graphical representation of average cell densities of A549 cells and HUVECs on anti-EGFR and the control surfaces after the washing step. Average A549 and HUVEC cell densities on anti-EGFR modified surfaces were 52 ± 4.1 and 4.0 ± 0.7 cells/mm<sup>2</sup>,

respectively. The average number of cells captured on isotype modified surfaces were  $1 \pm 0.2$  cells/mm<sup>2</sup>. (\**p-value* = 0.0001, \*\**p-value* = 0.005, \*\*\**p-value* = 0.0001; *n* = 3).

Results showed that the fraction of A549 cells on the nanotextured surface increased from 47% at initial introduction to 93% after the attachment and wash steps as shown in Figure 3.9(b). Capture data are summarized in Figure 3.9(c). Average cell densities of A549 cells and HUVECs were  $52 \pm 4.1$  cells/mm<sup>2</sup> and  $4 \pm 0.7$  cells/mm<sup>2</sup>, respectively. ANOVA showed statistically significant differences in cell capture between the two types of cells. After washing, 74% of cancer cells and 5% of HUVECs remained bound to the anti-EGFR functionalized surface. HUVECs may have been bound to the surfaces due to (i) interactions between the low expression of cell-membrane EGFR and high-density of anti-EGFR antibody on the nanotextured surface [122, 126], or (ii) interactions between the captured cancer cells and E-selectin and P-selectin on the HUVECs [127-129]. It is also observed that  $1 \pm 0.2$  cells/mm<sup>2</sup> were attached to the isotype control surface. This non-specific attachment could be due to electrostatic interactions with the surfaces. In addition to increased cell attachment (Figure 3.8c), nanotextured PDMS was able to enrich cancer cells from a mixed cell solution using nanotextured PDMS in the SEAM platform.

### **3.3.8. Simplified Workflow for Nucleic Acid Isolation from Captured Cells**

An important capability in cell capture devices is easy access to cells and nucleic acids for downstream analysis (e.g. clonal expansion, fluorescence in situ hybridization (FISH), gene expression, and sequencing) to determine the type of primary tumor and monitor disease progression [130, 131]. Microfluidic cell capture approaches are typically formed by permanently bonding the channel network to the capture surface, and access to the captured cells and nucleic acids is only possible by flowing fluid through the channel. With the magnetic latching used in SEAM, the channel and the surface can be quickly

decoupled to provide open access to the captured cells. For nucleic acid isolation, the flexible PDMS surface (and captured cells) can be removed from the device and transferred directly to a commercially available nucleic acid isolation workflow. Direct transfer can limit sample losses since the entire cell population is transferred without requiring flow-based sample handling or collection. As shown in Figure 3.10, nucleic acid was extracted from captured cells and the isolation yield was compared from flow-based in-channel lysis to our direct transfer method. Cells were captured in individual devices and half were selected at random for in-channel lysis of cells while the remaining devices were used for direct transfer of nanotextured surfaces to the lysis buffer. For in-channel lysis, a syringe pump was used to flow lysis buffer through the channel and collected in a tube. In the direct transfer method, the flexible PDMS surfaces were removed from the device and transferred directly into an equivalent volume of lysis buffer in a collection tube. The lysate was then processed using a Zymo extraction kit according to the manufacturer's instructions. The nucleic acid yield and purity were measured with a Nanodrop spectrometer.



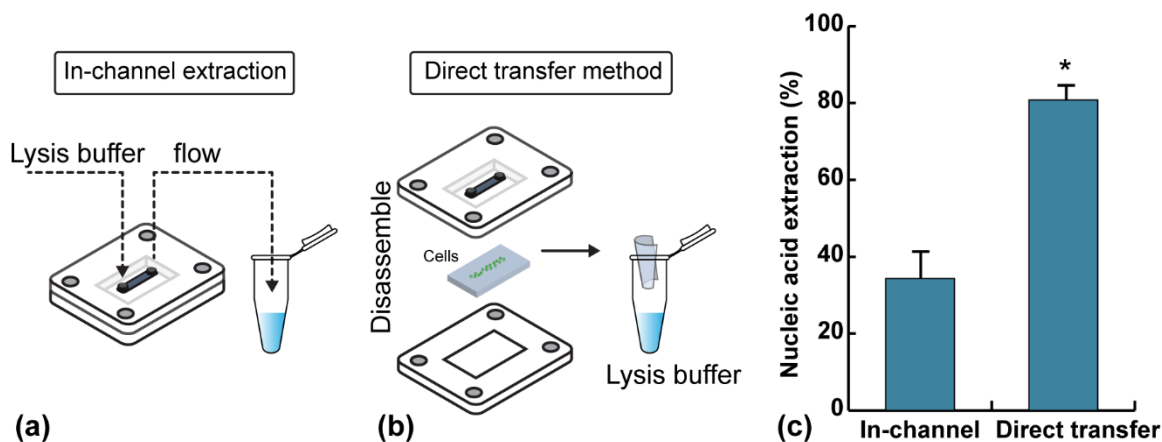


Figure 3.10. (a) Nucleic acid extraction from captured cells using in-channel lysis. The dotted line represents flow path for the lysis buffer and sample collection. (b) Cell lysis with direct transfer of captured cells from nanotextured PDMS surface into lysis buffer. (c) Comparison of nucleic acid extraction efficiency using the two methods. The data is normalized to the amount of nucleic acid directly extracted from a cell suspension. (\* $p$ -value < 0.05;  $n = 5$ ).

Results showed that approximately twice as much nucleic acid was extracted from the direct transfer method ( $1523 \pm 225.9$  ng,  $A_{260/280} = 2.03 \pm 0.02$ ) compared to in-channel lysis ( $647 \pm 5.7$  ng,  $A_{260/280} = 1.99 \pm 0.08$ ) with statistically significant differences ( $n = 5$ ,  $p$ -value < 0.05). For the normalization of data in Figure 3.10(c) the number of cells equivalent to the initial cell seeding density was pipetted directly from cell suspension into lysis buffer. The data are presented as the extraction efficiency with respect to the control. The extraction efficiency of direct transfer and in-channel method was 80% and 35%, respectively. The purity of the extracted nucleic acid between the methods was comparable, but the direct transfer method was simple to implement and did not require sample handling or fluid manipulation. The straight channel used here represented a conservative extraction because more complicated branched networks can lead to sample losses from dead volumes, external tubing, and large surface area-to-volume ratios microfluidic channels. The open cell access enabled by SEAM simplified the experimental

workflow for cell processing required for downstream analysis. Taken as a whole, our simplified nanotexture fabrication technique and microfluidic integration approach aim to eliminate the entry barrier for researchers interested in exploring the interactions between nanotextured surfaces and target cells.

### **3.4. Discussion**

The goal of this work was to present solutions to enable researchers to fabricate nanotextured substrates and easily integrate them into microfluidic systems to support applications where cell-surface interactions play an important role. Using a simple fabrication scheme can be carried out in any laboratory, our capture capabilities were comparable with other techniques that required specialized equipment and complex fabrication processes (71% increase vs. 85-100% increase) [57, 66, 70, 99]. It was anticipated that optimized surface functionalization approaches will improve our capture capabilities. The replica molding-based fabrication of nanotextured surfaces enables rapid iteration of surface modification approaches to improve capture. Conventional nanofabrication tools are compatible with a variety of hard materials (e.g. metal, glass, polymers), but soft biological materials pose a processing challenge; the backside molding approach used here can be applied to create defined nanotexture on polymers, synthetic hydrogels, and biological gels. A common neutravidin-biotin functionalization scheme was utilized to immobilize antibodies to the capture surfaces. This approach can be advanced to target a wide range of cancer cells through the simple addition of multiple biotinylated antibodies. This method is also amenable to other reagents such as RNA and DNA aptamers, or ECM proteins. The versatility of the approach opens the door for studies exploring the combined effects of nanotopography, substrate stiffness, and cell-protein interactions to control stem cell differentiation, cell adhesion, and migration. The molding technique is also a highly scalable and cost-effective approach to quickly create

nanotextured surfaces at the benchtop to support proof of concept studies and is compatible with a variety of other mold fabrication techniques including 3D printing.

The SEAM platform is designed to simplify integration of microfluidics and nanotextured substrates. Although our proof of concept uses a single microfluidic channel and a static cell incubation, throughput can be increased with a branched fluidic channel network and chaotic advection features can be introduced to the channel-roof to improve cell-surface contact during flow-based sample introduction. The removable assembly provides easy access to captured cell populations for processing and downstream analysis. SEAM enables the transfer of the entire captured cell population with minimal sample handling and fluidic manipulation; direct access to captured cell population provides a convenient approach for clinicians and life-science researchers to perform a variety of post-capture analysis without requiring potentially problematic liquid handling.

### **3.5. Conclusion**

This work presented (i) a simple molding process to create nanotextured substrates and (ii) introduce an easy-to-use platform to integrate nanotextured substrates into microfluidic architecture and (iii) demonstrated applicability in studies involving cell-surface interactions. An improvement in cell capture on antibody functionalized nanotextured PDMS was observed compared to non-textured PDMS surfaces. The nanotextured surfaces were also used to capture cancer cells from a mixed population. The modular assembly provided open access to captured cancer cell population for downstream analysis; nucleic acid extraction from the captured cancer cells using our approach showed higher isolation efficiency compared to conventional in-channel flow-based extraction method. The accessible nature of this research platform provides myriad opportunities to explore the effects of nanotexture on cell adhesion, cell capture, and other cell-surface phenomena.

## Chapter 4

### 4. Classification of Cancer Cells using Computational Analysis of Dynamic Morphology

#### 4.1. Introduction

Over the past few years, numerous efforts have been made to detect tumor cells for early cancer diagnosis. Early detection and treatment of cancer has very high survival rates and dramatically improved quality of life. The detection of cancer cells is challenging due to their rare presence in blood samples at early stages. In a similar vein, the identification of metastatic and aggressive cells is very important for cancer staging. Several methods have been employed to capture and identify tumor cells based on their physical, mechanical and chemical properties (e.g., size, deformability, electrical polarizability) [132]. For example, tumor cells have been recognized based on their biophysical properties using microfiltration, atomic force microscopy, micropipette aspiration, and micropore devices [31, 34, 116, 133-135]. The distinct electrical charge of tumor cells have also been utilized for electrophoresis based separation [136]. In the past decade, ligand-based tumor cell capture platforms have been widely used for highly sensitive and selective applications [53, 54, 69, 113, 137]. Such affinity-based methods have also been explored to selectively tag magnetic and fluorescent particles for cancer screening [138-140]. Although these techniques have their own advantages, these methods often require complex and time-consuming post-capture analysis for further verification. There is a huge disparity in knowledge for rapid, low-cost, and highly sensitive platforms for cancer screening.

Various cell screening methods have been demonstrated to analyze static images of cells, and a significant amount of work is reported on automated high-throughput microscopy for its rapid image acquisition capability [141-143]. Several fluorescently tagged biopsy samples have been imaged and analyzed to classify multiple cell phenotype

and morphology [82, 144, 145]. Nevertheless, static image-based classification techniques are limited to analyze cell composition only and cannot capture the behavior of cells. Therefore, time-resolved live-cell imaging is the way to go to analyze complex cellular dynamic processes. It has already been shown that the morphology of cancer cell lines correlates to their gene expression profile [146]. Fluorescence time-lapse imaging has been used to investigate complex dynamic processes such as cell division, cell motility, and intracellular trafficking [147-149]. It has been reported that tumor cells show distinctive morphology on a biofunctionalized surface [114, 150-152]. However, visual inspection of morphological dynamics from large-scale data is very time-consuming, labor-intensive, and unreliable. Even a well-trained pathologist would require to spend a great deal of time to process and analyze the data from simple biological assay. The overwhelming size of data motivates the design of machine learning approaches for the classification of cell phenotype, gene sequence, protein expressions, and other physical properties [153-157]. The ability to process and learn from a large number of time-resolved images and a comprehensive analysis of cell gesture can make a unique contribution to effective detection and classification of cancer cells.

This work describes a predictive computational framework to interpret complex cellular dynamics from microscopic time-lapse images for cancer diagnosis. About 50 characteristics features were extracted to quantify the intricate gesture of cells. A supervised machine learning algorithm was implemented to develop a classification model that identified metastatic tumor cells derived from solid-biopsy of cancer patient. The healthy counterparts of tumor cells, astrocytes, were also incubated on an aptamer-functionalized glass surface. The temporal context was incorporated into the annotation scheme to define the gestures of cells. Incorporation of cell behavior also suppressed confusion due to cell-outlook. Cell gestures were quantified in terms of features such as

cell geometry, cellular protrusions, and morphological changes in cellular boundary over time. The feature vectors were combined in a dataset to train and validate a predictive model. The approach was demonstrated to selectively detect metastatic human glioblastoma (hGBM) cells and astrocytes with an average accuracy of 85%. The approach is equally appreciable for large-scale applications for the detection of tumor cells without fluorescently labeling the cells. This is a novel system to detect cancer cells from cell gestures and can be readily used by pathologists and life science researchers to study cell behavior for disease diagnosis.

## **4.2. Materials, Methods, and Experimental Setup**

### **4.2.1. System Overview**

A high-level overview of the system is shown in Figure 4.1. The cell preparation and sample collection section include a functionalized surface and an optical microscope to record time-lapse images of cells. Cells were introduced on an anti-EGFR modified surface and the morphological behavior of cells was analyzed from their time-lapse optical micrographs. The classification of cancerous and non-cancerous cells was done based on this dynamic cell morphology. The classification system is composed of two major stages: (i) training and (ii) prediction. The image segmentation component crops out individual cell images from every frame of the time-lapse optical micrographs. The feature extraction part computes shape-dependent feature vectors. Machine learning algorithm was used to build the classifier based on the known sample. Once trained, the classifier identifies the unknown cell samples based on their distinguishing features.

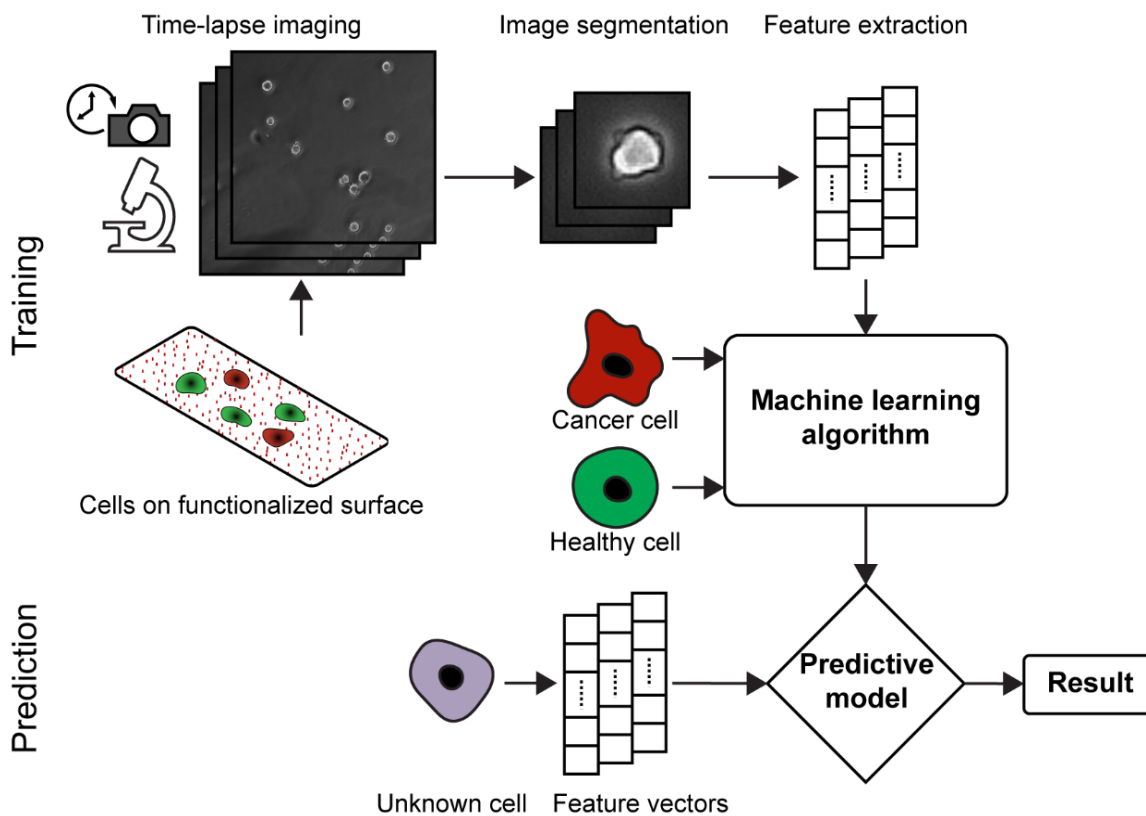


Figure 4.1. Schematic of dynamic morphological analysis of cell gesture. Optical micrographs of the cell population are processed with image analysis tool to detect the cell-contour. A collection of feature vectors is extracted to generate a morphological profile. The data for cell gesture is stored in a dataset. Machine learning algorithm is used to generate decision-making system to classify the cells based on the training data. Once the classification model is developed, unknown cells are classified based on the resemblance of their feature vectors to the known dataset.

#### 4.2.2. Surface Functionalization

Glass slides were functionalized with the anti-EGFR aptamer molecules. All chemicals were obtained from Sigma-Aldrich unless otherwise noted. Details of the functionalization process have been described before [114, 150]. To summarize, clean glass slides were functionalized with a silane reagent (3-Aminopropyl-triethoxysilane, SigmaAldrich-440140), crosslinker (p-Phenylene diisothiocyanate, SigmaAldrich-258555), DNA capture molecule and RNA aptamer (anti-EGFR) sequentially to immobilize

aptamers on the surface. The DNA linker with customized sequence was obtained from Integrated DNA Technologies (IDT) and the anti-EGFR aptamer was designed through SELEX process in the Ellington laboratory at the University of Texas at Austin. The anti-EGFR aptamer sequence was: 5'-GGC GCU CCG ACC UUA GUC UCU GUG CCG CUA UAA UGC ACG GAU UUA AUC GCC GUA GAA AAG CAU GUC AAA GCC GGA ACC GUG UAG CAC AGC AGA *GAA UUA AAU GCC CGC CAU GAC CAG*-3' (the extended sequence is shown in italics and it was used to bind to capture DNA). Aptamers are synthetically selected DNA or RNA oligonucleotides that bind to target molecules and are used for cancer diagnosis and therapeutics [158-160]. The sequence of the DNA capture molecules was 5'-amine-CTG GTC ATG GCG GGC ATT TAA TTC-3'. A mutant aptamer of the same length with a scrambled sequence was used for the control experiments. The sequence for mutant aptamer was 5'-GGC GCU CCG ACC UUA GUC UCU GUU CCC ACA UCA UGC ACA AGG ACA AUU CUG UGC AUC CAA GGA GGA GUU CUC GGA ACC GUG UAG CAC AGC AGA *GAA UUA AAU GCC CGC CAU GAC CAG*-3'. The presence of the aptamer on the glass surface was characterized with fluorescence imaging (with acridine orange). A schematic of the surface functionalization process is shown in Figure 4.2.

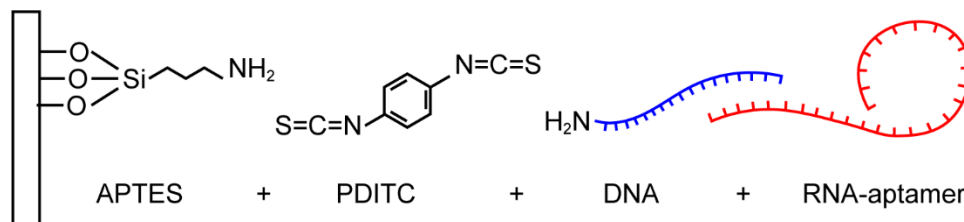


Figure 4.2. Schematic representing anti-EGFR aptamer functionalization on glass substrate.

It has been reported previously that most of the cancer cells overexpress EGFR on cell membrane [23, 161]. The EGFR density on lung and brain tumor cells is in the



range from 40,000 to 100,000 per cell. In a separate study, it has also been shown that EGFR is responsible for the proliferative nature of cancer cells [162]. It is the constant activation of these EGFR that causes the cells to go through morphological changes.

#### **4.2.3. Cancer and Healthy Cell Preparation**

Human glioblastoma (hGBM) cells and astrocytes were used for cell-gesture comparison. The hGBM cells were obtained from consenting patients at the University of Texas Southwestern Medical Center at Dallas, Texas as per the approved Institutional Review Board (IRB) protocol work [150]. Glioblastomas are brain tumor cells with overexpression of EGFR. The surface was functionalized with anti-EGFR aptamer because hGBM cells overexpress EGFR [114]. The astrocytes are healthy counterparts from the same lineage as hGBM cells. hGBM specimens (~50 mm<sup>3</sup>) were collected from patient's tumor (hGBM mass) and kept in ice-cold HBSS medium immediately after removal from the brain. The red blood cells were removed by lymphocyte-M (Cedarlane labs). The hGBM tissue was gently dissociated with a solution of papain (2%) and dispase (2%). It has been reported that GBM cells can be identified by a cell surface glycoprotein, CD133 [163-165]. The triturated solution was then tagged with CD133/2 (Miltenybiotec-293C3)-PE antibodies and sorted with Fluorescence-Activated Cell Sorting (FACS) Calibur machine (BD Biosciences). Cells were suspended in serum-free DMEM/F-12 medium (20 ng/mL of mouse EGF, 20 ng/mL of fibroblast growth factor, 1× B27 supplement, 1× Insulin-Transferrin-Selenium-X, and 100 units/mL penicillin - 100 µg/mL streptomycin) at 3 x 10<sup>6</sup> cells/60-mm plate density. Only CD133-positive cells were used in the experiments (referred as hGBM). The Astrocytes used for control experiments were also derived from human patients. After extraction and culture, the astrocytes were isolated from microglia and oligodendrocytes and were grown in culture medium.

#### 4.2.4. Effect of Aptamer on Morphology of Cancer Cells

Tumor cells overexpress EGFR on the cell membrane. These EGFR interacts with the anti-EGFR aptamer and results in a change in cell shape on a functionalized surface. The constant interactions of EGFR and anti-EGFR aptamers are responsible for the change in cell morphology. This phenomenon is not observed in healthy cells because healthy cells do not have enough EGFR on the cell membrane to interact with the functionalized surface. Figure 4.3 illustrates the change in tumor cell morphology due to the presence of aptamer on glass substrates

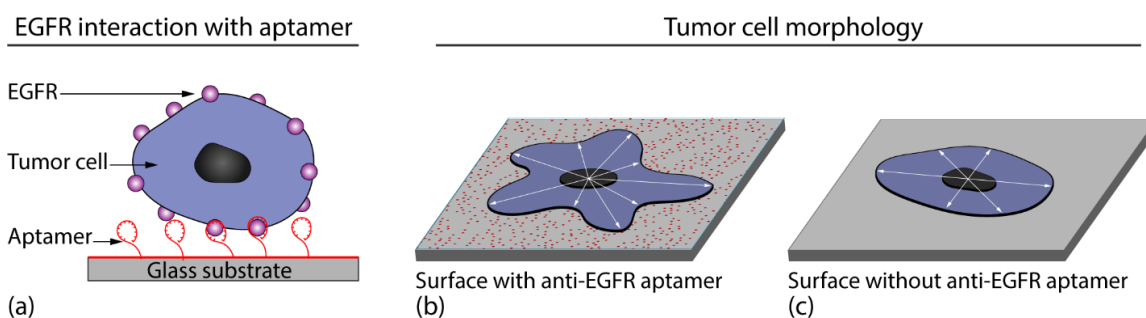


Figure 4.3. Effect of aptamer on the morphology of cancer cells. (a) EGFR expressed tumor cells interacts with anti-EGFR aptamer functionalized glass surface. (b) Tumor cells show distinct morphology over time when seeded on anti-EGFR aptamer functionalized surface. (c) Tumor cells do not show much activity in absence of aptamer on the surface.

#### 4.2.5. Image Acquisition and Processing

Cells were suspended on the glass substrates at a density of 100,000 cells/mL and were allowed to interact with the functionalized substrates. Time-lapse optical micrographs were acquired at an interval of 30 seconds for 15 minutes using a Leica optical inverted microscope (Leica DM IL LED) with DFC295 CMOS color camera at 20X magnification. A mercury light source (Leica classic) was used to illuminate the samples from the bottom side. All transmitted-light images were acquired in the Differential Interference Contrast (DIC) mode with 20 ms exposure time. A larger interval may fail to

capture the morphological changes of cell. Alternatively, a smaller interval is preferable to monitor the cell activity more precisely but at the cost of increased data size. The entire substrate was imaged with a moving stage microscope. The micrographs were acquired and stored at 4096x3072 resolutions in TIFF format. After contrast enhancement and Wiener filtering on the acquired images, each cell image was separated in a 200 × 200 pixel (60 μm x 60 μm) cropping window using image segmentation algorithm [114]. With 15 seconds interval, a set of 25 images was allocated for each cell depicting states of that particular cell to represent the dynamic morphology over time. A representative time-lapse images of a cancer and healthy cell is shown in Figure 4.4. These images were processed and analyzed to quantify the cell gestures with a set of feature vectors. The features were used to construct a dataset to train and validate the system. All the algorithms were implemented in MATLAB (v2013a) and Python (v3.5) software. Python package scikit-learn (v0.18) was used for the machine learning.

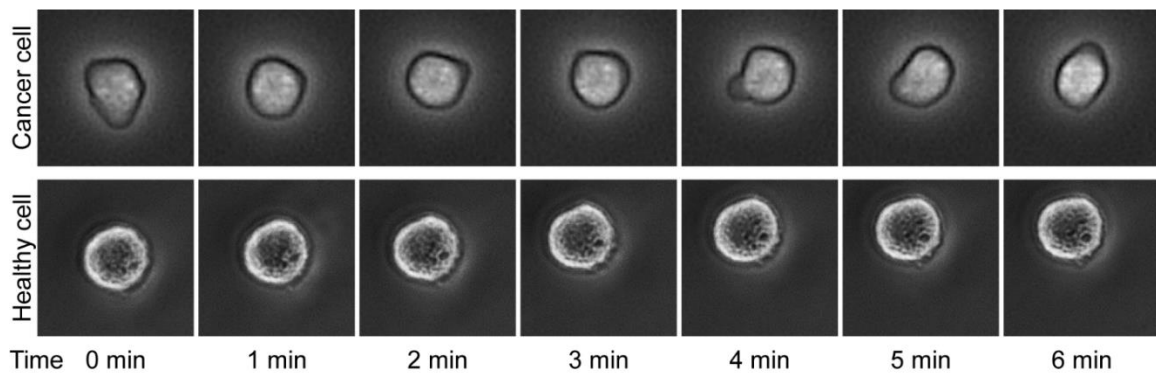


Figure 4.4. Representative time-lapse images of a cancer cell and a healthy cell on anti-EGFR functionalized surface taken with an optical microscope. The changes in cell morphology over time are more pronounced for cancer cell.

#### **4.2.6. Feature Extraction and Annotation of Cell Gesture**

A level-set algorithm was applied to detect the contour of the cell from each image [166]. Multiple feature vectors, such as the center of mass, area, perimeter, and

equivalent-radius of the cell were extracted from the cell's contour. Other shape-defining parameters such as aspect ratio, convexity, bounding rectangle, minimum enclosing circle, best-fitted ellipse, extent, and solidity of the shape were also calculated to characterize cell gestures at various instances of time. Figure 4.5 demonstrates a few shape defining features extracted from cell contour.

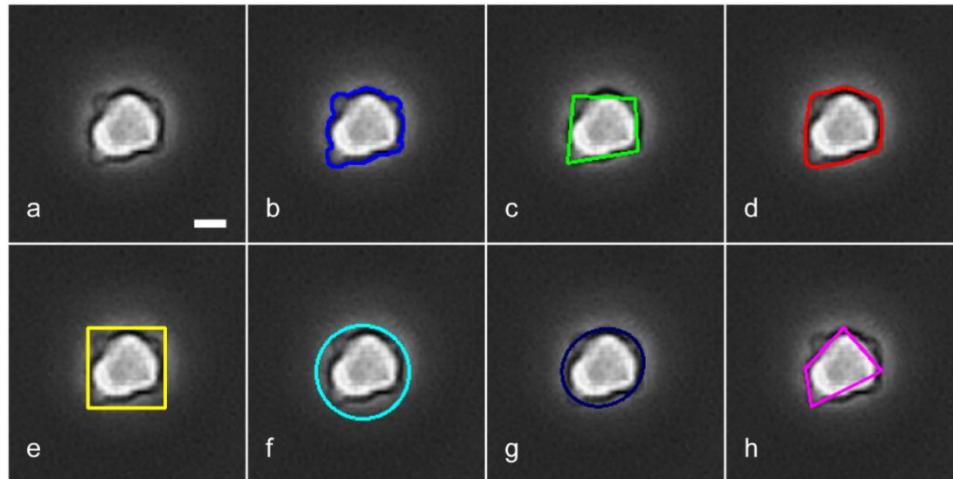


Figure 4.5. Features extracted from grayscale optical micrographs of a cell. (a) Grayscale image of the cell. The scale bar = 10  $\mu\text{m}$ . (b) The contour of the cell. (c) 4-point shape estimation. (d) Convexity from cell contour. (e) Bounding rectangle. (f) Minimum enclosing circle. (g) Best fitted ellipse. (h) Extreme points.

Cancer is a disease of abnormal cell growth and unusual cellular activity. Tumor cells can have larger size, greater nucleus-to-cytoplasm ratio, and very different cytoskeletal structures in contrast to normal cells. In addition to that, cells showed distinct dynamic morphology. To quantify the changes in cell shape over time, the rate of change of the shape-parameters was also taken as another set of feature vectors. The Hausdorff distance between consecutive frames, uniformity of cell contour, and the number of pseudopods around cell boundary were calculated to define the dynamic behavior of the cells. The rate of change of these parameters was also calculated and defined as additional feature vectors. Tracking the activity of the cell over the whole incubation period

revealed unique but subtle nature of cancer cells. Using machine learning algorithms, these features were quantitatively and computationally analyzed to recognize the differences in cell behavior.

#### **4.2.7. Feature Extraction**

After acquiring all the time-lapse micrographs, each cell image was cropped out in a 200x200 pixel window. A MATLAB program was used to store all the cropped images for each cell and every frame in an indexed directory. A batch of images was generated for each cell showing its shape change with time. These images were in RGB format. Then a level-set algorithm was used to detect the cell contour based on the image contrast. The RGB images were processed with a low-pass Wiener filter to remove noise while preserving the edges by adapting to a pixel-wise statistical estimation of the local neighborhood. The images were further smoothed by a Gaussian filter. Then the RGB images were converted to greyscale images. A properly exposed cell image (greyscale) should have the maximum contrast along its contour. The level-set method is a dynamic process which starts from the image boundary and moves inwards the cellular edge to track the cell contour. In this way, the cells were segmented from the non-cell background by detecting the cell boundary. The greyscale images of the cells were then converted to binary images. A binary image contains solid black (pixel value=0) and white (pixel value=255) pixels only. Thus every cell image is represented as an orthogonal matrix with the pixel intensity corresponding to its location (coordinates). The cell contour is the vector containing all the coordinates of the cell boundary. Multiple features were calculated from this binary cell images including the area of the cell, the perimeter (length of the contour), roundness, aspect ratio, solidity, and the equivalent radius.

#### 4.2.8. Definition of Features

Pseudopods are defined as the protruding section from a regular cell boundary. If the protrusion was larger than 120% of the average distance from the center to cell-contour; and the width of the protrusion has an angular distance of  $>10^\circ$  at the center of the cell, then the protrusion was counted as one pseudopod. Cell aspect ratio is the ratio of cell width and cell height. The solidity of the cell was calculated by taking the ratio of the area of the contour and the area of the convex envelope of the cell. Cell extent is the ratio of the cell area and the bounding rectangle. Hausdorff distance was used to calculate the resemblance between cell contours (represented by  $A$ ,  $B$  in the equation) in two consecutive images. If the cells do not show any morphological change within two consecutive frames, the Hausdorff distance will be a small number. If a cell is changing shape, the distance will be a larger number.

$$\text{Aspect ratio} = \text{cell width} / \text{cell height}$$

$$\text{Solidity} = \text{area of cell contour} / \text{area of cell convex envelope}$$

$$\text{Cell extent} = \text{area of cell contour} / \text{area of cell bounding box}$$

$$\text{Hausdorff distance, } H(A, B) = \max\left(\left(h(A, B), h(B, A)\right)\right); \text{ where, } h(A, B) = \max_{a \in A} \min_{b \in B} |a - b|$$

The quantitative metrics of all the features are mentioned in Table 4.1. The resemblance of the cell shape with a rectangle, circle, or an ellipse also provided information about cell geometry. For these measures, the best fitted geometric shape was determined by the algorithm and the area or extreme points of the shapes were used for feature vector calculation. Once all the features were defined, the variation of these unique features among the different frame of the time-lapse images was calculated and used as

another set of features. The rate of change of the parameters with respect to time was also taken into account.

A dataset was created with all the feature vectors. The machine learning was implemented in using python programming (version 3.5). Python package ‘numpy’, and ‘matplotlib’ was used for data calculation, matrix manipulation, and feature extraction. Package ‘pandas’ was used for data structure and data analysis. And ‘sklearn’ package was imported to implement machine learning in python. The Flowchart of the training and prediction process is illustrated in Figure 4.1.

Table 4.1. List of feature vectors with quantitative measure.

Feature	Quantitative Feature (Average $\pm$ SD)		
	Active Cancer	Inactive Cancer	Healthy Astrocytes
Cell area	3.51E+03 $\pm$ 09E+02	2.75E+03 $\pm$ 10E+02	5.39E+03 $\pm$ 13E+02
Number of pseudopods	4.68E-01 $\pm$ 32E-02	4.00E-03 $\pm$ 01E-02	7.20E-02 $\pm$ 13E-02
Perimeter	2.31E+02 $\pm$ 35E+00	1.99E+02 $\pm$ 35E+00	2.85E+02 $\pm$ 35E+00
Aspect ratio	9.92E-01 $\pm$ 07E-02	1.05E+00 $\pm$ 04E-02	1.01E+00 $\pm$ 07E-02
Bounding rectangle	6.85E+01 $\pm$ 10E+00	5.83E+01 $\pm$ 12E+00	8.50E+01 $\pm$ 12E+00
Center shift	2.74E+00 $\pm$ 82E-02	1.24E+00 $\pm$ 18E-02	1.92E+00 $\pm$ 79E-02
Convex hull	3.58E+03 $\pm$ 10E+02	2.60E+03 $\pm$ 10E+02	5.46E+03 $\pm$ 13E+02
Equivalent radius	3.26E+01 $\pm$ 04E+00	2.69E+01 $\pm$ 06E+00	4.06E+01 $\pm$ 05E+00
Equivalent rectangle	4.47E+03 $\pm$ 12E+02	3.23E+03 $\pm$ 13E+02	6.81E+03 $\pm$ 17E+02
Cell extent	7.08E-01 $\pm$ 02E-02	6.84E-01 $\pm$ 04E-02	7.27E-01 $\pm$ 03E-02
Hausdorff distance	1.10E+01 $\pm$ 03E+00	6.30E+00 $\pm$ 02E+00	1.73E+01 $\pm$ 10E+00
Length of fitted ellipse	7.17E+01 $\pm$ 09E+00	5.76E+01 $\pm$ 12E+00	8.61E+01 $\pm$ 11E+00
Minimum enclosing circle	3.72E+01 $\pm$ 05E+00	2.92E+01 $\pm$ 06E+00	4.43E+01 $\pm$ 06E+00
Non-uniformity	2.88E+00 $\pm$ 82E-02	1.75E+00 $\pm$ 28E-02	2.28E+00 $\pm$ 71E-02
Solidity	9.57E-01 $\pm$ 02E-02	9.65E-01 $\pm$ 78E-04	9.63E-01 $\pm$ 01E-02
Cell stretch	6.95E+01 $\pm$ 09E+00	5.53E+01 $\pm$ 11E+00	8.41E+01 $\pm$ 11E+00
Width of fitted ellipse	6.14E+01 $\pm$ 09E+00	5.10E+01 $\pm$ 11E+00	7.78E+01 $\pm$ 10E+00
Variation in cell area	2.86E+02 $\pm$ 99E+00	2.86E+02 $\pm$ 03E+02	2.50E+02 $\pm$ 01E+02
Variation in number of pseudopods	5.96E-01 $\pm$ 20E-02	2.00E-02 $\pm$ 06E-02	1.49E-01 $\pm$ 24E-02
Variation in perimeter	1.26E+01 $\pm$ 04E+00	1.06E+01 $\pm$ 07E+00	8.34E+00 $\pm$ 05E+00
Variation in aspect ratio	1.10E-01 $\pm$ 02E-02	6.44E-02 $\pm$ 03E-02	4.62E-02 $\pm$ 01E-02
Variation in bounding rectangle	5.47E+00 $\pm$ 01E+00	1.05E+01 $\pm$ 09E+00	2.67E+00 $\pm$ 01E+00
Variation in cell center shift	1.35E+00 $\pm$ 27E-02	6.65E-01 $\pm$ 13E-02	9.25E-01 $\pm$ 30E-02
Variation in cell convex hull	3.11E+02 $\pm$ 01E+02	5.30E+02 $\pm$ 05E+02	2.60E+02 $\pm$ 01E+02
Variation in equivalent radius	1.31E+00 $\pm$ 36E-02	4.82E+00 $\pm$ 04E+00	9.66E-01 $\pm$ 55E-02
Variation in equivalent rectangle	4.22E+02 $\pm$ 01E+02	6.61E+02 $\pm$ 06E+02	3.53E+02 $\pm$ 02E+02
Variation in cell extent	3.36E-02 $\pm$ 77E-04	6.47E-02 $\pm$ 05E-02	1.88E-02 $\pm$ 57E-04
Variation in Hausdorff distance	4.31E+00 $\pm$ 01E+00	2.69E+00 $\pm$ 89E-02	7.12E+00 $\pm$ 05E+00
Variation in length of fitted ellipse	4.51E+00 $\pm$ 66E-02	1.05E+01 $\pm$ 09E+00	2.73E+00 $\pm$ 01E+00
Variation in minimum enclosing circle	2.53E+00 $\pm$ 37E-02	5.38E+00 $\pm$ 05E+00	1.46E+00 $\pm$ 78E-02
Variation in non-uniformity	8.75E-01 $\pm$ 18E-02	4.22E-01 $\pm$ 11E-02	4.05E-01 $\pm$ 20E-02
Variation in solidity	1.36E-02 $\pm$ 48E-04	1.25E-02 $\pm$ 60E-04	7.97E-03 $\pm$ 62E-04
Variation in cell stretch	4.80E+00 $\pm$ 01E+00	1.01E+01 $\pm$ 08E+00	3.18E+00 $\pm$ 02E+00

Variation in width of fitted ellipse	3.22E+00 ± 66E-02	9.19E+00 ± 08E+00	2.09E+00 ± 01E+00
Rate of change in cell area over time	1.88E+02 ± 74E+00	2.11E+02 ± 03E+02	2.00E+02 ± 01E+02
Rate of change in pseudopods over time	5.33E-01 ± 25E-02	8.33E-03 ± 03E-02	8.13E-02 ± 14E-02
Rate of change in cell perimeter over time	8.63E+00 ± 03E+00	6.93E+00 ± 06E+00	6.93E+00 ± 03E+00
Rate of change in aspect ratio over time	6.37E-02 ± 01E-02	5.21E-02 ± 02E-02	4.03E-02 ± 02E-02
Rate of change in bounding rectangle over time	3.47E+00 ± 78E-02	6.69E+00 ± 06E+00	2.23E+00 ± 01E+00
Rate of change in cell center shift over time	1.18E+00 ± 22E-02	6.79E-01 ± 13E-02	9.30E-01 ± 30E-02
Rate of change in cell convex hull over time	2.02E+02 ± 81E+00	3.64E+02 ± 04E+02	2.06E+02 ± 01E+02
Rate of change in equivalent radius over time	8.72E-01 ± 31E-02	3.10E+00 ± 03E+00	7.66E-01 ± 47E-02
Rate of change in equivalent rectangle over time	2.87E+02 ± 01E+02	4.68E+02 ± 05E+02	2.84E+02 ± 01E+02
Rate of change in cell extent over time	2.59E-02 ± 59E-04	4.82E-02 ± 04E-02	1.87E-02 ± 57E-04
Rate of change in Hausdorff distance over time	3.05E+00 ± 01E+00	2.13E+00 ± 91E-02	2.68E+00 ± 92E-02
Rate of change in length of fitted ellipse over time	2.98E+00 ± 77E-02	6.74E+00 ± 06E+00	2.16E+00 ± 01E+00
Rate of change in minimum enclosing circle over time	1.62E+00 ± 37E-02	3.45E+00 ± 03E+00	1.13E+00 ± 70E-02
Rate of change in non-uniformity over time	5.66E-01 ± 20E-02	3.41E-01 ± 13E-02	3.68E-01 ± 21E-02
Rate of change in cell solidity over time	1.02E-02 ± 39E-04	1.18E-02 ± 60E-04	7.13E-03 ± 40E-04
Rate of change in cell stretch over time	3.08E+00 ± 01E+00	6.55E+00 ± 06E+00	2.51E+00 ± 01E+00
Rate of change in width of fitted ellipse over time	2.39E+00 ± 78E-02	6.20E+00 ± 06E+00	1.79E+00 ± 01E+00

#### 4.2.9. Data Classification

The feature vectors calculated for each cell sample were fed to a classifier to train respective data clusters. The model was trained with the dataset to classify three cell categories (i) Active cancer, (ii) Inactive cancer, and (iii) Healthy cells. The classes 'active cancer' and 'inactive cancer' included the gestures of hGBM cells incubated on an anti-EGFR aptamer surface and a control mutant aptamer surface, respectively. The 'healthy' group contained the gestures of healthy/non-cancerous cells (astrocytes) on both anti-EGFR and mutant aptamer functionalized substrates. Supervised machine learning algorithms were used to label the cell types in the training dataset. The system was trained with 1000 sample images including 25% active tumor cells, 25% inactive tumor cells, and 50% healthy cell samples. Three commonly used classifiers were implemented, (i) Support Vector Machine (SVM), (ii) Random Forest Tree (RFT), and (iii) Naïve Bayes Classifier (NBC) to train the system. After training, the accuracy of the classifiers was validated and compared based on their performance. A five-fold validation technique was used where 80% of the dataset was used as training samples and the rest 20% was used



for test purpose. Generally, a larger proportion of training sample ensures better classification of the test samples.

#### **4.2.10. Machine Learning Algorithm**

The key purpose of this work was to systematically quantify the extents to which a machine learning based classification model identifies tumor cells from their morphological characteristics. The task of tumor cell category identification was defined as a supervised multi-class classification problem. In supervised learning, the knowledge about the problem is composed in the form  $(x, c)$ , in which  $x$  represents an input (feature vectors in this case) and  $c$  denotes its label (cancer class). The machine learning algorithm extracts the knowledge from the example dataset and predicts new labels for unknown inputs. Formally, given  $X$ , a set of all cells, and a training set,  $S$  of labeled cells  $(s,c)$ , where  $(s,c) \in (X \times C)$ , to learn a function  $f$ , such that  $f: X \rightarrow C$ , in other words, it maps a cell to one of the categories of  $C$ . Here,  $X$  represents as a vector of the above features and  $C$  represent the classes such that  $C = [\text{Active Cancer}, \text{Inactive Cancer}, \text{Healthy Cell}]$ . Theoretically, this problem formulation allows us to leverage any supervised classification algorithm that can handle multi-class scenarios. In this work, three algorithms were used for the experiment, (i) Naïve Bayes (NB), (ii) Support Vector Machine (SVM), and (iii) Random Forest Tree (RFT). NB is a probabilistic classifier based on the Bayes theorem for conditional probabilities whereas SVM is based on concepts from the statistical learning theory. RFT is a combination of decision trees where each tree votes for a preferred class and the majority voted class is considered as the final prediction. The accuracy, precision, recall, and F1-score were calculated to compare the performance of these three algorithms.

### 4.3. Results and Discussion

#### 4.3.1. Classification of Cell Gesture Using Supervised Methods

For cancer diagnosis, the primary goal is to accurately identify and count the number of cancer cells from blood sample where other cells are present. Once the classifier was modeled, the system was validated with untrained samples to measure the accuracy. A five-fold validation technique was used to measure the accuracy. In this technique, the entire dataset was randomized and then divided into five segments. Four segments were used to train the system and the remaining one was used to test the accuracy. The same approach was repeated for all combinations of train-test data segments (five possible combinations). The accuracy was calculated and compared to all three classifier models, Support Vector Machine (SVM), Random Forest Tree (RFT) and Naïve Bayes Classifier (NBC). The following equation was used to calculate the accuracy of the predicted result. Here,  $\hat{y}_i$  is the predicted label of the  $i$ -th sample,  $y_i$  is the corresponding true label, and  $N$  is the total number of samples analyzed.

$$Accuracy(y, \hat{y}) = \frac{1}{N_{samples}} \sum_{i=1}^N 1(\hat{y}_i = y_i)$$

Table 4.2 compares the accuracy of the three classifiers. The overall accuracy of the model to classify tumor cells and healthy cells were 90%, 82% and 85% using NBC, SVM, and RFT classifiers, respectively. The performance of the classifier depends on the type of dataset used to build the model. However, an overall accuracy of 85% validates the effectiveness of multiple feature analysis and applicability of machine learning algorithm for tumor cell diagnosis. Such high accuracy is achieved while the classification is fully automated and compatible for large-scale application without disturbing the cell microenvironment. The selectivity has been maintained with aptamers and the cell did not

have to be fluorescently stained either. Aptamers are also preferred over antibody for chemical stability and high selectivity.

Table 4.2. Average accuracy of classification using SVM, RFT, and NBC computed with five-fold validation technique. The standard deviation was calculated from the accuracy among the five combinations of training sets in cross-validation.

Classifier	Average Accuracy (%)
Naïve Bayes Classifier	90 ± 10
Support Vector Machine	82 ± 25
Random Forest Tree	85 ± 24

#### 4.3.2. Feature Ranking

From visual inspection of static images, it is easy to confuse a cancer cell with a healthy one. However, a combination of all the extracted feature vectors provided an opportunity to distinguish the cancer cell gestures. Machine learning algorithm provided a feasible approach to combine all the feature vectors and build a robust classifier. It should be borne in mind that classifying the samples from just a few feature vectors would be very challenging. A feature ranking chart using random forest tree (RFT) was created to demonstrate the importance of including all the feature vectors in constructing the classifier. A random forest is a collection of decision trees used for classification. Each of these decision trees consists of several feature vectors. The RFT classifier was trained with a known sample dataset and calculated the importance of every feature vector. Figure 4.6 shows the ranking of the top 25 features in descending order of importance. Overlapping large error bars represent that the importance of any individual feature is not significant enough to be a single discerning factor to distinguish the cell categories. The machine learning provided the combination of all the features to develop a complex decision-making algorithm to classify the dataset correctly.

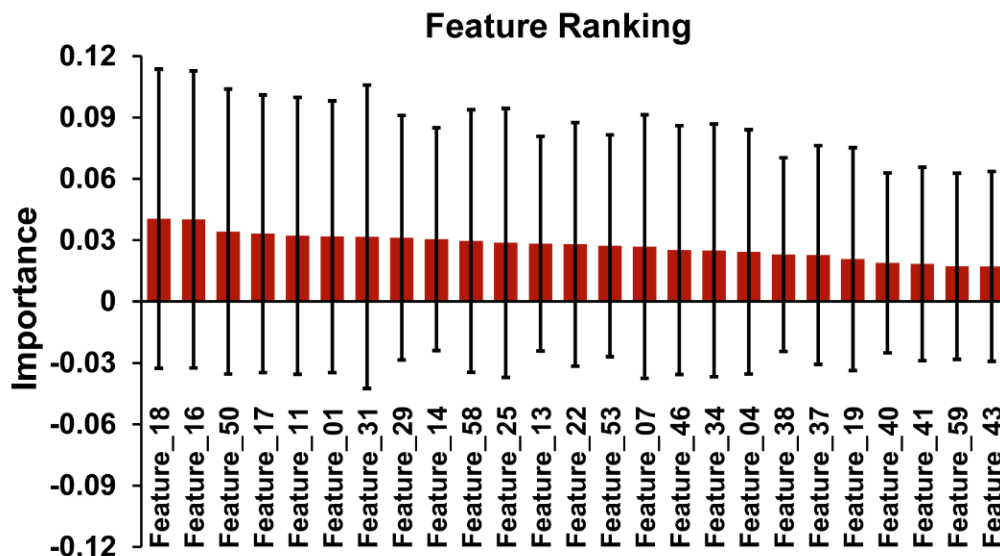


Figure 4.6. Feature ranking of the top 25 features in descending order of importance. The vertical lines represent the standard deviations of importance-metric.

### 4.3.3. Confusion Matrix Analysis

The difference in cell gesture of cancer and healthy cell is not always very obvious. Not all cancer cells would express very active behavior either. The model missed a few targets as some of the cancer cells did not show much activity on a functionalized surface. The gestures of a few cancer cells on control surface also appeared similar to the gestures of healthy cells. This could be a possible source of confusion for the model. To understand the false-positive and false-negative results, a normalized confusion matrix was calculated to compare among the three classifier models. SVM classifier was chosen because it scored the lowest accuracy. The confusion matrix in Figure 4.7 displays the matching of active, inactive, and control cells versus predicted annotations by the classifier. Each row represents the instances of actual cell type and each column of the matrix represents the instances for the predicted label by the classifier.

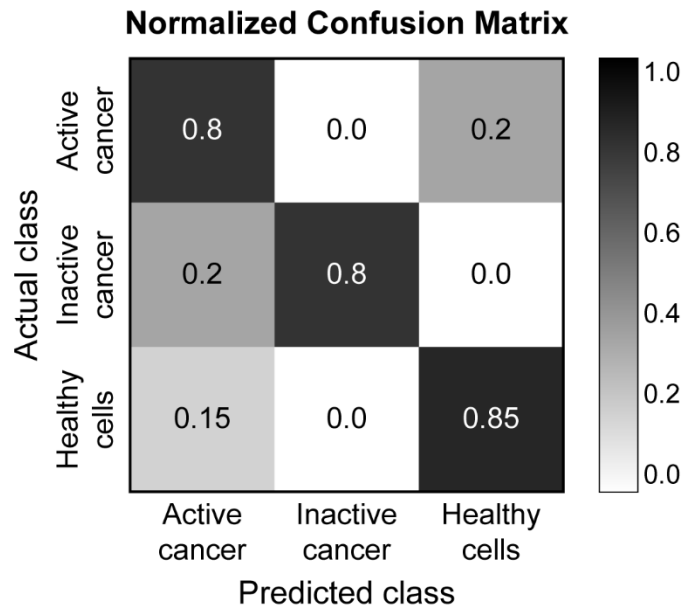


Figure 4.7. Confusion matrix of the SVM classifier for active cancer, inactive cancer, and healthy cell categories. The intensity bar represents the scale.

As shown in Figure 4.7, the diagonal digits represent the best accuracy for all three categories. The system correctly predicted cancer cells on anti-EGFR and mutant-aptamer surface in 80% cases. Among the tumor cells, 20% did not show remarkable activity to be identified as active cancer cells. On the other hand, all healthy cells were identified with 85% accuracy whereas remaining 15% showed similar gesture as active cancer cells. The accuracy could be improved with a larger dataset with more samples and features. However, 85% accuracy with this sample dataset validated the significance of machine learning algorithm for such applications.

#### **4.3.4. Comparison between Classifiers**

For cancer diagnosis, the measurement of false-positive and false-negative results can add significant complexity to the later prognosis. The system's ability in avoiding false-negative predictions is much more important than concluding a false-positive result. It is crucial not to miss any cancer cells rather than misunderstanding a healthy cell as cancerous one. The precision and recall value from predicted results were measured to

further analyze the performance of the model. The recall is the ratio of the number of true positives over the total number of actually positive instances. Precision is the ratio of the number of true positives over the total number of predicted positive instances. The following equations were used to calculate these two parameters. Here  $T_P$  = true positive,  $F_P$  = false-positive, and  $F_N$  = false-negative.

$$Recall (r) = \frac{T_P}{T_P + F_N} ; Precision(p) = \frac{T_P}{T_P + F_P} ; F_1 score = \frac{2pr}{p + r}$$

Table 4.3. Precision, recall and F1-score measurements (The maximum value of each column is shown in bold).

	Precision			Recall			F <sub>1</sub> -Score		
	Active	Inactive	Other	Active	Inactive	Other	Active	Inactive	Other
<b>NBC</b>	0.91	1.0	0.87	1.0	0.6	1.0	0.95	0.75	0.93
<b>SVC</b>	0.62	1.0	0.89	0.8	0.8	0.85	0.7	0.89	0.87
<b>RFT</b>	1.0	0.73	0.85	0.9	0.8	0.85	0.95	0.76	0.85

For all three classification models, the recall score is greater than 80% (Table 4.3). The recall-value for active tumor cells with the NBC model is 100%. Overall, the NBC performed better compared to the other two classifiers which as observed from  $F_1$ -score. The  $F_1$ -score is the harmonic mean of precision and recall. A good retrieval algorithm would maximize precision and recall simultaneously and score a large  $F_1$ -measure.

#### 4.3.5. Precision-Recall Curve Analysis

The precision-recall relation was also used to compare the performance of the three classifiers. Together, precision and recall represent a trade-off. One can be improved by compromising the performance of the other. For cancer diagnosis, a good

recall value is more important than the precision. Figure 4.8(a) shows the precision vs. recall values for the SVM classifier. The precision-recall curves for individual classes are shown with dotted lines. As seen from the plot, the classifier predicted the inactive tumor cells more accurately compared to the other two classes. It was possible to maintain a good precision while achieving a good recall score. The black solid line represents the overall average precision-recall performance of the SVM classifier.

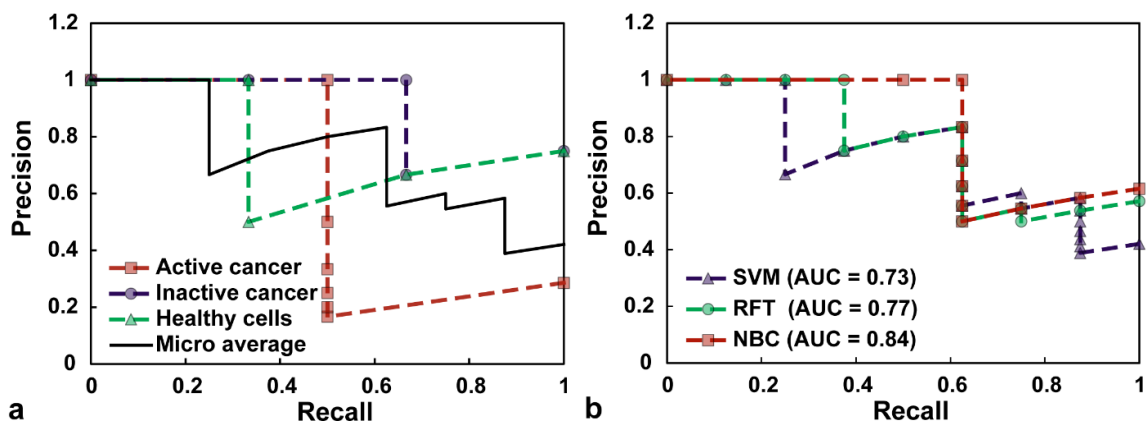


Figure 4.8. (a) Precision-Recall plot for the predictive model trained with SVM classifier. The black solid line represents the average performance of the model. (b) Performance comparison of three different classifiers. The average value of precision and recall are plotted here for each classifier model. The area under the curve (AUC) for each model is mentioned in the legend.

Figure 4.8(b) shows the average precision-recall performance of three classifiers. To compare the performance, the area under the curve (AUC) was calculated. A large AUC represents a better classifier in terms of error margins. SVM, RFT and NBC classifier scored AUC values of 0.73, 0.77, and 0.84, respectively. Among the three commonly used classifiers, the NBC performed best with the dataset and application.

The dynamic morphology of cells on an aptamer-functionalized surface can be a novel biomarker for detection of cancer cells. Both, cancerous and non-cancerous cells are present in biopsy samples from patients. This work demonstrates a fast and accurate

method to quantify cell gestures and distinguish hGBM cells from astrocytes based on their dynamic morphology from time-lapse images. Multiple factors can contribute to regulating cell protrusion, adhesion, and surface tension (cell rounding). Individual genes and signaling proteins can also modulate cell morphology [153]. The hGBM cells showed random extensions and contractions of pseudopods, whereas astrocyte cells did not show any distinct activity. This was due to many reasons and especially from the EGFR overexpression on hGBM cells and their affinity toward anti-EGFR aptamer/antibody [19, 167, 168]. Overexpression of EGFR and flexibility of cell membrane on hGBM cells allowed a higher number of binding interactions between EGFR and anti-EGFR aptamer [161, 169]. On the other hand, astrocytes did not show any change in their morphology on anti-EGFR and mutant aptamer surface in the 15-minute interval while the surfaces were imaged with the microscope camera. The less number of EGFR on astrocyte cell membrane could not instigate any interactions with the anti-EGFR-modified surface. This increased the cell motility of hGBM cells compared to that of astrocytes. The experiments were performed with solid-biopsy samples and the work can be expanded with liquid-biopsy samples too. Similar cell response can also be expected from other types of tumor cell with appropriate choice of aptamer functionalized surface. Thus, the approach can be extended to target other types of tumor cells (breast, lung, and prostate cancer samples) that are known to travel in the blood (e.g. circulating tumor cells).

This work utilized the cell motility on anti-EGFR aptamer-modified substrates as a new strategy to detect cancer cells. The cancer cells with overexpressed surface biomarkers (EGFR) interacted more with the aptamer-functionalized surface and showed distinct morphology. Noncancerous cells did not show such activity because they do not have high EGFR expression on the surface. The approach is very selective and this can be a good tool to analyze invasive and benign cancer cells where the number of



biomarkers expressed on different cell-membranes are different. Existing methods to quantify cell surface receptors commonly involves staining of cells with antibody-conjugated fluorescent or magnetic particles and then analyze them with an optical setup or magnetic sorter. These tools are expensive, bulky, and requires strict maintenance. Our approach used only a standard optical microscope and a CMOS camera. The analysis is packaged as software and can be used on any computer/mobile platform. Also, cell staining often restricts regular cellular functions which can be a concern for post-capture analysis. The advantage of this technique compared to others is that it is suitable for a quick diagnosis without much overhead. This method does not involve any cell staining. Furthermore, aptamers are chemically more stable than antibodies [170]. Aptamer-functionalized chips can be stored in controlled conditions for a few weeks. When the samples are available, cells can be seeded on the functionalized chips and imaged within 15 minutes to run the experiment.

Another advantage of the chip-based device is that it can be easily integrated with other microfluidic cell-capture platforms to serve as an additional modality to identify cancer cells based on their physical behavior. Dynamic morphology analysis can be a good cytological indicator to complement other chip-based detection techniques. It is also possible to introduce nanotexture on the surface to enhance the cell-surface interactions [171, 172]. If required, cleavable linkers can also be used for functionalization so that after the morphology analysis, cells could be released from the surface to perform other post-capture analysis [173].

This method is compatible with automated high-throughput imaging and can analyze a large volume of data in a short amount of time. Microscopic image assessment is still the most commonly used and available tool. It is financially and logistically feasible compared to other commonly used approaches like flow cytometry, x-ray radiography,

computed tomography (CT), positron emission tomography (PET), and magnetic resonance imaging (MRI). Most of these techniques are for advanced stage cancer diagnosis and have limited sensitivity. The method presented here uses only an optical microscope and does not require sophisticated infrastructure for device fabrication. This makes it simple to analyze whole-slide microscopic images without any fluorescent staining. The automation of the analysis makes it more suitable for large volume sample analysis which otherwise would not be very convenient and feasible to a human pathologist.

Cell segmentation is still one of the major challenges in automated image analysis workflow. For this work, bright field images and contrast analysis were used to isolate cells in a label-free environment. It is very important to focus the cells properly in order to capture their activity and avoid imaging artifacts. An out-of-focus image may appear different than a focused one which may create confusion in tracing the cell boundary from image contrast analysis. In this experiment, single plane images acquired from an optical microscope were used for simplicity. Cells were seeded on the aptamer-functionalized (anti-EGFR and mutant aptamer) glass surfaces and the surface was always kept in focus to minimize variability in the image acquisition process. Thus, all the images of the cells were captured at the same focal plane. An alignment mark on the glass surface was helpful to maintain the focal plane on the surface. However, it is also possible to use a confocal microscope and use 3D-stacked images to find the best focal plane. This may also help to detect the cell boundary more accurately.

However, cells can be tagged with fluorescent markers to facilitate the intensity-based segmentation scheme. It is known that tumor cells have a larger nucleus to cytoplasm ratio. The nucleus of the cells can also be stained to analyze the change in shape of the nucleus over time. Further characterization of the morphological behavior of

tumor cells in combination with molecular characteristics can provide additional valuable prognostic information about the primary tumor. A larger dataset and unsupervised machine learning can also be implemented to identify aberrant cell gestures. For larger dataset, the inclusion of selective features based on their importance can reduce over-fitting of the model and analysis time.

The presented approach can also be applied to investigate the role of individual genes in regulating time-resolved cell morphology and complex phenotypes. The change in cell gesture with disease progression is another aspect to explore. Since this method only requires an imaging setup, a central database can be maintained to store the cell gesture of different types of cancer cells and predicted results can be sent to local remote devices for off-site diagnosis. With the increased availability of live-cell screening microscopes, the cell gesture analysis can be a dominating technology for early detection of cancer in near future.

#### **4.4. Conclusion**

This work presented a simple and elegant approach to detect and classify cancer cells based on cell gesture using a machine learning technique. The dynamic morphology of cells was quantified with a number of unique features which were used to identify hGBM cells from healthy astrocytes. The identification scheme was validated with untrained data and three different classifiers were used to construct the system and compare the performances. The Naïve Bayes classifier identified the cancer cells with the highest accuracy. This work established the foundation for automated screening and classification of cancer from time-lapse optical micrographs. This can further be used to study cell behaviors for other types of diseases. Cell gesture analysis can be a simple platform to develop cost-effective and efficient point-of-care device to detect cancer at early stages.

## Chapter 5

### 5. Molecular Dynamics Study of Protein Deformation through Solid-State Nanopore

#### 5.1. Introduction

Over the past decade, nanopore technology has advanced substantially due to its capability for single molecule detection and characterization [174-178]. Nanopore devices have been used for label-free detection of DNA [179], RNA [180, 181], and also for rapid sequencing of DNA [182-184]. It is an attractive choice for sensitive and accurate detection of proteins and protein-complexes [174, 185, 186]. This work explores the structural deformation of a protein from a nanopore translocation.

Most of the early nanopore studies were done with biological nanopores like alpha-hemolysin or mycobacteria smegmatis porin A (MspA) [182, 187]. Solid-state nanopore emerged as an alternative choice and became more popular for its robustness, easy fabrication, high throughput, low cost, and scalability [178]. In the past decade, synthetic nanopores have been widely used for single molecule detection [175, 188-190]. Although silicon nitride ( $\text{Si}_3\text{N}_4$ ) is the most popular choice of material for synthetic nanopores [186, 188, 191, 192], other materials such as silicon dioxide ( $\text{SiO}_2$ ) [189, 193], aluminum-oxide ( $\text{Al}_2\text{O}_3$ ) [190], and graphene [194-197] have also been used to make nanopores. Several studies have been conducted on protein translocation through solid-state nanopore including protein transport [198], protein identification [186, 199], unfolding and stretching of protein [200], protein trapping [187], high voltage transport of protein [198], and localization of protein in a DNA [201]. In some cases, the inner wall of the nanopore is bioengineered with other biomaterials to mimic the biological nanopore [202]. Lipid-coated nanopore has been used to tailor protein translocation [203], aptamer coating on nanopore wall has been used for increased selectivity [92], chemical modification and metallization have been done for stochastic sensing of proteins [199].

The structural integrity of protein is a common concern during a nanopore-based protein detection process [188]. The stress caused by channel constriction during translocation or applied electric field may deform the 3D shape of a protein. Recent studies have shown that the biophysical properties of a protein are manipulated by variations in solvent or pH in a nano-confined environment [188, 204]. In addition, the thermal, chemical, and electrical field can influence interactions between the protein and pore which can trigger protein denaturation inside a nanopore [205]. Thus, a comprehensive understanding of the conformational changes is important because of the nature of detection using ionic current measurement. Study of the deformation can be a stepping stone for a comprehensive understanding of the orientation and interaction of the constituting amino acid molecules of protein. Computational analysis and simulation tools provide an exceptional advantage in such cases because it allows us to explore atomic level interactions which are rather difficult to grasp from experimental situations [206]. Several theoretical and computational analyses such as coarse-grained dynamic simulation [207], time distribution model [192], molecular dynamics [208, 209], and stochastic model [210] have been designed to study the translocation behavior and dynamics of protein molecule inside a nanopore [211]. Similar studies on deformation mechanism for DNA have been presented already [212-215]. The deformability of DNA structure under electric bias has been shown already [216].

This work focuses on the deformation of a protein inside a nanopore under the influence of applied bias. This is valuable for protein detection with nanopore as the function of a protein depends on the integrity of its conformal structure [217]. Nanoscale Molecular Dynamics (NAMD v2.9) was used to simulate the translocation of protein through a  $\text{Si}_3\text{N}_4$  pore and observed the deformation of protein structure [218]. Thrombin was selected as a proof of concept. The 3D structural deformation of thrombin was

measured using Visual Molecular Dynamics (VMD v1.9.2) while different electric fields were applied across the pore [219]. Thrombin is the protein responsible for thrombosis. Thrombin plays a vital role in cancer metastasis as well [220]. No mechanical force was used on the protein to ensure that only the influence of applied bias on the deformation was monitored. The model was simulated for 20 ns of translocation of protein using a multicore computing facility at Texas Advanced Computing Center (TACC) and analyzed the structural changes for different applied voltages. Root mean square deviation (RMSD) and Radial distribution function (RDF) from VMD were used to quantify the deviation of protein structure from its initial structure. The protein deformed gradually with the increase in electric field and although the overall size of the protein did not change much at a small voltage, the shape was stretched due to the presence of electric field. Such molecular dynamics (MD) simulation provided insight to investigate protein deformation in nanopore study before delving into laboratory experiment.

The basic principle of molecular translocation through a nanopore is very straightforward. A schematic is shown in Figure 5.1. The experimental setup includes two chambers separated by a solid-state nanopore. Typically the pore is drilled by high energy electron beam using Transmission Electron Microscope (TEM) or by using Focused Ion Beam (FIB) [189]. Although the ion beam has higher energy compared to electron-beam to drill a pore in a thicker membrane, a TEM offers better control and precision over the pore diameter because the size of the electron beam is much smaller than the size of ions used in FIB. The chambers are filled with buffer solution and electrodes are placed in the chambers to create an electric field high enough to force the target molecule to pass from one chamber to the other through the nano-aperture. The ionic current is measured with a patch-clamp measurement system. When a protein travels through the nanopore, a drop in the ionic current is registered. This current profile gives insights on the properties of the

molecule. The magnitude and duration of the current blockade are proportional to the size and the transition time of the passing analyte through the pore. In some cases, the pore is smaller than the molecule to measure the mechanophysical property of the translocating molecule. Figure 5.1 shows a cross-section of a  $\text{Si}_3\text{N}_4$  nanopore and a protein crossing the pore due to the applied bias.

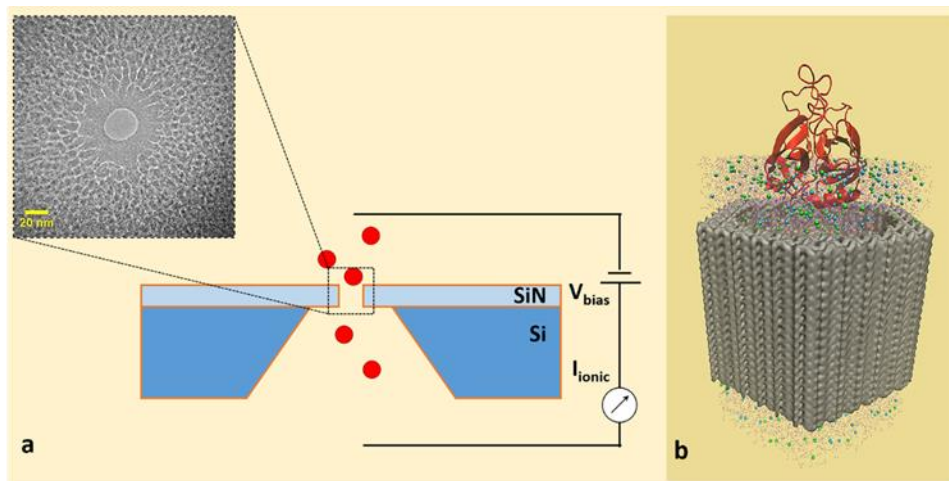


Figure 5.1. (a) Schematic representation of nanopore experiment to capture the ionic current signature for protein translocation. The inset shows an actual TEM drilled pore. (b) Model of the simulated system: all-atom MD model comprised of a thrombin inside a  $\text{Si}_3\text{N}_4$  nanopore. The pore is solvated with KCl. The inner diameter of the pore is 6 nm, simulated periodic cell structure was  $68 \text{ \AA} \times 78 \text{ \AA} \times 96 \text{ \AA}$ .

## 5.2. Materials and Methods

### 5.2.1. Simulation Details

NAMD v2.9 was used to simulate the experiment [218]. VMD v1.9.2 was used for visualization and data analysis of the simulated results [219]. The protocol for MD model is similar to the one reported by Aksimentiev et al. [221]. The CHARMM22 model was used for the force field calculation [222, 223]. All simulations were performed on computer clusters (includes 6400 nodes each configured with two Xeon E5-2680 processors and one Intel Xeon Phi SE10P Coprocessor (on a PCIe card)). Each node was configured with

32GB of 'host' memory with an additional 8GB of memory on the Xeon Phi coprocessor card) at Texas Advanced Computing Center (TACC) using 240 cores in parallel. Thrombin was selected as a sample protein. The structure of thrombin was obtained from the Research Collaboratory for Structural Bioinformatics (RCSB). The protein data bank (PDB) file, 1HAP, contained the x-ray resolved configuration of a thrombin-oligomer complex [224]. VMD was used to extract the structure of human alpha-thrombin. The protein had two major chains, chain-L and chain-H with 36 and 259 amino acids, respectively. The pore diameter was selected to be slightly larger than the protein size to negate the effect of protein deformation due to pore constriction. The pore was placed in the z-direction and the protein was electrophoretically driven through the nanopore.

### **5.2.2. Model Construction**

The simulation consisted of a 6 nm thick block of  $\text{Si}_3\text{N}_4$  containing a 6 nm diameter nanopore at the center. First, a crystalline structure of  $\text{Si}_3\text{N}_4$  unit cell was created. Then the unit cell was replicated and assembled in order to form a 10 nm x 10 nm x 6 nm  $\text{Si}_3\text{N}_4$  membrane. Since the longest dimension of thrombin is 4.7 nm in its native state, a 6 nm diameter nanopore was created at the center of the membrane. The membrane was given a hexagonal shape to reduce the total number of atoms ensuring better simulation speed. The atom count for the complete nanopore model was 11,016. The pore was solvated with 1M KCl solution. Salt concentration was chosen close to standard experimental conditions [225]. Since no mechanical force was applied, the protein was electrophoretically driven through the nanopore.

Each simulation was executed in three steps. First, the total system energy was minimized by conjugate gradient method to ensure a stable system. Energy minimization involves finding the minimum energy landscape where the molecule is relaxed, by systematically varying the positions of atoms and calculating the energy in an iterative



manner. Then the temperature of the system was raised to 295 K gradually at constant volume (i.e. in NVT ensemble) followed by an equilibration at constant pressure and temperature (i.e. NPT ensemble). Finally, an electric potential was applied across the nanopore along the z-axis at constant volume. The simulation was performed for 20 ns at 1 fs steps. The applied electric field was varied from 0 to 1 kCal/(mol.Å.e) for each system using equation 1 [221]. The trajectory frames were recorded every 800 fs in 20 ns duration.

$$E - field_z \left( \frac{kCal}{mol.\text{\AA}.e} \right) = \frac{-23.060549 \times U}{l_z} \text{ (V/\text{\AA})};$$

Here,  $U$  is the potential difference and  $l_z$  is the size of the whole system along the z-axis. The NAMD unit for electric field is kCal/(mol.Å.e), 23.0605492 is the conversion factor for  $U$  (volts) and  $l_z$  (angstroms).

### **5.2.3. Nanopore Construction and Energy Minimization**

The simulation consisted of a 6 nm thick block of Si<sub>3</sub>N<sub>4</sub> containing a 6 nm diameter nanopore at the center. First, a crystalline structure of Si<sub>3</sub>N<sub>4</sub> unit cell was created in NAMD. Then the unit cell was replicated and assembled in order to form a Si<sub>3</sub>N<sub>4</sub> membrane. The dimension of the membrane was 10 nm x 10 nm with a uniform thickness of 6 nm. A cylindrically shaped nanopore was created at the center of the membrane by removing atoms from the center. The smallest diameter inside the nanopore was 6 nm. Figure 5.2(A) illustrates the construction of nanopore. Finally, the membrane was given a hexagonal shape large enough to surround the nanopore. This reduced the total number of atoms ensuring better simulation speed. The atom count for the complete nanopore model was 11,016. Thrombin was selected as a sample protein. The structure of thrombin was obtained from the Research Collaboratory for Structural Bioinformatics (RCSB). Any protein whose crystallographic structure is known could be used for the study. The longest dimension of thrombin is 4.7 nm in its native state. Since no mechanical force was applied,

the protein was electrophoretically driven through the nanopore. There were 394 residues in thrombin composed of total 3934 atoms in the system.

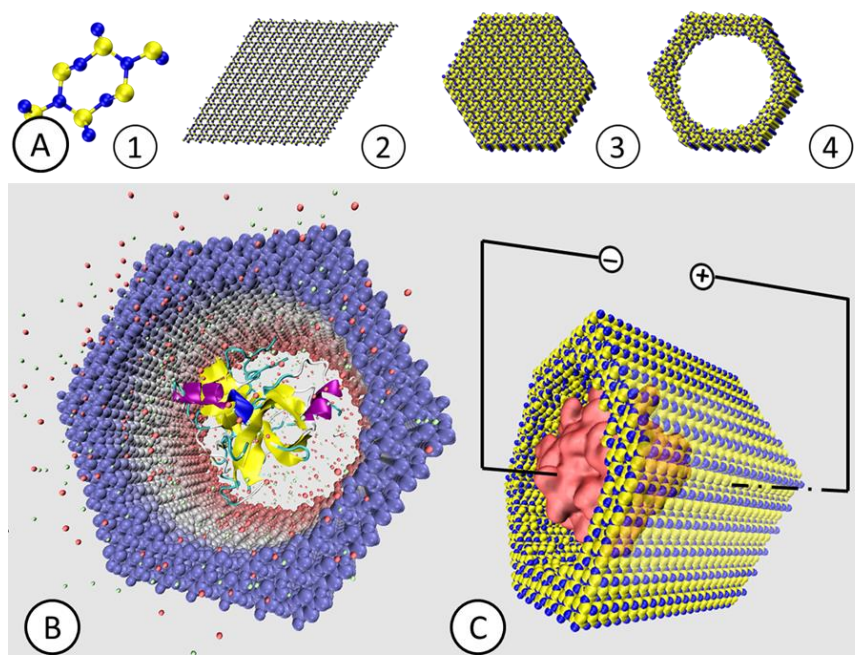


Figure 5.2. (A) Construction of  $\text{Si}_3\text{N}_4$  nanopore from a  $\text{Si}_3\text{N}_4$  unit cell using NAMD. (1)  $\text{Si}_3\text{N}_4$  unit cell; (2) Single-molecule thick  $\text{Si}_3\text{N}_4$  membrane; (3) the membrane is given a convenient geometry; (4) a nanopore in a  $\text{Si}_3\text{N}_4$  membrane. (B) Visualization of the thrombin molecule inside a  $\text{Si}_3\text{N}_4$  membrane (using VMD). Each color represents a different secondary structure. (C) The complete model of the system with molecular transport through nanopore under an applied bias.

All of the simulations were performed using NAMD2.9 with periodic boundary conditions under constant temperature and constant system volume known as NVT ensemble. Each simulation was executed in three steps. First, the total system energy was minimized by conjugate gradient method to ensure a stable system. Then the temperature of the system was raised to 295 K in 500 steps gradually at constant volume (i.e. in NVT ensemble) followed by an equilibration at constant pressure and temperature (i.e. NPT ensemble). The Langevin thermostat with  $5 \text{ ps}^{-1}$  damping constant was used to

maintain the desired temperature. During the equilibration, the temperature was kept at 295 K while applying Langevin forces. Finally, an electric potential was applied across the nanopore along the z-axis at constant volume. Both the equilibration and application of external electric field was performed for 20 ns at 1 fs steps. Before applying the electric field, the system was equilibrated by minimizing the energy to ensure a stable system. The system as can be seen from the energy curve (Figure 5.3). The total energy of the system dropped very quickly during stabilization and remained unchanged for the rest of the time.

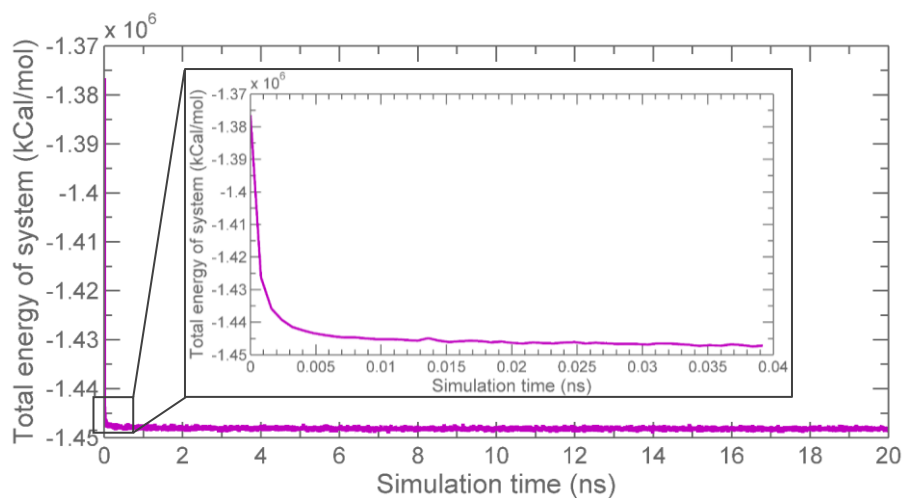


Figure 5.3. Energy minimization of the system with conjugate gradient method for 20 nanoseconds. The inset shows the minimization of energy during the first 40 picoseconds.

#### 5.2.4. Force-field Calculations

The interatomic and intermolecular force fields were estimated with CHARMM22 and CHARMM27 models because these are noteworthy for protein and DNA systems, respectively. The CHARMM22 model used a potential energy function  $U(R)$  defined by the following equation [222].

$$\begin{aligned}
U(R) = & \sum_{bonds} K_b(b - b_0)^2 + \sum_{UB} K_{UB}(S - S_0)^2 + \sum_{angle} K_\theta(\theta - \theta_0)^2 \\
& + \sum_{dihedrals} K_\chi(1 + \cos(n\chi - \delta)) + \sum_{impropers} K_{imp}(\varphi - \varphi_0)^2 \\
& + \sum_{nonbond} \epsilon_{ij} \left[ \left( \frac{R_{min_{ij}}}{r_{ij}} \right)^{12} - \left( \frac{R_{min_{ij}}}{r_{ij}} \right)^6 \right] + \frac{q_i q_j}{\epsilon_1 r_{ij}};
\end{aligned}$$

Where,  $K_b$ ,  $K_{UB}$ ,  $K_\theta$ ,  $K_\chi$ ,  $K_{imp}$  are the force constants associated with bonds, Urey-Bradley, angles, dihedrals, and improper dihedral angles, respectively.  $b$ ,  $S$ ,  $\theta$ ,  $\chi$ ,  $\varphi$ ,  $n$ , and  $\delta$  represent the bond length, Urey-Bradley-distance, bond angle, dihedral angle, improper torsion angle, phase shift, and multiplicity or periodicity of the dihedral angle, respectively. The last two terms of the equation describe the van der Waals energy calculated with Lennard-Jones potential and the electrostatic energy assessed from Coulombic potential. Here  $\epsilon$  and  $r_{ij}$  are effective dielectric constant, and distance between atoms  $i$  and  $j$ . The  $\epsilon_{ij}$  values were established by the geometric mean of  $\epsilon_i$  and  $\epsilon_j$  and  $R_{min_{ij}}$  values were calculated from the arithmetic mean of  $R_{min_i}$  and  $R_{min_j}$ .

### 5.3. Results and Discussion

The thrombin molecule was placed inside the nanopore and the change in its structure was observed for different electric potentials applied across the nanopore. The electric field was set to 0.0, 0.05, 0.10 and 1.0 kCal/(mol.Å.e) along the z-axis. The deformation was quantified by the root mean square deviation (RMSD) of protein backbone with its initial conformation having the two structures in best alignment with each other. The formula for RMSD calculation is given by the following equation.

$$RMSD_\alpha(t_j) = \sqrt{\frac{\sum_{\alpha=1}^{N_\alpha} (r_\alpha(t_j) - \langle r_\alpha \rangle)^2}{N_\alpha}},$$

$$\langle r_\alpha \rangle = \frac{1}{N_t} \sum_{j=1}^{N_t} r_\alpha(t_j);$$

Where  $N_\alpha$  is the number of atoms whose positions are being compared.  $N_t$  is the number of time steps over which the positions were compared,  $r_\alpha(t_j)$  is the position of atom  $\alpha$  at time  $t_j$  and  $\langle r_\alpha \rangle$  is the average value of the position of atom  $\alpha$ . VMD was used to calculate the RMSD of the protein structure for each frame at every 0.8 ps interval for the total time span of 20 ns.

Figure 5.4 shows the RMSD plot of thrombin's shape at different electric fields. The deformation in thrombin's structure was insignificant for low electric fields such as 0.05 and 0.1 kCal/(mol.Å.e). At these voltage levels, the force fields were not strong enough to deform the protein's structure. Proteins are made of amino acids. The net charge of a protein depends on its isoelectric point and pH. In the presence of an electric field, these amino acids tend to reorder themselves due to the electrostatic field to attain the lowest possible energy state. This resulted in a slightly deformed structure of the molecule. Higher voltage would produce larger electrostatic force and cause more deformation. The results showed that an electric field as high as 1 kCal/(mol.Å.e) deformed the protein by approximately 16% from its initial structure within the first 20 ns. The trend of the deformation suggested that more deformation would occur for a longer exposure to this electric field. However, a high voltage in a nanopore experiment would reduce the protein translocation time to facilitate a high-throughput analysis but at the cost of further deformation in protein structure.

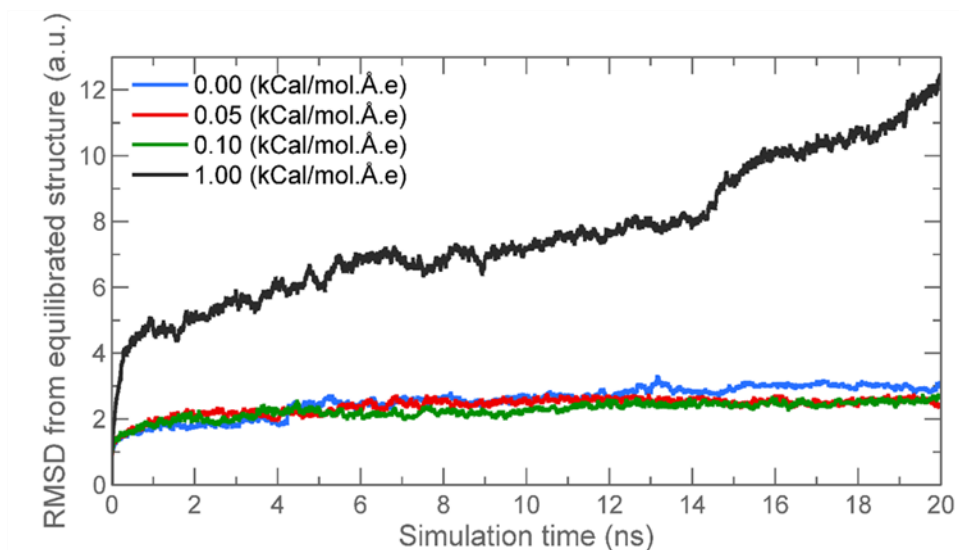


Figure 5.4. Root mean squared deviation (RMSD) of the protein backbone compared with the initial conformation.

In a typical nanopore experiment, protein molecules move through the nanopore due to their charge which in turn is defined by their isoelectric point and the pH of the solution in the presence of an electric field [226]. A complete protein translocation event is approximately a few hundred microseconds to milliseconds [185, 186]. The isoelectric point of human thrombin is 7.0–7.6 [227]. Since the pH of the solution was ~7.0, the thrombin was slightly positively charged. As a result, it traveled towards the negative potential. A complete protein translocation event is approximately a few hundred microseconds to milliseconds [185, 186]. An MD simulation with such long event would require unreasonable processing power and time. The simulations performed here were done for 20 ns. Although it was very short compared to typical experiment, it was possible to precisely monitor the movement even within 20 ns because of the detailed information captured by MD simulations. The center of mass (COM) of the molecule was calculated and the movement of the COM was tracked over time. Then the projection of the overall movement along the three axes (x, y, and z) were calculated. The correlation between the protein's overall movement and the projection in a particular axis was calculated to find

the direction of movement. The maximum correlation coefficient ( $0.963 \pm 0.025$ ) was observed with the z-axis component for all three bias situations. This validated that the overall movement was along the z-axis which was the same direction for the applied electric field. The same was observed from the trajectory of the molecule in VMD.

The radial distribution function,  $g(r)$ , of thrombin's structure was also calculated to observe how the atoms of the protein were distributed and how this distribution was affected by the external electric field. In statistical mechanics, the radial distribution function of a system describes how the density of particles varies as a function of distance from a reference point. It is a useful tool utilized in molecular dynamics to describe the structure of a system. It measures the probability of finding a neighboring atom with respect to distance from another one. The  $g(r)$  of thrombin's 3D structure was computed by calculating the interatomic distance of every particle pair and binning them in a histogram. The histogram was then normalized by the volume of a spherical shell with thickness,  $\delta r$ . This was achieved by multiplying the density function with the volume of a spherical shell at distance  $r$  shown in the following equation.

$$g(r) = \frac{1}{N} \frac{dn(r)}{4\pi r^2 dr \rho}$$

Here,  $N$  represents the total number of atoms,  $\rho$  is the number density, and  $dn(r)$  is the number of atoms at a distance  $r$  and  $r+dr$ .

The radial distribution function for thrombin's structure at different electric fields is shown in Figure 5.5(a) and 5.5(b). The horizontal axis is the distance around an atom, while the vertical axis in Figure 5.5(a) represents the number of atom-pairs available at a distance given on the x-axis. The position of the peak represents the most common distance between two atoms. At higher electric field, there is a right shift of the curve. That

means the most probable distance between any two atoms increased approximately from 2.2 nm to ~2.6 nm due to the large electric field. Hence the atoms in the protein went apart from each other. The expansion of the curve along horizontal axis also suggests that the protein got stretched under a higher electric field.

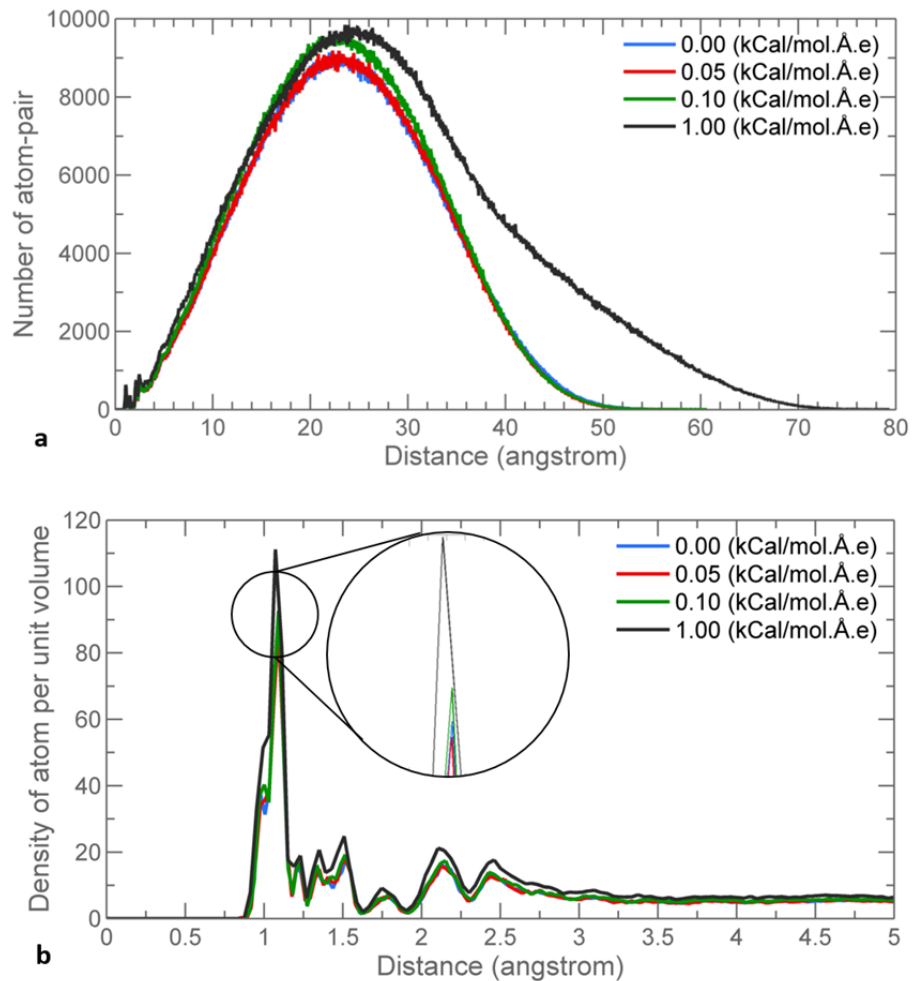


Figure 5.5. (a) Radial distribution analysis of thrombin's structure after 20 ns simulation at increasing electric fields. The vertical axis represents the number of atom-pair at a distance mentioned in the horizontal axis. (b) Normalized radial distributions function. The density of atoms lying on the surface of a sphere at the listed distance from an atom.

Figure 5.5(b) is the normalized version of 5.5(a). The vertical axis here shows the number of neighboring atoms present in an imaginary sphere of that distance. The position



of the prominent peak over here is around 1 Å, which refers to the radius of the imaginary sphere around an atom to have the highest atom density. There is no significant shift in the position of this peak. However, the height of the dominant peak has increased by approximately 20% from its initial position at the high electric fields. It means that at the very vicinity of an atom the neighboring atoms were more tightly packed in the presence of the higher electric field. This was again a result of stretched deformation.

To measure the effect of protein deformation on the ionic current profile, the average ionic current was measured through the pore. Ideally, proteins are suspended in an ionic solution in nanopore experiments. When there is no protein inside the nanopore, the setup only measures the ionic current from the movements of K<sup>+</sup> and Cl<sup>-</sup> ions. This is registered as the baseline current. During translocation, the protein molecule blocked a certain amount of KCl ions through the cylindrical pore. This current blockage depends on the size and charge of the translocating molecule and also the charge of the K<sup>+</sup> and Cl<sup>-</sup> atoms. The ionic current profiles for four different electric fields ranging from 0 to 1 kCal/(mol.Å.e) were recorded. Since the state of the MD system was recorded after every 800 fs, the current profile was recorded from the change in total electric charge in between two consecutive time-frames. These calculations were done for the entire 20 ns time span. Equation 5 represents current calculation, where,  $z_i$  and  $q_i$  are z-coordinate and charge of ion  $i$ , respectively, and  $\Delta t$  is the simulation step [228].

$$I(t + \Delta t/2) = \frac{1}{\Delta t l_z} \sum_{i=1}^N q_i (z_i(t + \Delta t) - z_i(t))$$

The current-voltage (I-V) profile of the system was calculated to understand the equivalent resistance introduced by the protein (Figure 5.6). At higher electric field, more ions passed through the nanopore resulting in an increase in the current. It is visible from

the plot that the nanopore current increased linearly as the applied voltage increased. The linear I-V profile suggests that the protein, while inside the nanopore, offered a constant resistance even when it was slightly deformed due to the electric field.

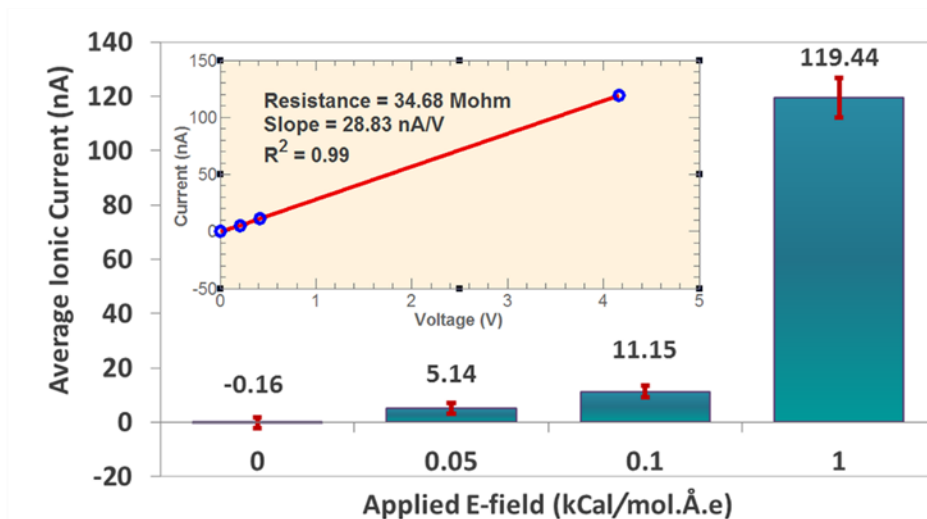


Figure 5.6. Current-Voltage profile of the system. The average ionic current is linearly dependent on the applied potential when the protein is inside the nanopore. The inset shows the linear relationship between the two entities. The data points are interpolated with linear regression analysis.

Figure 5.5 in conjunction with the RMSD plot suggests that the protein showed deformation in the shape with more atomic packing. This led to an overall enlargement of the protein's shape at a higher electric field. The protein went through stretching associated with the forces in the nanopore in response to high voltage. Since the force was exerted in the direction of travel, the structure got stretched in the same direction. This did not affect the overall blocking of the pore by that much and hence was not visible through the ionic current profile. This phenomenon may not be very crucial for nanopore experiments with DNA or polymer chains but should be considered for studying size sensitive biomolecules such as proteins.

#### **5.4. Conclusion**

A computational model for sensing protein translocations through nanopores was shown here. The interatomic interactions and translocation of thrombin through a  $\text{Si}_3\text{N}_4$  nanopore was studied using this model. The conformal structure of the protein that yields its particular functional form and also the alterations in protein structure are important to understand. A comprehensive analysis has been presented to quantify the behavior of a model protein inside a solid-state nanopore under external electric field. The protein underwent gradual deformation at high applied voltage. The structural deformability, atomic displacement, and ionic current for thrombin passing through a nanopore were quantified. The presented framework allowed a closer inspection on the underlying processes of a nanopore experiment. This knowledge can be translated into design rules for protein measurement experiments with solid-state nanopore and also further protein deformation study.

## Chapter 6

### 6. Future research directions

#### 6.1. Introduction

In this chapter, scopes of future works that can complement/supplement the current research are discussed.

#### 6.2. Effect of Nanotexture and Stiffness of Substrate in Cell Adhesion

In chapter 3, a quick and easy method of creating nanotextured polymer was presented. The application of nanotextured PDMS in cell capture was also demonstrated. However, the same approach can be implemented to explore different patterns and roughness of nanotexture and its effect in cell adhesion, cell viability, attachment, and cell migration studies. Other moldable polymers, such as gelatin and hydrogel can be used to create a nanotextured substrate and explore the effect of substrate material in cancer cell experiments. Different ratio of PDMS and curing agent can be used to create different surfaces having different stiffness but same roughness to investigate the role of surface stiffness in cell adhesion and interactions.

#### 6.3. Diagnosis of Different Cell Types using Dynamic Morphology Analysis

The cell gesture identification method was demonstrated for brain tumor cells and healthy astrocytes. The overexpression of EGFR on hGBM cells made it possible to utilize cell behavior on the anti-EGFR modified surface as a metric to identify cancer cells. However, overexpression of biomarkers on cancer cells is common. Hence, a surface functionalized with anti-EpCAM or anti-HER aptamer can be used to quantify gesture for other types of cancer cells such as breast cancer and lung cancer.

#### **6.4. Cell Gesture at Different Stages of Cancer**

The expression of surface receptors on cancer cells depends on the origin and the stage of cancer. Therefore, the interaction between cancer cells and surface immobilized capture molecules could be an indicator to determine the staging of cancer. The functionalized nanotextured substrates and the cell gesture analysis can both be used to design experiments to explore the staging of cancer. The activity of cancer cells before and after metastasis is also known to be different. So the dynamic morphology analysis can be used to distinguish metastatic cancer cells from non-metastatic ones.

#### **6.5. MD Simulation for EGFR and EGFR-aptamer Complex Translocation through Nanopore**

Computer simulations provide a bridge between macroscopic laboratory experiments and microscopic understanding of the underlying physics. An MD simulation can be used to design different nanopore models to study the deformation dynamics of a protein in nanopore experiment. Optimization of the diameter and depth of the pore can be done before investing in laboratory experiments. Recently, nanopore devices are being used for protein-complex detection. Protein biomarkers can be selectively labeled with aptamer and a nanopore device can quantify the number of target sample through ionic current measurements. Such experiments can also be modeled using MD simulations for optimizing experimental process parameters.

## Chapter 7

### 7. Conclusion

In this dissertation, we discussed the importance of early detection for effective diagnosis and treatment of cancer. A few devices and technologies for detection of cancer cells were reviewed here. We have demonstrated the use of a simple flexible nanotextured polymer-based device to capture cancer cells. We presented a one-step fabrication method of creating nanotexture in a polymer and showed a modular approach to integrate nanotextured polymer into microfluidics. Biofunctionalized nanotextured PDMS showed enhanced cell-surface interactions to facilitate cell capture and the modular assembly provided easy access to captured cells for post-capture analysis. We also presented a novel approach to analyze the dynamic morphology of cells on a biofunctionalized surface. We used this technique to identify cancer cells from its gestures. The interaction between the protein biomarker on cancer cell surface and the surface immobilized aptamers triggered the cells to show distinct morphological change. We used machine learning algorithms to classify cancer and healthy cells from cell gestures. We also developed a molecular dynamics model of protein biomarker detection using nanopore. The computational model allowed us to understand protein deformation mechanism under electric fields in a nanopore experiment.

## References

1. Siegel, R.L., K.D. Miller, and A. Jemal, *Cancer statistics, 2017*. CA: A Cancer Journal for Clinicians, 2017. **67**(1): p. 7-30.
2. McCabe, M.S., et al., *American Society of Clinical Oncology statement: achieving high-quality cancer survivorship care*. Journal of Clinical Oncology, 2013. **31**(5): p. 631-640.
3. Statistics, N.C.f.H., *Health, United States, 2015: with special feature on racial and ethnic health disparities*. 2016.
4. Data, M., *Leading Causes of Death, 1900-1998*. Centers for Disease Control and Prevention Website ([www.cdc.gov/nchs/nvss/mortality\\_historical\\_data.htm](http://www.cdc.gov/nchs/nvss/mortality_historical_data.htm)), 1950.
5. Weiss, R., et al., *Retroviruses: ancient and modern*, in *100 Years of Virology*. 1999, Springer. p. 171-177.
6. Gallis, B., M. Linial, and R. Eisenman, *An avian oncovirus mutant deficient in genomic RNA: characterization of the packaged RNA as cellular messenger RNA*. Virology, 1979. **94**(1): p. 146-161.
7. Duncan, I., *Evidence for an oncovirus in swimbladder fibrosarcoma of Atlantic salmon *Salmo salar* L*. Journal of Fish Diseases, 1978. **1**(1): p. 127-131.
8. Eisenman, R., R. Shaikh, and W.S. Mason, *Identification of an avian oncovirus polyprotein in uninfected chick cells*. Cell, 1978. **14**(1): p. 89-104.
9. Chaffer, C.L. and R.A. Weinberg, *A perspective on cancer cell metastasis*. Science, 2011. **331**(6024): p. 1559-1564.
10. Kerr, J.F., C.M. Winterford, and B.V. Harmon, *Apoptosis. Its significance in cancer and cancer therapy*. Cancer, 1994. **73**(8): p. 2013-2026.
11. Knudson, A.G., *Two genetic hits (more or less) to cancer*. Nature reviews. Cancer, 2001. **1**(2): p. 157.
12. Brenner, D.J., et al., *Estimated risks of radiation-induced fatal cancer from pediatric CT*. American journal of roentgenology, 2001. **176**(2): p. 289-296.
13. Klein, C.A., *The metastasis cascade*. Science, 2008: p. 1785-1787.
14. Liotta, L., et al., *Tumor invasion and metastases: biochemical mechanisms*, in *New Directions in Cancer Treatment*. 1989, Springer. p. 381-398.
15. Schroeder, A., et al., *Treating metastatic cancer with nanotechnology*. Nature reviews. Cancer, 2012. **12**(1): p. 39.
16. Goetz, T., *The Riddle of Early Detection!* Wired magazine, 2008.

17. Blumen, H., K. Fitch, and V. Polkus, *Comparison of treatment costs for breast cancer, by tumor stage and type of service*. American health & drug benefits, 2016. **9**(1): p. 23.
18. Stoscheck, C.M. and L.E. King, *Role of epidermal growth factor in carcinogenesis*. Cancer research, 1986. **46**(3): p. 1030-1037.
19. Carpenter, G. and S. Cohen, *Epidermal growth factor*. Annual review of biochemistry, 1979. **48**(1): p. 193-216.
20. Nicholson, R., J. Gee, and M. Harper, *EGFR and cancer prognosis*. European journal of cancer, 2001. **37**: p. 9-15.
21. McLendon, R.E., et al., *Glioma-associated antigen expression in oligodendroglial neoplasms: tenascin and epidermal growth factor receptor*. Journal of Histochemistry & Cytochemistry, 2000. **48**(8): p. 1103-1110.
22. Hong, W.K. and A. Ullrich, *The role of EGFR in solid tumors and implications for therapy*. Oncol. Biother, 2000. **1**(1).
23. Carpenter, G., *The biochemistry and physiology of the receptor-kinase for epidermal growth factor*. Molecular and cellular endocrinology, 1983. **31**(1): p. 1-19.
24. Michnick, S.W. and S.S. Sidhu, *Submitting antibodies to binding arbitration*. Nature chemical biology, 2008. **4**(6): p. 326-329.
25. Goldenberg, D.M., *Monoclonal antibodies in cancer detection and therapy*. The American journal of medicine, 1993. **94**(3): p. 297-312.
26. Cordell, J.L., et al., *Immunoenzymatic labeling of monoclonal antibodies using immune complexes of alkaline phosphatase and monoclonal anti-alkaline phosphatase (APAAP complexes)*. Journal of Histochemistry & Cytochemistry, 1984. **32**(2): p. 219-229.
27. Tockman, M.S., et al., *Sensitive and specific monoclonal antibody recognition of human lung cancer antigen on preserved sputum cells: a new approach to early lung cancer detection*. Journal of Clinical Oncology, 1988. **6**(11): p. 1685-1693.
28. Heller, M.J., *DNA microarray technology: devices, systems, and applications*. Annual review of biomedical engineering, 2002. **4**(1): p. 129-153.
29. Chen, G., et al., *Array-based technologies and their applications in proteomics*. Current topics in medicinal chemistry, 2003. **3**(6): p. 705-724.
30. Sefah, K., et al., *Development of DNA aptamers using Cell-SELEX*. Nature protocols, 2010. **5**(6): p. 1169.



31. Vona, G., et al., *Isolation by size of epithelial tumor cells: a new method for the immunomorphological and molecular characterization of circulating tumor cells*. The American journal of pathology, 2000. **156**(1): p. 57-63.
32. Pereira, P., et al., *Passive circulating cell sorting by deformability using a microfluidic gradual filter*. Lab on a Chip, 2013. **13**(1): p. 161-170.
33. Yoon, Y., et al., *Clogging-free microfluidics for continuous size-based separation of microparticles*. Scientific reports, 2016. **6**: p. 26531.
34. Zheng, S., et al., *3D microfilter device for viable circulating tumor cell (CTC) enrichment from blood*. Biomedical microdevices, 2011. **13**(1): p. 203-213.
35. Xu, W., et al., *Cell stiffness is a biomarker of the metastatic potential of ovarian cancer cells*. PloS one, 2012. **7**(10): p. e46609.
36. Swaminathan, V., et al., *Mechanical stiffness grades metastatic potential in patient tumor cells and in cancer cell lines*. Cancer research, 2011. **71**(15): p. 5075-5080.
37. Gossett, D.R., et al., *Hydrodynamic stretching of single cells for large population mechanical phenotyping*. Proceedings of the National Academy of Sciences, 2012. **109**(20): p. 7630-7635.
38. Dudani, J.S., et al., *Pinched-flow hydrodynamic stretching of single-cells*. Lab on a Chip, 2013. **13**(18): p. 3728-3734.
39. Warkiani, M.E., et al., *Ultra-fast, label-free isolation of circulating tumor cells from blood using spiral microfluidics*. Nature protocols, 2016. **11**(1): p. 134-148.
40. Warkiani, M.E., et al., *An ultra-high-throughput spiral microfluidic biochip for the enrichment of circulating tumor cells*. Analyst, 2014. **139**(13): p. 3245-3255.
41. Warkiani, M.E., et al., *Slanted spiral microfluidics for the ultra-fast, label-free isolation of circulating tumor cells*. Lab on a Chip, 2014. **14**(1): p. 128-137.
42. Renier, C., et al., *Label-free isolation of prostate circulating tumor cells using Vortex microfluidic technology*. npj Precision Oncology, 2017. **1**(1): p. 15.
43. Dhar, M., et al., *Label-free enumeration, collection and downstream cytological and cytogenetic analysis of circulating tumor cells*. Scientific reports, 2016. **6**: p. 35474.
44. Nathamgari, S.S.P., et al., *Isolating single cells in a neurosphere assay using inertial microfluidics*. Lab on a Chip, 2015. **15**(24): p. 4591-4597.
45. Dhar, M., et al., *High efficiency vortex trapping of circulating tumor cells*. Biomicrofluidics, 2015. **9**(6): p. 064116.

46. Lin, H.K., et al., *Portable filter-based microdevice for detection and characterization of circulating tumor cells*. *Clinical Cancer Research*, 2010. **16**(20): p. 5011-5018.
47. Barlogie, B., et al., *Flow cytometry in clinical cancer research*. *Cancer research*, 1983. **43**(9): p. 3982-3997.
48. Krüger, J., et al., *Development of a microfluidic device for fluorescence activated cell sorting*. *Journal of micromechanics and microengineering*, 2002. **12**(4): p. 486.
49. Pamme, N. and C. Wilhelm, *Continuous sorting of magnetic cells via on-chip free-flow magnetophoresis*. *Lab on a Chip*, 2006. **6**(8): p. 974-980.
50. Hoshino, K., et al., *Microchip-based immunomagnetic detection of circulating tumor cells*. *Lab on a Chip*, 2011. **11**(20): p. 3449-3457.
51. Myklatun, A., et al., *Microfluidic sorting of intrinsically magnetic cells under visual control*. *Scientific Reports*, 2017. **7**.
52. Karabacak, N.M., et al., *Microfluidic, marker-free isolation of circulating tumor cells from blood samples*. *Nature protocols*, 2014. **9**(3): p. 694-710.
53. Nagrath, S., et al., *Isolation of rare circulating tumour cells in cancer patients by microchip technology*. *Nature*, 2007. **450**(7173): p. 1235-1239.
54. Stott, S.L., et al., *Isolation of circulating tumor cells using a microvortex-generating herringbone-chip*. *Proceedings of the National Academy of Sciences*, 2010. **107**(43): p. 18392-18397.
55. Gleghorn, J.P., et al., *Capture of circulating tumor cells from whole blood of prostate cancer patients using geometrically enhanced differential immunocapture (GEDI) and a prostate-specific antibody*. *Lab on a chip*, 2010. **10**(1): p. 27-29.
56. Sarioglu, A.F., et al., *A microfluidic device for label-free, physical capture of circulating tumor cell clusters*. *Nature methods*, 2015. **12**(7): p. 685-691.
57. Chen, W., et al., *Nanoroughened surfaces for efficient capture of circulating tumor cells without using capture antibodies*. *ACS nano*, 2012. **7**(1): p. 566-575.
58. Asghar, W., et al., *Synthesis of nano-textured biocompatible scaffolds from chicken eggshells*. *Nanotechnology*, 2012. **23**(47): p. 475601.
59. Islam, M., et al., *Nanotextured polymer substrates show enhanced cancer cell isolation and cell culture*. *Nanotechnology*, 2015. **26**(22): p. 225101.
60. Yoon, Y., D. Kim, and J.-B. Lee, *Hierarchical micro/nano structures for super-hydrophobic surfaces and super-lyophobic surface against liquid metal*. *Micro and Nano Systems Letters*, 2014. **2**(1): p. 3.

61. Rahman, A., et al., *Sub-50-nm self-assembled nanotextures for enhanced broadband antireflection in silicon solar cells*. Nature communications, 2015. **6**.
62. Siddique, R.H., G. Gomard, and H. Hölscher, *The role of random nanostructures for the omnidirectional anti-reflection properties of the glasswing butterfly*. Nature communications, 2015. **6**: p. 6909.
63. Dou, X., et al., *Bioinspired Hierarchically Structured Surfaces for Efficient Capture and Release of Circulating Tumor Cells*. ACS Applied Materials & Interfaces, 2017. **9**(10): p. 8508-8518.
64. Han, W., et al., *Nanoparticle coatings for enhanced capture of flowing cells in microtubes*. ACS nano, 2009. **4**(1): p. 174-180.
65. Zhang, N., et al., *Electrospun TiO<sub>2</sub> nanofiber-based cell capture assay for detecting circulating tumor cells from colorectal and gastric cancer patients*. Advanced Materials, 2012. **24**(20): p. 2756-2760.
66. Yoon, H.J., et al., *Sensitive capture of circulating tumour cells by functionalized graphene oxide nanosheets*. Nature nanotechnology, 2013. **8**(10): p. 735-741.
67. Lee, S.-K., et al., *Nanowire substrate-based laser scanning cytometry for quantitation of circulating tumor cells*. Nano letters, 2012. **12**(6): p. 2697-2704.
68. Sekine, J., et al., *Functionalized conducting polymer nanodots for enhanced cell capturing: the synergistic effect of capture agents and nanostructures*. Advanced Materials, 2011. **23**(41): p. 4788-4792.
69. Wang, S., et al., *Highly efficient capture of circulating tumor cells by using nanostructured silicon substrates with integrated chaotic micromixers*. Angewandte Chemie International Edition, 2011. **50**(13): p. 3084-3088.
70. Mahmood, M.A.I., et al., *Micro+ nanotexturing of substrates to enhance ligand-assisted cancer cell isolation*. Nanotechnology, 2014. **25**(47): p. 475102.
71. Nair, S., et al., *Role of size scale of ZnO nanoparticles and microparticles on toxicity toward bacteria and osteoblast cancer cells*. Journal of Materials Science: Materials in Medicine, 2009. **20**(1): p. 235.
72. Rogers, J.A. and R.G. Nuzzo, *Recent progress in soft lithography*. Materials today, 2005. **8**(2): p. 50-56.
73. Oliva, M.R. and S. Saini, *Liver cancer imaging: role of CT, MRI, US and PET*. Cancer imaging, 2004. **4**(Spec No A): p. S42.
74. Weissleder, R., *Scaling down imaging: molecular mapping of cancer in mice*. Nature Reviews Cancer, 2002. **2**(1): p. 11-18.

75. Quon, A. and S.S. Gambhir, *FDG-PET and beyond: molecular breast cancer imaging*. Journal of clinical oncology, 2005. **23**(8): p. 1664-1673.
76. Estelrich, J., M.J. Sánchez-Martín, and M.A. Busquets, *Nanoparticles in magnetic resonance imaging: from simple to dual contrast agents*. International journal of nanomedicine, 2015. **10**: p. 1727.
77. Revia, R.A. and M. Zhang, *Magnetite nanoparticles for cancer diagnosis, treatment, and treatment monitoring: recent advances*. Materials Today, 2016. **19**(3): p. 157-168.
78. Ntouroupi, T., et al., *Detection of circulating tumour cells in peripheral blood with an automated scanning fluorescence microscope*. British journal of cancer, 2008. **99**(5): p. 789-795.
79. Guber, A., et al., *Computerized analysis of cytology and fluorescence in situ hybridization (FISH) in induced sputum for lung cancer detection*. Cancer cytopathology, 2010. **118**(5): p. 269-277.
80. Ojansivu, V., et al., *Automated classification of breast cancer morphology in histopathological images*. Diagnostic Pathology, 2013. **8**(1): p. S29.
81. Loukas, C., et al., *Breast cancer characterization based on image classification of tissue sections visualized under low magnification*. Computational and mathematical methods in medicine, 2013. **2013**.
82. Carpenter, A.E., et al., *CellProfiler: image analysis software for identifying and quantifying cell phenotypes*. Genome biology, 2006. **7**(10): p. R100.
83. Held, M., et al., *CellCognition: time-resolved phenotype annotation in high-throughput live cell imaging*. Nature methods, 2010. **7**(9): p. 747-754.
84. Laksameethanasan, D., et al., *cellXpress: a fast and user-friendly software platform for profiling cellular phenotypes*. BMC bioinformatics, 2013. **14**(16): p. S4.
85. Weeraratna, A.T., et al., *Wnt5a signaling directly affects cell motility and invasion of metastatic melanoma*. Cancer cell, 2002. **1**(3): p. 279-288.
86. Sahai, E., *Mechanisms of cancer cell invasion*. Current opinion in genetics & development, 2005. **15**(1): p. 87-96.
87. Lauffenburger, D.A. and A.F. Horwitz, *Cell migration: a physically integrated molecular process*. Cell, 1996. **84**(3): p. 359-369.
88. Kourou, K., et al., *Machine learning applications in cancer prognosis and prediction*. Computational and structural biotechnology journal, 2015. **13**: p. 8-17.

89. Cruz, J.A. and D.S. Wishart, *Applications of machine learning in cancer prediction and prognosis*. Cancer informatics, 2006. **2**: p. 59.
90. Branton, D., et al., *The potential and challenges of nanopore sequencing*. Nature biotechnology, 2008. **26**(10): p. 1146-1153.
91. Clarke, J., et al., *Continuous base identification for single-molecule nanopore DNA sequencing*. Nature nanotechnology, 2009. **4**(4): p. 265-270.
92. Rotem, D., et al., *Protein detection by nanopores equipped with aptamers*. Journal of the American Chemical Society, 2012. **134**(5): p. 2781-2787.
93. Murray, R.W., *Nanoelectrochemistry: metal nanoparticles, nanoelectrodes, and nanopores*. Chemical reviews, 2008. **108**(7): p. 2688-2720.
94. Han, A., et al., *Label-free detection of single protein molecules and protein–protein interactions using synthetic nanopores*. Analytical chemistry, 2008. **80**(12): p. 4651-4658.
95. Li, S., et al., *Fabrication of gelatin nanopatterns for cell culture studies*. Microelectronic Engineering, 2013. **110**: p. 70-74.
96. Im, S.G., et al., *Grafted conducting polymer films for nano-patterning onto various organic and inorganic substrates by oxidative chemical vapor deposition*. Advanced Materials, 2007. **19**(19): p. 2863-2867.
97. Gogolides, E., K. Ellinas, and A. Tserepi, *Hierarchical micro and nano structured, hydrophilic, superhydrophobic and superoleophobic surfaces incorporated in microfluidics, microarrays and lab on chip microsystems*. Microelectronic Engineering, 2015. **132**: p. 135-155.
98. Vlachopoulou, M.-E., et al., *Protein arrays on high-surface-area plasma-nanotextured poly (dimethylsiloxane)-coated glass slides*. Colloids and Surfaces B: Biointerfaces, 2011. **83**(2): p. 270-276.
99. Wan, Y., et al., *Nanotextured substrates with immobilized aptamers for cancer cell isolation and cytology*. Cancer, 2012. **118**(4): p. 1145-1154.
100. Vetrone, F., et al., *Nanoscale oxidative patterning of metallic surfaces to modulate cell activity and fate*. Nano letters, 2009. **9**(2): p. 659-665.
101. Ferraris, S., et al., *Micro-and nano-textured, hydrophilic and bioactive titanium dental implants*. Surface and Coatings Technology, 2015. **276**: p. 374-383.
102. Tserepi, A., et al., *Plasma nanotextured polymeric surfaces for controlling cell attachment and proliferation: a short review*. Plasma Chemistry and Plasma Processing, 2016. **36**(1): p. 107-120.

103. Chen, W., et al., *Nanotopography influences adhesion, spreading, and self-renewal of human embryonic stem cells*. ACS nano, 2012. **6**(5): p. 4094-4103.
104. Di Mundo, R., et al., *Cell adhesion on nanotextured slippery superhydrophobic substrates*. Langmuir, 2011. **27**(8): p. 4914-4921.
105. Koufaki, N., et al., *Controlling cell adhesion via replication of laser micro/nano-textured surfaces on polymers*. Biofabrication, 2011. **3**(4): p. 045004.
106. Jiang, P., J. Liang, and C. Lin, *Construction of micro–nano network structure on titanium surface for improving bioactivity*. Applied Surface Science, 2013. **280**: p. 373-380.
107. Park, J., et al., *Directed migration of cancer cells by the graded texture of the underlying matrix*. Nature materials, 2016. **15**(7): p. 792.
108. Kim, T.-H., et al., *Controlling differentiation of adipose-derived stem cells using combinatorial graphene hybrid-pattern arrays*. Acs Nano, 2015. **9**(4): p. 3780-3790.
109. Yoon, H.J., M. Kozminsky, and S. Nagrath, *Emerging role of nanomaterials in circulating tumor cell isolation and analysis*. ACS nano, 2014. **8**(3): p. 1995-2017.
110. Wang, B., et al., *Effect of surface nanotopography on immunoaffinity cell capture in microfluidic devices*. Langmuir, 2011. **27**(17): p. 11229-11237.
111. Hughes, A.D. and M.R. King, *Use of naturally occurring halloysite nanotubes for enhanced capture of flowing cells*. Langmuir, 2010. **26**(14): p. 12155-12164.
112. Wang, S., et al., *Three-Dimensional Nanostructured Substrates toward Efficient Capture of Circulating Tumor Cells*. Angewandte Chemie, 2009. **121**(47): p. 9132-9135.
113. Islam, M., et al., *Electrical Profiling and Aptamer Functionalized Nanotextured Surface in a Single Biochip for the Detection of Tumor Cells*. Functional Nanostructures, 2016. **1**(1): p. 13-21.
114. Mahmood, M.A.I., et al., *One-step tumor detection from dynamic morphology tracking on aptamer-grafted surfaces*. Technology, 2015. **3**(04): p. 194-200.
115. Wan, Y., et al., *Nanostructured polystyrene well plates allow unbiased high-throughput characterization of circulating tumor cells*. ACS applied materials & interfaces, 2014. **6**(23): p. 20828-20836.
116. Islam, M., et al., *Effects of nanotexture on electrical profiling of single tumor cell and detection of cancer from blood in microfluidic channels*. Scientific reports, 2015. **5**.

117. Tsougeni, K., et al., *Plasma nanotextured polymeric lab-on-a-chip for highly efficient bacteria capture and lysis*. Lab on a Chip, 2016. **16**(1): p. 120-131.
118. Nečas, D. and P. Klapetek, *Gwyddion: an open-source software for SPM data analysis*. Open Physics, 2012. **10**(1): p. 181-188.
119. Moynihan, H. and A. Crean, *Physicochemical Basis of Pharmaceuticals*. 2009: Oxford University Press.
120. Abhyankar, V.V., et al., *A Reversibly Sealed, Easy Access, Modular (SEAM) Microfluidic Architecture to Establish In Vitro Tissue Interfaces*. PloS one, 2016. **11**(5): p. e0156341.
121. Maya, S., et al., *Cetuximab conjugated O-carboxymethyl chitosan nanoparticles for targeting EGFR overexpressing cancer cells*. Carbohydrate polymers, 2013. **93**(2): p. 661-669.
122. Rho, J.K., et al., *Epithelial to mesenchymal transition derived from repeated exposure to gefitinib determines the sensitivity to EGFR inhibitors in A549, a non-small cell lung cancer cell line*. Lung Cancer, 2009. **63**(2): p. 219-226.
123. Sirotnak, F.M., et al., *Efficacy of cytotoxic agents against human tumor xenografts is markedly enhanced by coadministration of ZD1839 (Iressa), an inhibitor of EGFR tyrosine kinase*. Clinical Cancer Research, 2000. **6**(12): p. 4885-4892.
124. Meiser, F., C. Cortez, and F. Caruso, *Biofunctionalization of Fluorescent Rare-Earth-Doped Lanthanum Phosphate Colloidal Nanoparticles*. Angewandte Chemie International Edition, 2004. **43**(44): p. 5954-5957.
125. Amin, D.N., et al., *Tumor endothelial cells express epidermal growth factor receptor (EGFR) but not ErbB3 and are responsive to EGF and to EGFR kinase inhibitors*. Cancer research, 2006. **66**(4): p. 2173-2180.
126. Wikstrand, C.J., et al., *Cell surface localization and density of the tumor-associated variant of the epidermal growth factor receptor, EGFRvIII*. Cancer research, 1997. **57**(18): p. 4130-4140.
127. Auvinen, K., S. Jalkanen, and M. Salmi, *Expression and function of endothelial selectins during human development*. Immunology, 2014. **143**(3): p. 406-415.
128. Pottratz, S.T., et al., *P-selectin-mediated attachment of small cell lung carcinoma to endothelial cells*. American Journal of Physiology-Lung Cellular and Molecular Physiology, 1996. **271**(6): p. L918-L923.

129. Richter, U., et al., *Adhesion of small cell lung cancer cells to E-and P-selectin under physiological flow conditions: implications for metastasis formation*. Histochemistry and cell biology, 2011. **135**(5): p. 499-512.
130. Yu, M., et al., *Circulating breast tumor cells exhibit dynamic changes in epithelial and mesenchymal composition*. science, 2013. **339**(6119): p. 580-584.
131. Yu, M., et al., *Circulating tumor cells: approaches to isolation and characterization*. The Journal of cell biology, 2011. **192**(3): p. 373-382.
132. Miyamoto, D.T., L.V. Sequist, and R.J. Lee, *Circulating tumour cells - monitoring treatment response in prostate cancer*. Nature reviews Clinical oncology, 2014. **11**(7): p. 401-412.
133. Asghar, W., et al., *Electrical fingerprinting, 3D profiling and detection of tumor cells with solid-state micropores*. Lab on a Chip, 2012. **12**(13): p. 2345-2352.
134. Byun, S., et al., *Characterizing deformability and surface friction of cancer cells*. Proceedings of the National Academy of Sciences, 2013. **110**(19): p. 7580-7585.
135. Helenius, J., et al., *Single-cell force spectroscopy*. Journal of cell science, 2008. **121**(11): p. 1785-1791.
136. Gascoyne, P.R. and S. Shim, *Isolation of circulating tumor cells by dielectrophoresis*. Cancers, 2014. **6**(1): p. 545-579.
137. Wan, Y., et al., *Capture, isolation and release of cancer cells with aptamer-functionalized glass bead array*. Lab on a Chip, 2012. **12**(22): p. 4693-4701.
138. Basu, S., et al., *Purification of specific cell population by fluorescence activated cell sorting (FACS)*. JoVE (Journal of Visualized Experiments), 2010(41): p. e1546-e1546.
139. Fu, A.Y., et al., *A microfabricated fluorescence-activated cell sorter*. Nature biotechnology, 1999. **17**(11): p. 1109-1111.
140. Talasaz, A.H., et al., *Isolating highly enriched populations of circulating epithelial cells and other rare cells from blood using a magnetic sweeper device*. Proceedings of the National Academy of Sciences, 2009. **106**(10): p. 3970-3975.
141. Carpenter, A.E., *Image-based chemical screening*. Nature Chemical Biology, 2007. **3**(8): p. 461-465.
142. Eggert, U.S. and T.J. Mitchison, *Small molecule screening by imaging*. Current opinion in chemical biology, 2006. **10**(3): p. 232-237.
143. Loo, L.-H., L.F. Wu, and S.J. Altschuler, *Image-based multivariate profiling of drug responses from single cells*. Nature methods, 2007. **4**(5): p. 445-453.



144. Carpenter, A.E. and D.M. Sabatini, *Systematic genome-wide screens of gene function*. Nature Reviews Genetics, 2004. **5**(1): p. 11-22.
145. Kiger, A., et al., *A functional genomic analysis of cell morphology using RNA interference*. Journal of biology, 2003. **2**(4): p. 27.
146. Kenny, P.A., et al., *The morphologies of breast cancer cell lines in three-dimensional assays correlate with their profiles of gene expression*. Molecular oncology, 2007. **1**(1): p. 84-96.
147. Conrad, C. and D.W. Gerlich, *Automated microscopy for high-content RNAi screening*. The Journal of cell biology, 2010. **188**(4): p. 453-461.
148. Neumann, B., et al., *High-throughput RNAi screening by time-lapse imaging of live human cells*. Nature methods, 2006. **3**(5): p. 385-390.
149. Neumann, B., et al., *Phenotypic profiling of the human genome by time-lapse microscopy reveals cell division genes*. Nature, 2010. **464**(7289): p. 721-727.
150. Wan, Y., et al., *Surface-immobilized aptamers for cancer cell isolation and microscopic cytology*. Cancer research, 2010. **70**(22): p. 9371-9380.
151. Wan, Y., et al., *Velocity effect on aptamer-based circulating tumor cell isolation in microfluidic devices*. The Journal of Physical Chemistry B, 2011. **115**(47): p. 13891-13896.
152. Wan, Y., et al., *Proliferation and migration of tumor cells in tapered channels*. Biomedical microdevices, 2013. **15**(4): p. 635-643.
153. Bakal, C., et al., *Quantitative morphological signatures define local signaling networks regulating cell morphology*. science, 2007. **316**(5832): p. 1753-1756.
154. Beck, A.H., et al., *Systematic analysis of breast cancer morphology uncovers stromal features associated with survival*. Science translational medicine, 2011. **3**(108): p. 108ra113-108ra113.
155. Boland, M.V. and R.F. Murphy, *A neural network classifier capable of recognizing the patterns of all major subcellular structures in fluorescence microscope images of HeLa cells*. Bioinformatics, 2001. **17**(12): p. 1213-1223.
156. Price, J.H., et al., *Advances in molecular labeling, high throughput imaging and machine intelligence portend powerful functional cellular biochemistry tools*. Journal of cellular biochemistry, 2002. **87**(S39): p. 194-210.
157. Hanif, M., et al., *An accelerated framework for the classification of biological targets from solid-state micropore data*. Computer methods and programs in biomedicine, 2016. **134**: p. 53-67.

158. Hamaguchi, N., A. Ellington, and M. Stanton, *Aptamer beacons for the direct detection of proteins*. Analytical biochemistry, 2001. **294**(2): p. 126-131.
159. Keefe, A.D., S. Pai, and A. Ellington, *Aptamers as therapeutics*. Nature reviews Drug discovery, 2010. **9**(7): p. 537-550.
160. Song, Y., et al., *Selection of DNA aptamers against epithelial cell adhesion molecule for cancer cell imaging and circulating tumor cell capture*. Analytical chemistry, 2013. **85**(8): p. 4141-4149.
161. Barker, F.G., et al., *EGFR overexpression and radiation response in glioblastoma multiforme*. International Journal of Radiation Oncology\* Biology\* Physics, 2001. **51**(2): p. 410-418.
162. Sok, J.C., et al., *Mutant epidermal growth factor receptor (EGFRvIII) contributes to head and neck cancer growth and resistance to EGFR targeting*. Clinical Cancer Research, 2006. **12**(17): p. 5064-5073.
163. Singh, S.K., et al., *Identification of human brain tumour initiating cells*. nature, 2004. **432**(7015): p. 396.
164. Brescia, P., et al., *CD133 is essential for glioblastoma stem cell maintenance*. Stem cells, 2013. **31**(5): p. 857-869.
165. Wang, R., et al., *Glioblastoma stem-like cells give rise to tumour endothelium*. Nature, 2010. **468**(7325): p. 829.
166. Sethian, J.A., *A fast marching level set method for monotonically advancing fronts*. Proceedings of the National Academy of Sciences, 1996. **93**(4): p. 1591-1595.
167. Franovic, A., et al., *Translational up-regulation of the EGFR by tumor hypoxia provides a nonmutational explanation for its overexpression in human cancer*. Proceedings of the National Academy of Sciences, 2007. **104**(32): p. 13092-13097.
168. Maheswaran, S., et al., *Detection of mutations in EGFR in circulating lung-cancer cells*. New England Journal of Medicine, 2008. **359**(4): p. 366-377.
169. Cross, S.E., et al., *Nanomechanical analysis of cells from cancer patients*. Nature nanotechnology, 2007. **2**(12): p. 780-783.
170. Jayasena, S.D., *Aptamers: an emerging class of molecules that rival antibodies in diagnostics*. Clinical chemistry, 1999. **45**(9): p. 1628-1650.
171. Mansur, N., et al., *Functionalization of nanotextured substrates for enhanced identification of metastatic breast cancer cells*. Nanotechnology, 2017. **28**(28).

172. Hasan, M.R., et al., *One-step fabrication of flexible nanotextured PDMS as a substrate for selective cell capture*. Biomedical Physics & Engineering Express, 2017.
173. Zheng, Q., S.M. Iqbal, and Y. Wan, *Cell detachment: post-isolation challenges*. Biotechnology advances, 2013. **31**(8): p. 1664-1675.
174. Howorka, S. and Z.S. Siwy, *Nanopores as protein sensors*. Nature biotechnology, 2012. **30**(6): p. 506-507.
175. Miles, B.N., et al., *Single molecule sensing with solid-state nanopores: novel materials, methods, and applications*. Chemical Society Reviews, 2013. **42**(1): p. 15-28.
176. Movileanu, L., *Interrogating single proteins through nanopores: challenges and opportunities*. Trends in biotechnology, 2009. **27**(6): p. 333-341.
177. Stoloff, D.H. and M. Wanunu, *Recent trends in nanopores for biotechnology*. Current opinion in biotechnology, 2013. **24**(4): p. 699-704.
178. Venkatesan, B.M. and R. Bashir, *Nanopore sensors for nucleic acid analysis*. Nature nanotechnology, 2011. **6**(10): p. 615-624.
179. Wanunu, M., et al., *Electrostatic focusing of unlabelled DNA into nanoscale pores using a salt gradient*. Nature nanotechnology, 2010. **5**(2): p. 160-165.
180. Butler, T.Z., J.H. Gundlach, and M. Troll, *Ionic current blockades from DNA and RNA molecules in the  $\alpha$ -hemolysin nanopore*. Biophysical journal, 2007. **93**(9): p. 3229-3240.
181. Butler, T.Z., J.H. Gundlach, and M.A. Troll, *Determination of RNA orientation during translocation through a biological nanopore*. Biophysical journal, 2006. **90**(1): p. 190-199.
182. Manrao, E.A., et al., *Reading DNA at single-nucleotide resolution with a mutant MspA nanopore and phi29 DNA polymerase*. Nature biotechnology, 2012. **30**(4): p. 349-353.
183. Sigalov, G., et al., *Detection of DNA sequences using an alternating electric field in a nanopore capacitor*. Nano letters, 2008. **8**(1): p. 56-63.
184. Wells, D.B., et al., *Assessing graphene nanopores for sequencing DNA*. Nano letters, 2012. **12**(8): p. 4117-4123.
185. Ali, W., et al., *Differentiation of Specific Cancer Biomarkers with Solid-state Nanopores*. Functional Nanostructures, 2016: p. 26-34.

186. Han, A., et al., *Sensing protein molecules using nanofabricated pores*. Applied Physics Letters, 2006. **88**(9): p. 3901.
187. Mohammad, M.M., et al., *Controlling a single protein in a nanopore through electrostatic traps*. Journal of the American Chemical Society, 2008. **130**(12): p. 4081-4088.
188. Fologea, D., et al., *Electrical characterization of protein molecules by a solid-state nanopore*. Applied Physics Letters, 2007. **91**(5): p. 053901.
189. Storm, A., et al., *Fabrication of solid-state nanopores with single-nanometre precision*. Nature materials, 2003. **2**(8): p. 537-540.
190. Venkatesan, B.M., et al., *Highly sensitive, mechanically stable nanopore sensors for DNA analysis*. Advanced Materials, 2009. **21**(27): p. 2771-2776.
191. Niedzwiecki, D.J., et al., *Sampling a biomarker of the human immunodeficiency virus across a synthetic nanopore*. ACS nano, 2013. **7**(4): p. 3341-3350.
192. Plesa, C., et al., *Fast translocation of proteins through solid state nanopores*. Nano letters, 2013. **13**(2): p. 658-663.
193. Kim, M.J., et al., *Rapid fabrication of uniformly sized nanopores and nanopore arrays for parallel DNA analysis*. Advanced Materials, 2006. **18**(23): p. 3149-3153.
194. Garaj, S., et al., *Graphene as a subnanometre trans-electrode membrane*. Nature, 2010. **467**(7312): p. 190-193.
195. Merchant, C.A., et al., *DNA translocation through graphene nanopores*. Nano letters, 2010. **10**(8): p. 2915-2921.
196. Schneider, G.F., et al., *DNA translocation through graphene nanopores*. Nano letters, 2010. **10**(8): p. 3163-3167.
197. Venkatesan, B.M., et al., *Stacked graphene-Al<sub>2</sub>O<sub>3</sub> nanopore sensors for sensitive detection of DNA and DNA-protein complexes*. ACS nano, 2011. **6**(1): p. 441-450.
198. Cressiot, B., et al., *Protein transport through a narrow solid-state nanopore at high voltage: experiments and theory*. ACS nano, 2012. **6**(7): p. 6236-6243.
199. Wei, R., et al., *Stochastic sensing of proteins with receptor-modified solid-state nanopores*. Nature nanotechnology, 2012. **7**(4): p. 257-263.
200. Freedman, K.J., et al., *Single molecule unfolding and stretching of protein domains inside a solid-state nanopore by electric field*. Scientific reports, 2013. **3**.
201. Kowalczyk, S.W., A.R. Hall, and C. Dekker, *Detection of local protein structures along DNA using solid-state nanopores*. Nano letters, 2009. **10**(1): p. 324-328.

202. Kowalczyk, S.W., et al., *Single-molecule transport across an individual biomimetic nuclear pore complex*. Nature nanotechnology, 2011. **6**(7): p. 433-438.
203. Yusko, E.C., et al., *Controlling protein translocation through nanopores with bio-inspired fluid walls*. Nature nanotechnology, 2011. **6**(4): p. 253-260.
204. Lucent, D., V. Vishal, and V.S. Pande, *Protein folding under confinement: a role for solvent*. Proceedings of the National Academy of Sciences, 2007. **104**(25): p. 10430-10434.
205. Freedman, K.J., et al., *Chemical, thermal, and electric field induced unfolding of single protein molecules studied using nanopores*. Analytical chemistry, 2011. **83**(13): p. 5137-5144.
206. Aksimentiev, A., et al., *Computer Modeling in Biotechnology*. Nanostructure Design: Methods and Protocols, 2008: p. 181-234.
207. Lee, P.-H., V. Helms, and T. Geyer, *Coarse-grained Brownian dynamics simulations of protein translocation through nanopores*. The Journal of chemical physics, 2012. **137**(14): p. 145105.
208. Gumbart, J. and K. Schulten, *Molecular dynamics studies of the archaeal translocon*. Biophysical journal, 2006. **90**(7): p. 2356-2367.
209. Kannam, S.K., et al., *Sensing of protein molecules through nanopores: a molecular dynamics study*. Nanotechnology, 2014. **25**(15): p. 155502.
210. Kong, C.Y. and M. Muthukumar, *Simulations of stochastic sensing of proteins*. Journal of the American Chemical Society, 2005. **127**(51): p. 18252-18261.
211. Javidpour, L., M.R.R. Tabar, and M. Sahimi, *Molecular simulation of protein dynamics in nanopores. I. Stability and folding*. The Journal of chemical physics, 2008. **128**(11): p. 115105.
212. Heng, J.B., et al., *Stretching DNA using the electric field in a synthetic nanopore*. Nano letters, 2005. **5**(10): p. 1883-1888.
213. Heng, J.B., et al., *Sizing DNA using a nanometer-diameter pore*. Biophysical journal, 2004. **87**(4): p. 2905-2911.
214. Li, J., et al., *DNA molecules and configurations in a solid-state nanopore microscope*. Nature materials, 2003. **2**(9): p. 611-615.
215. Luan, B., et al., *Dynamics of DNA translocation in a solid-state nanopore immersed in aqueous glycerol*. Nanotechnology, 2012. **23**(45): p. 455102.

216. Mahmood, M.A.I., et al., *3D Structural Integrity and Interactions of Single-Stranded Protein-Binding DNA in a Functionalized Nanopore*. The Journal of Physical Chemistry B, 2014. **118**(22): p. 5799-5806.
217. Gething, M.-J. and J. Sambrook, *Protein folding in the cell*. Nature, 1992. **355**(6355): p. 33-45.
218. Kalé, L., et al., *NAMD2: greater scalability for parallel molecular dynamics*. Journal of Computational Physics, 1999. **151**(1): p. 283-312.
219. Humphrey, W., A. Dalke, and K. Schulten, *VMD: visual molecular dynamics*. Journal of molecular graphics, 1996. **14**(1): p. 33-38.
220. Nierodzik, M.L. and S. Karpatkin, *Thrombin induces tumor growth, metastasis, and angiogenesis: Evidence for a thrombin-regulated dormant tumor phenotype*. Cancer cell, 2006. **10**(5): p. 355-362.
221. Comer, J.R., D.B. Wells, and A. Aksimentiev, *Modeling nanopores for sequencing DNA*. DNA Nanotechnology: Methods and Protocols, 2011: p. 317-358.
222. MacKerell, A.D., et al., *CHARMM: the energy function and its parameterization*. Encyclopedia of computational chemistry, 1998.
223. MacKerell Jr, A.D., et al., *All-atom empirical potential for molecular modeling and dynamics studies of proteins†*. The journal of physical chemistry B, 1998. **102**(18): p. 3586-3616.
224. Padmanabhan, K. and A. Tulinsky, *An ambiguous structure of a DNA 15-mer thrombin complex*. Acta Crystallogr D Biol Crystallogr, 1996. **52**(Pt 2): p. 272-82.
225. Aksimentiev, A., *Deciphering ionic current signatures of DNA transport through a nanopore*. Nanoscale, 2010. **2**(4): p. 468-483.
226. Goldenberg, D.P. and T.E. Creighton, *Gel electrophoresis in studies of protein conformation and folding*. Analytical biochemistry, 1984. **138**(1): p. 1-18.
227. Berg, W., et al., *The isoelectric point of thrombin and its behaviour compared to prothrombin at some solid surfaces*. Thrombosis and haemostasis, 1979. **42**(3): p. 972-982.
228. Phillips, J.C., et al., *Scalable molecular dynamics with NAMD*. Journal of computational chemistry, 2005. **26**(16): p. 1781-1802.

## Biographical Information

Mohammad Hasan was born and raised in Dhaka, Bangladesh. He completed his Bachelor's degree in Electrical and Electronic Engineering from Bangladesh University of Engineering and Technology (BUET) Dhaka, Bangladesh in 2009. His undergraduate research was to develop improved I-V characteristics model for nanometer MESFETs. After graduation, Hasan worked as a lecturer in the Department of Electrical Engineering at United International University (UIU), Dhaka, Bangladesh till 2011. He also worked as a research consultant in Stochastic Logic from 2009 to 2011. He joined the University of Texas at Arlington in direct Doctoral program in Electrical Engineering (EE) Department in 2011. While working under the supervision of Dr. Samir Iqbal in NanoBioLab, he completed several projects in designing and fabricating biosensors for cancer detection. He also developed new techniques to study and analyze cancer biomarkers for early detection of cancer. During his Ph.D., Hasan also worked as a Graduate Teaching Assistant (GTA) in the EE department. Mohammad Hasan participated in numerous research outreach activities and volunteered in several engineering events. He won Outstanding GTA Mentor award, Engineering week challenge, Intellectual-engagement mentoring fellowship, and Kelcy Warren scholarship. He earned his Ph.D. in fall of 2017.

## Appendix

### **Permission from co-authors and publishers**




To whom it may concern

Subject: Permission to reuse/reprint a published/accepted/in-press manuscript in PhD dissertation

I am a co-author on the paper titled "One-Step Fabrication of Flexible Nanotextured PDMS as a Substrate for Selective Cell Capture" that is accepted for publication at Biomedical Physics & Engineering Express.

I grant permission to Mr. Mohammad Hasan to reuse/reprint this article in his PhD dissertation.

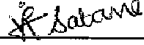
Name : SAI SANTOSH SASANK PERI  
Signature :   
Email : saisantosh.sasan.peri@mavs.uta.edu  
Date : 10/31/17

To whom it may concern

Subject: Permission to reuse/reprint a published/accepted/in-press manuscript in PhD dissertation

I am a co-author on the paper titled "One-Step Fabrication of Flexible Nanotextured PDMS as a Substrate for Selective Cell Capture" that is accepted for publication at Biomedical Physics & Engineering Express.

I grant permission to Mr. Mohammad Hasan to reuse/reprint this article in his PhD dissertation.

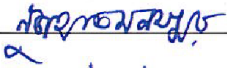
Name : Viraj Babane  
Signature :   
Email : Viraj.parag.babane@maas.era.edu  
Date : 10/30/2017

To whom it may concern

Subject: Permission to reuse/reprint a published/accepted/in-press manuscript in PhD dissertation

I am a co-author on the paper titled "One-Step Fabrication of Flexible Nanotextured PDMS as a Substrate for Selective Cell Capture" that is accepted for publication at Biomedical Physics & Engineering Express.

I grant permission to Mr. Mohammad Hasan to reuse/reprint this article in his PhD dissertation.

Name : NUZHAT MANSUR  
Signature :   
Email : nuzhat.mansur@mavs.uta.edu  
Date : 11/02/2017

To whom it may concern

Subject: Permission to reuse/reprint a published/accepted/in-press manuscript in PhD dissertation

I am a co-author on the paper titled “One-Step Fabrication of Flexible Nanotextured PDMS as a Substrate for Selective Cell Capture” that is accepted for publication at Biomedical Physics & Engineering Express.

I grant permission to Mr. Mohammad Hasan to reuse/reprint this article in his PhD dissertation.

Name : Jean Gao

Signature : 

Email : gao@uta.edu

Date : Oct 30, 2017

To whom it may concern

Subject: Permission to reuse/reprint a published/accepted/in-press manuscript in PhD dissertation

I am a co-author on the paper titled "One-Step Fabrication of Flexible Nanotextured PDMS as a Substrate for Selective Cell Capture" that is accepted for publication at Biomedical Physics & Engineering Express.

I grant permission to Mr. Mohammad Hasan to reuse/reprint this article in his PhD dissertation.


Name : Kyutai T. Nguyen  
Signature : kyutainguyen  
Email : knnguyen@uta.edu  
Date : 10/31/2017

To whom it may concern

Subject: Permission to reuse/reprint a published/accepted/in-press manuscript in PhD dissertation

I am a co-author on the paper titled “One-Step Fabrication of Flexible Nanotextured PDMS as a Substrate for Selective Cell Capture” that is accepted for publication at Biomedical Physics & Engineering Express.

I grant permission to Mr. Mohammad Hasan to reuse/reprint this article in his PhD dissertation.

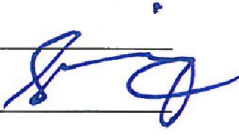
Name : \_Jon Weidanz\_  
Signature :   
Email : \_weidanz@uta.edu\_  
Date : \_November 2, 2017\_

To whom it may concern

Subject: Permission to reuse/reprint a published/accepted/in-press manuscript in PhD dissertation

I am a co-author on the paper titled "One-Step Fabrication of Flexible Nanotextured PDMS as a Substrate for Selective Cell Capture" that is accepted for publication at Biomedical Physics & Engineering Express.

I grant permission to Mr. Mohammad Hasan to reuse/reprint this article in his PhD dissertation.

Name : Samir M. Iqbal  
Signature :   
Email : sm.iqbal@utrgv.edu  
Date : 10/30/2017

Dear Mohammad Raziul Hasan,

Thank you for your email and for taking the time to seek this permission.

When you transferred the copyright in your article to IOP, we granted back to you certain rights, including the right to include all or part of the [Final Published Version](#) of the article within any thesis or dissertation. Please note you may need to obtain separate permission for any third party content you included within your article.

Please include citation details, “© IOP Publishing. Reproduced with permission. All rights reserved” and for online use, a link to the Version of Record.

The only restriction is that if, at a later date, you wanted your thesis/dissertation to be published commercially, further permission would be required.

I wish you the best of luck with the completion of your thesis/dissertation.

Kind regards,  
Christina

### **Copyright & Permissions Team**

Gemma Alaway – Senior Rights & Permissions Adviser  
Christina Colwell - Rights & Permissions Assistant

#### Contact Details

E-mail: [permissions@iop.org](mailto:permissions@iop.org)

For further information about copyright and how to request permission: <http://iopscience.iop.org/page/copyright>

Please see our Author Rights Policy <http://iopublishing.org/author-rights/>

**Please note:** We do not provide signed permission forms as a separate attachment. Please print this email and provide it to your publisher as proof of permission.

**Please note:** Any statements made by IOP Publishing to the effect that authors do not need to get permission to use any content where IOP Publishing is not the publisher is not intended to constitute any sort of legal advice. Authors must make their own decisions as to the suitability of the content they are using and whether they require permission for it to be published within their article.

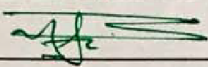


To whom it may concern

Subject: Permission to reuse/reprint a published/accepted/in-press manuscript in PhD dissertation

I am a co-author on the paper titled "Classification of Metastatic Tumor Cells using Computational Dynamic Morphology Analysis" that is in review for publication at Computer Methods and Programs in Biomedicine.

I grant permission to Mr. Mohammad Hasan to reuse/reprint this article in his PhD dissertation.

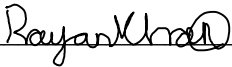
Name : Naeemul Hassan  
Signature :   
Email : nhasan@olemiss.edu  
Date : Oct - 30, 2017

To whom it may concern

Subject: Permission to reuse/reprint a published/accepted/in-press manuscript in PhD dissertation

I am a co-author on the paper titled “Classification of Metastatic Tumor Cells using Computational Dynamic Morphology Analysis” that is in review for publication at Computer Methods and Programs in Biomedicine.

I grant permission to Mr. Mohammad Hasan to reuse/reprint this article in his PhD dissertation.

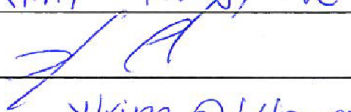
Name : Rayan khan  
Signature :   
Email : rayan.khan@mavs.uta.edu  
Date : 10/31/2017

To whom it may concern

Subject: Permission to reuse/reprint a published/accepted/in-press manuscript in PhD dissertation

I am a co-author on the paper titled "Classification of Metastatic Tumor Cells using Computational Dynamic Morphology Analysis" that is in review for publication at Computer Methods and Programs in Biomedicine.

I grant permission to Mr. Mohammad Hasan to reuse/reprint this article in his PhD dissertation.


Name : Kim, Youngtae  
Signature :   
Email : ykim@uta.edu  
Date : 10/31/2017

To whom it may concern

Subject: Permission to reuse/reprint a published/accepted/in-press manuscript in PhD dissertation

I am a co-author on the paper titled "Classification of Metastatic Tumor Cells using Computational Dynamic Morphology Analysis" that is in review for publication at Computer Methods and Programs in Biomedicine.

I grant permission to Mr. Mohammad Hasan to reuse/reprint this article in his PhD dissertation.

Name : Samir M. Iqbal  
Signature :   
Email : sm.iqbal@utrgv.edu  
Date : 10/30/2017

To whom it may concern

Subject: Permission to reuse/reprint a published/accepted/in-press manuscript in PhD dissertation

I am a co-author on the paper titled “Molecular Dynamics Study of Protein Deformation through Solid-State Nanopore” that is in review for publication at Functional Nanostructures.

I grant permission to Mr. Mohammad Hasan to reuse/reprint this article in his PhD dissertation.

Name : Mohammed Arif Iftakher Mahmood

Signature : 

Email : arif.iftakher@gmail.com


Date : 31/10/2017

To whom it may concern

Subject: Permission to reuse/reprint a published/accepted/in-press manuscript in PhD dissertation

I am a co-author on the paper titled "Molecular Dynamics Study of Protein Deformation through Solid-State Nanopore" that is in review for publication at Functional Nanostructures.

I grant permission to Mr. Mohammad Hasan to reuse/reprint this article in his PhD dissertation.

Name : NUZHAT MANSUR  
Signature :   
Email : nuzhat.mansur@mavs.uta.edu  
Date : 11/02/2017

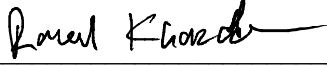
To whom it may concern

Subject: Permission to reuse/reprint a published/accepted/in-press manuscript in PhD dissertation

I am a co-author on the paper titled “Molecular Dynamics Study of Protein Deformation through Solid-State Nanopore” that is in review for publication at Functional Nanostructures.

I grant permission to Mr. Mohammad Hasan to reuse/reprint this article in his PhD dissertation.

Name : Raja Raheel Khanzada

Signature : 

Email : Raja Raheel . Khanzada @ MUVS. Uta. edu

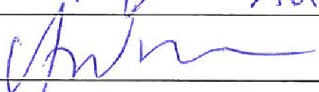
Date : Oct 30, 2017

To whom it may concern

Subject: Permission to reuse/reprint a published/accepted/in-press manuscript in PhD dissertation

I am a co-author on the paper titled "Molecular Dynamics Study of Protein Deformation through Solid-State Nanopore" that is in review for publication at Functional Nanostructures.

I grant permission to Mr. Mohammad Hasan to reuse/reprint this article in his PhD dissertation.

Name : Ashfaq Adnan  
Signature :   
Email : aadnan@uta.edu  
Date : 10-31-2017

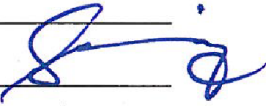


To whom it may concern

Subject: Permission to reuse/reprint a published/accepted/in-press manuscript in PhD dissertation

I am a co-author on the paper titled "Molecular Dynamics Study of Protein Deformation through Solid-State Nanopore" that is in review for publication at Functional Nanostructures.

I grant permission to Mr. Mohammad Hasan to reuse/reprint this article in his PhD dissertation.

Name : Samir M. Iqbal  
Signature :   
Email : sm.iqbal@utrgv.edu  
Date : 10/30/2017